# Towards an efficient computational strategy for electro-activation in cardiac mechanics

Emilio Garcia-Blanco[a], Rogelio Ortigosa[b,1], Antonio J. Gil[a,2], Javier Bonet[c]

[a] *Zienkiewicz Centre for Computational Engineering, College of Engineering Swansea University, Bay Campus, SA1 8EN, United Kingdom*

[b] *Computational Mechanics & Scientific Computing Group Technical University of Cartagena, Campus Muralla del Mar, 30202 Cartagena (Murcia), Spain*

[c] *University of Greenwich, London, SE10 9LS, United Kingdom*

**Abstract**

The computational modelling of the heart motion within a cardiac cycle is an extremely challenging problem due to (a) the complex multi-scale interaction that takes place between the electrophysiology and electrochemistry at cellular level and the macro-scale response of the heart muscle, and (b) the large deformations and the strongly anisotropic and quasi-incompressible behaviour of the myocardium. These pose an extreme challenge to the scalability of electromechanical solvers due to the size and conditioning of the system of equations required to obtain accurate solutions, both in terms of wall deformation and transmembrane potential propagation. In the search towards an efficient modelling of electro-activation, this paper presents a coupled electromechanical computational framework whereby, first, we explore the use of an efficient stabilised low order tetrahedral Finite Element methodology and compare it against a very accurate super enhanced mixed formulation previously introduced by the authors in [1] and, second, we exploit the use of tailor-made staggered and staggered linearised solvers in order to assess their feasibility against a fully monolithic approach. Through a comprehensive set of examples, culminating in a realistic ventricular geometry, we aim to put forward some suggestions regarding the level of discretisation and coupling required to ensure sufficiently reliable results yet with an affordable computational time.

*Keywords:* Cardiac electromechanics, Mixed Formulations, Polyconvexity, Finite Elements

## 1. Introduction

Cardiovascular diseases (CVD) are considered one of the main causes of death, especially in the developed world. With a constantly increasing ageing population, the burden that CVD patients put on the healthcare system (both in terms of infrastructure and staff time) has been recognised as an urgent matter in need of immediate attention, before it becomes unsustainable [2–4]. The support that computational mechanics can provide through the design of in-silico diagnostic tools is nowadays well-acknowledged by experts in the field, especially in challenging cardiopathies such as heart infarction or dysrhythmia. Over the last decade, great effort has been devoted to attempting the computational modelling of heart-related CVD with two objectives in mind: first, to help clinicians by equipping them with novel diagnostic tools and, second, to better understand the very complex electro-chemo-bio-mechanical phenomena underpinning the behaviour of the heart.

[1] Corresponding author: rogelio.ortigosa@upct.es

[2] Corresponding author: a.j.gil@swansea.ac.uk

In a nutshell, the cardiac wall is comprised of layers of collagen and bands of muscle fibres (cardiomyoytes) which contract with the propagation of the cardiac action potential. This depolarisation generates a set of ion interchanges which trigger the cross-bridge cycle [5] and, eventually, restore the initial cell membrane potential (repolarisation) [6]. This rapid multi-scale process initiates at cell level and culminates with the macro-contraction of the heart muscle (constantly repeating with every heartbeat). The modelling of this highly complex space-time coupled phenomenon requires the careful interaction of electrophysiology [7], electrochemistry [8] and nonlinear continuum mechanics [9–12], in conjunction with in-vivo material characterisation [13, 14], accurate medical imaging and state-of-the art numerical algorithms for new computer architectures [15, 16].

Electrophysiology is devoted to describe the time evolution of the cardiac action potential, classically simulated through a set of diffusion-reaction equations activated via a sophisticated source term encapsulating the chemical activity. A variety of numerical models have been proposed over the years [7, 17], referred to as either bidomain [18–20] or monodomain [7, 21–24] models, the latter being preferred due to their relative ease of implementation. Regarding electrochemistry, since the pioneering work of Hodgkin and Huxley [8] in ionic modelling, available numerical models have improved in accuracy due to the increased availability of experimental data [13, 25–33]. Unfortunately, this led to prohibitively expensive numerical models, until the work of Bueno-Orovio *et al.* [34] put an end to this trend by proposing an extremely efficient alternative. As for material characterisation, since the original work of Demiray [35], numerous constitutive models have been introduced, capable of accounting for the anisotropy, transmural gradient fibre orientation and viscoelasticity of the myocardium [11, 36–39]. Nowadays, the strain energy law proposed by Holzapfel and Ogden [10] stands as the norm in the field. The electro-mechanical activation is incorporated via the so-called active stress [37] or active strain [40] approaches. A challenging aspect of this model is the strong anisotropy induced by the fibre component of the model as well as the quasi-incompressibility constraint of the matrix, which hinder the use of standard computational solvers, due to the stiff conditioning of the resulting system of equations.

Several research groups have pursued the complete coupled electromechanical simulation of the heart, starting with the work of Nash and Panfilov [41] on a simplified two-dimensional domain. The work of Watanabe *et al.* [15] adds the surrounding fluid interaction as part of a three-dimensional idealised ventricle. Vigmond *et al.* introduce a new approach by using cable methods and highlight the greater computational cost associated with the fluid sub-problem compared to the chemo-electrical one [42]. Göktepe and Kühl [43–45] developed a fully implicit electro-mechanical model where the electromechanical feedback was implemented via a monolithic scheme. Quarteroni, Rossi *et al.* [16, 23, 46, 47] have extensively worked on the development of an active strain coupled electromechanical solver. In addition, Baillargeon *et al.* [24] presented an entire heart simulation including a lumped model of the surrounding cardiovascular system mimicking the blood dynamics. Finally, some recent efforts have been devoted to the problem optimisation [48, 49] in this context.

Surprisingly, from the computational standpoint, most of the coupled cardiac models listed above assume quasi-incompressibility modelled via the penalty method and use displacement-potential based ($\boldsymbol{x}$-$\phi$) Finite Element formulations with linear tetrahedral technology[3] [23, 24, 45, 47]. Unfortunately, it is well-known that this Finite Element approach can be susceptible of experiencing bending and volumetric locking as well as spurious pressure oscillations [50, 51]. To prevent this, the mixed formulation proposed by some of the authors in [50, 52–55] was adapted to cardiac electromechanics in our previous work [1], with the ultimate goal of overcoming the aforementioned numerical difficulties [50, 55–59]. Specifically, in Reference [1], a monolithic fully

[3]Complex geometries, generated from medical imaging and segmentation reconstruction, currently advocate for the use of tetrahedral technology due to the relative ease to generate suitable three-dimensional meshes.

implicit scheme was introduced leading to a highly accurate method capable of reproducing the two-way electromechanical feedback. The work also studied the loss of ellipticity and polyconvexity of the Holzapfel and Ogden model [60–62] and presented a new super enhanced mixed Finite Element formulation, short-named as **MFA**. In this **MFA** formulation, elemental strain and transmembrane potential gradient fields are incorporated in the methodology and resolved locally through a static condensation procedure. In addition, a comprehensive study was carried out where both active strain (**MFA**-$\gamma$) and active stress (**MFA**-$T_a$) approaches were compared in combination with two widely-used ionic models for a series of simplified three-dimensional examples.

Unfortunately, the high computational cost associated with the (large scale) modelling of the electro-mechanical coupling in a truly realistic ventricular geometry, still represents a bottleneck to the scalability of these algorithms (e.g. in terms of assembly, static condensation and system solution). Crucially, our previous work [1] constitutes an ideal benchmark and the perfect platform in order to assess the performance, reliability and limitations of less demanding coupling schemes and more affordable Finite Element formulations, as well as providing a quantitative evaluation of the importance of the electromechanical feedback in a complete cardiac simulation. As a result, our efforts in this paper will be devoted to (a) assess the suitability of an alternative stabilised linear finite element formulation for displacement, pressure and intermembrane potential ($\boldsymbol{x}$-$\phi$-$p$ formulation) [50, 51], comparing it against the super enhanced **MFA** formulation proposed in [1] and (b) alleviate the computational cost associated with the solution of the resulting stiff system of equations, through the implementation of alternative staggered and staggered linearised solvers [63–65], without compromising the overall accuracy of the scheme.

The paper is organised as follows. Section 2 introduces the fundamentals of the kinematics in nonlinear continuum mechanics and the governing equations used to describe the behaviour of the heart during the cardiac cycle. In Section 3, relevant aspects concerning the passive response of the myocardium, its electrophysiology and the coupling between the mechanics and the electric physics are briefly recalled. Section 4 presents the three alternative formulations which will be investigated in this paper, namely, the widely used $\boldsymbol{x}$-$\phi$ formulation, the sophisticated **MFA** formulation in [1] and a proposed stabilised $\boldsymbol{x}$-$\phi$-$p$ formulation. Section 5 details the specific (low order) Finite Element discretisation technologies employed as well as three alternative coupling algorithms, namely, monolithic, staggered and staggered linearised. An ample spectrum of numerical examples is included in Section 6 in order to test the suitability of the various discretisations and implementations, with the objective to put forward some suggestions regarding the level of discretisation and coupling required in the search for an approach which is sufficiently accurate yet with an affordable computational time. Finally, Section 7 provides some concluding remarks and a summary of the key contributions of this paper.

## 2. Kinematics and governing equations

Let us consider the motion of a continuum (representing in this case the human myocardium) defined by an initial configuration of domain $\Omega_0$ with boundary $\partial\Omega_0$ and outward normal $\boldsymbol{N}$. After the motion, the continuum occupies a final configuration defined by a domain $\Omega$ with boundary $\partial\Omega$ and outward normal $\boldsymbol{n}$. The pseudo-time ($t$) dependent mapping field $\boldsymbol{\phi}$ links a material particle from initial configuration $\boldsymbol{X} \in \Omega_0$ to final configuration $\boldsymbol{x} \in \Omega$ according to $\boldsymbol{x} = \boldsymbol{\phi}(\boldsymbol{X}, t)$ (refer to Figure 1). Three kinematic measures are typically introduced, namely, the deformation gradient tensor $\boldsymbol{F}_{\boldsymbol{x}}$, its cofactor $\boldsymbol{H}_{\boldsymbol{x}}$ and its determinant $J_{\boldsymbol{x}}$, defined as

$$\boldsymbol{F}_{\boldsymbol{x}} = \boldsymbol{\nabla}_0 \boldsymbol{x}; \qquad \boldsymbol{H}_{\boldsymbol{x}} = \frac{1}{2}\boldsymbol{F}_{\boldsymbol{x}} \times \boldsymbol{F}_{\boldsymbol{x}}; \qquad J_{\boldsymbol{x}} = \frac{1}{3}\boldsymbol{H}_{\boldsymbol{x}} : \boldsymbol{F}_{\boldsymbol{x}}, \tag{1}$$

where $\boldsymbol{\nabla}_0(\bullet)$ denotes the Lagrangian (initial configuration) gradient operator, and for any two second order tensors $\boldsymbol{A}$ and $\boldsymbol{B}$, $\times$ in $(1)_b$ denotes the tensor cross product operation defined as

$(\boldsymbol{A}\times\boldsymbol{B})_{iI} = \mathcal{E}_{ijk}\mathcal{E}_{IJK}A_{jJ}B_{kK}$ [50, 59, 66]. The coupled system of partial differential equations governing the motion $\boldsymbol{x}$ and the evolution of transmembrane potential $\phi$ are now introduced. The conservation of linear momentum[4] can be expressed in a Lagrangian setting as

$$\left.\begin{aligned} \mathrm{DIV}\boldsymbol{P} + \boldsymbol{b}_0 &= \boldsymbol{0} && \text{in } \Omega_0 \times [\,0\,,\,T\,] \\ \boldsymbol{P}\boldsymbol{N} &= \boldsymbol{t}_0 && \text{on } \partial_t\Omega_0 \times [\,0\,,\,T\,] \\ \boldsymbol{x} &= \boldsymbol{\phi}_{\boldsymbol{x}} && \text{on } \partial_{\boldsymbol{x}}\Omega_0 \times [\,0\,,\,T\,] \end{aligned}\right\} \tag{2}$$

where $\partial\Omega_0 = \partial_{\boldsymbol{x}}\Omega_0 \cup \partial_t\Omega_0$ and $\partial_{\boldsymbol{x}}\Omega_0 \cap \partial_t\Omega_0 = \emptyset$, $\boldsymbol{P}$ represents the first Piola-Kirchhoff stress tensor, $\boldsymbol{b}_0$ a force per unit undeformed volume and $\boldsymbol{t}_0$ a force per unit of undeformed area. Satisfaction of rotational equilibrium requires $\boldsymbol{P}\boldsymbol{F}_{\boldsymbol{x}}^T = \boldsymbol{F}_{\boldsymbol{x}}\boldsymbol{P}^T$. The time-dependent evolution of the transmembrane potential $\phi$, considering a monodomain approach [21, 22], can be expressed in a Lagrangian setting as

$$\left.\begin{aligned} \mathrm{DIV}\boldsymbol{Q} + f_\phi &= \dot{\phi} && \text{in } \Omega_0 \times [\,0\,,\,T\,] \\ \boldsymbol{Q}\cdot\boldsymbol{N} &= 0 && \text{on } \partial\Omega_0 \times [\,0\,,\,T\,] \\ \phi &= \phi_0 && \text{in } \Omega_0 \times 0 \end{aligned}\right\} \tag{3}$$

where $\dot{(\bullet)}$ represents the time derivative, $\phi_0$ denotes the resting potential, $\boldsymbol{Q}$ represents the electric flux vector across the cell membrane [44] and $f_\phi$ the electrical source term.

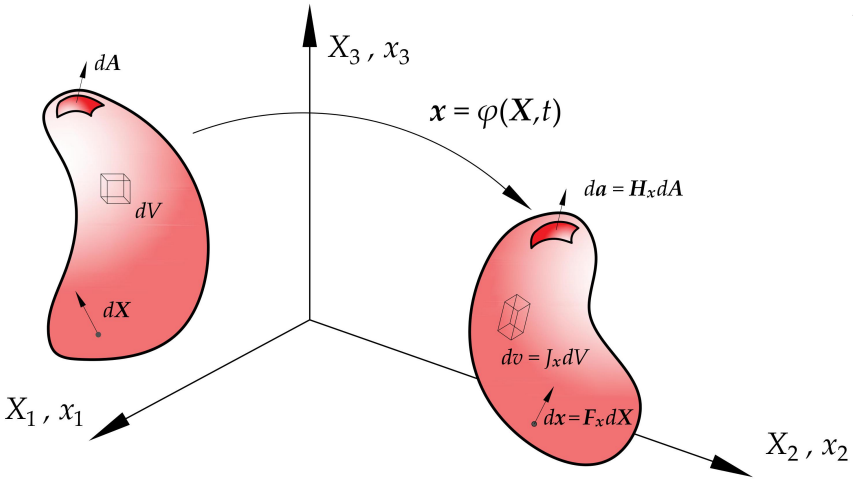


Figure 1: Motion map of the continuum $\Omega_0$ and the kinematic measures $\{\boldsymbol{F}_{\boldsymbol{x}}, \boldsymbol{H}_{\boldsymbol{x}}, J_{\boldsymbol{x}}\}$.

## 3. Constitutive equations

For the closure of the governing equations (2)-(3), constitutive laws are needed for the evaluation of $\boldsymbol{P}$, $\boldsymbol{Q}$ and $f_\phi$.

### *3.1. Passive response of the heart*

The passive response of the heart is usually described with an invariant representation of a strain energy functional $\Psi(\boldsymbol{\nabla}_0\boldsymbol{x})$ in terms of the kinematic measures $\{\boldsymbol{F}_{\boldsymbol{x}}, \boldsymbol{H}_{\boldsymbol{x}}, J_{\boldsymbol{x}}\}$. In addition, the strain energy must describe the underlying anisotropic structure of the cardiac tissue, characterised by a transmural spatially varying set of muscle fibres, represented by the triad $\{\boldsymbol{f}_0, \boldsymbol{s}_0, \boldsymbol{n}_0\}$ at each Lagrangian particle $\boldsymbol{X} \in \Omega_0$ (refer to Figure 2) [9, 46, 67]. As such, the strain energy

[4] It is customary to neglect inertial effects in equation (2) (*quasi-statics*).

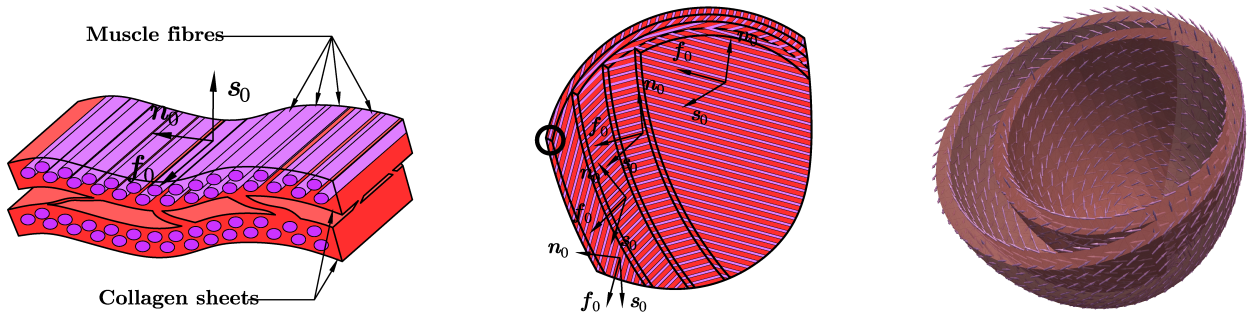


Figure 2: Anisotropic structure of the cardiac tissue. Representation of the triad $\{\boldsymbol{f}_0, \boldsymbol{s}_0, \boldsymbol{n}_0\}$ in the Lagrangian setting (left), accounting for their spatial variability (centre). Idealised set of ventricles (right).

is additively decomposed into its isotropic-deviatoric, volumetric and anisotropic contributions, denoted as $\hat{W}$, $U$ and $W^{\text{ani}}$, respectively, as

$$\Psi\left(\boldsymbol{\nabla}_0 \boldsymbol{x}\right) = W\left(\boldsymbol{F}_{\boldsymbol{x}}, \boldsymbol{H}_{\boldsymbol{x}}, J_{\boldsymbol{x}}, \boldsymbol{f}_0, \boldsymbol{s}_0\right) = \hat{W}\left(\boldsymbol{F}_{\boldsymbol{x}}, \boldsymbol{H}_{\boldsymbol{x}}, J_{\boldsymbol{x}}\right) + U\left(J_{\boldsymbol{x}}\right) + W^{\text{ani}}\left(\boldsymbol{F}_{\boldsymbol{x}}, \boldsymbol{H}_{\boldsymbol{x}}, J_{\boldsymbol{x}}, \boldsymbol{f}_0, \boldsymbol{s}_0\right). \quad (4)$$

For instance, Holzapfel and Ogden [10] proposed the following strain energy functional for the characterisation of the myocardium

$$\begin{aligned} \hat{W}(\boldsymbol{F}_{\boldsymbol{x}}, J_{\boldsymbol{x}}) &= \frac{a}{2b} e^{b\left(II_{\hat{\boldsymbol{F}}_{\boldsymbol{x}}} - 3\right)}; \qquad & U\left(J_{\boldsymbol{x}}\right) &= \frac{\kappa}{2}\left(J_{\boldsymbol{x}} - 1\right)^2; \\ W^{\text{ani}}\left(\boldsymbol{F}_{\boldsymbol{x}}, \boldsymbol{f}_0, \boldsymbol{s}_0\right) &= \frac{a_f}{2b_f}\left(e^{b_f\langle I_{4,\boldsymbol{f}_0} - 1\rangle^2} - 1\right) + \frac{a_s}{2b_s}\left(e^{b_s\langle I_{4,\boldsymbol{s}_0} - 1\rangle^2} - 1\right) + \frac{a_{fs}}{2b_{fs}}\left(e^{b_{fs} I_{8,\boldsymbol{f}_0\boldsymbol{s}_0}^2} - 1\right), \end{aligned} \quad (5)$$

with $\{a, \kappa, a_f, b_f, a_s, b_s, a_{fs}, b_{fs}\}$ positive material constants and where $\langle\bullet\rangle$ represents the Macaulay brackets $\langle\bullet\rangle = (\bullet + |\bullet|)/2$, $II_{(\bullet)}$ denotes the second invariant of $(\bullet)$ and with the anisotropic invariants $I_{4,\boldsymbol{f}_0}$, $I_{4,\boldsymbol{s}_0}$, $I_{8,\boldsymbol{f}_0\boldsymbol{s}_0}$ defined as

$$\begin{aligned} II_{\hat{\boldsymbol{F}}_{\boldsymbol{x}}} &= J_{\boldsymbol{x}}^{-2/3}\boldsymbol{F}_{\boldsymbol{x}} : \boldsymbol{F}_{\boldsymbol{x}}; \qquad & I_{4,\boldsymbol{f}_0} &= \boldsymbol{F}_{\boldsymbol{x}}\boldsymbol{f}_0 \cdot \boldsymbol{F}_{\boldsymbol{x}}\boldsymbol{f}_0; \\ I_{4,\boldsymbol{s}_0} &= \boldsymbol{F}_{\boldsymbol{x}}\boldsymbol{s}_0 \cdot \boldsymbol{F}_{\boldsymbol{x}}\boldsymbol{s}_0; \qquad & I_{8,\boldsymbol{f}_0\boldsymbol{s}_0} &= \boldsymbol{F}_{\boldsymbol{x}}\boldsymbol{f}_0 \cdot \boldsymbol{F}_{\boldsymbol{x}}\boldsymbol{s}_0. \end{aligned} \quad (6)$$

The loss or ellipticity and polyconvexity [60, 62, 68] of the above model was analysed in our previous publication [1], where a possible regularisation approach was also put forward. The first Piola-Kirchhoff stress tensor $\boldsymbol{P}$ and the fourth order elasticity tensor $\boldsymbol{\mathcal{C}}$ can be easily obtained as

$$\boldsymbol{P} = \partial_{\boldsymbol{\nabla}_0\boldsymbol{x}}\Psi\left(\boldsymbol{\nabla}_0\boldsymbol{x}\right); \qquad \boldsymbol{\mathcal{C}} = \partial^2_{\boldsymbol{\nabla}_0\boldsymbol{x}\boldsymbol{\nabla}_0\boldsymbol{x}}\Psi. \quad (7)$$

or, alternatively, in terms of the kinematic measures $\{\boldsymbol{F}_{\boldsymbol{x}}, \boldsymbol{H}_{\boldsymbol{x}}, J_{\boldsymbol{x}}\}$ as [52–54]

$$\boldsymbol{P} = \partial_{\boldsymbol{F}_{\boldsymbol{x}}} W + \partial_{\boldsymbol{H}_{\boldsymbol{x}}} W \boldsymbol{\times} \boldsymbol{F}_{\boldsymbol{x}} + \partial_{J_{\boldsymbol{x}}} W \boldsymbol{H}_{\boldsymbol{x}}, \quad (8)$$

and

$$\begin{aligned} \boldsymbol{\mathcal{C}} = {} & \partial^2_{\boldsymbol{F}_{\boldsymbol{x}}\boldsymbol{F}_{\boldsymbol{x}}} W + \boldsymbol{F}_{\boldsymbol{x}} \boldsymbol{\times} \partial^2_{\boldsymbol{H}_{\boldsymbol{x}}\boldsymbol{H}_{\boldsymbol{x}}} W \boldsymbol{\times} \boldsymbol{F}_{\boldsymbol{x}} + \partial^2_{J_{\boldsymbol{x}}J_{\boldsymbol{x}}} W \boldsymbol{H}_{\boldsymbol{x}} \otimes \boldsymbol{H}_{\boldsymbol{x}} \\ & + \partial^2_{\boldsymbol{F}_{\boldsymbol{x}}\boldsymbol{H}_{\boldsymbol{x}}} W \boldsymbol{\times} \boldsymbol{F}_{\boldsymbol{x}} + \boldsymbol{F}_{\boldsymbol{x}} \boldsymbol{\times} \partial^2_{\boldsymbol{H}_{\boldsymbol{x}}\boldsymbol{F}_{\boldsymbol{x}}} W + \partial^2_{\boldsymbol{F}_{\boldsymbol{x}}J_{\boldsymbol{x}}} W \otimes \boldsymbol{H}_{\boldsymbol{x}} + \boldsymbol{H}_{\boldsymbol{x}} \otimes \partial^2_{J_{\boldsymbol{x}}\boldsymbol{F}_{\boldsymbol{x}}} W \\ & + \boldsymbol{F}_{\boldsymbol{x}} \boldsymbol{\times} \partial^2_{\boldsymbol{H}_{\boldsymbol{x}}J_{\boldsymbol{x}}} W \otimes \boldsymbol{H}_{\boldsymbol{x}} + \boldsymbol{H}_{\boldsymbol{x}} \otimes \partial^2_{J_{\boldsymbol{x}}\boldsymbol{H}_{\boldsymbol{x}}} W \boldsymbol{\times} \boldsymbol{F}_{\boldsymbol{x}} + \boldsymbol{\mathcal{I}} \boldsymbol{\times} \left(\partial_{\boldsymbol{H}_{\boldsymbol{x}}} W + \partial_{J_{\boldsymbol{x}}} W \boldsymbol{F}_{\boldsymbol{x}}\right), \end{aligned} \quad (9)$$

with $\mathcal{I}_{iIjJ} = \delta_{ij}\delta_{IJ}$ and with $\left(\boldsymbol{\mathcal{A}} \boldsymbol{\times} \boldsymbol{A}\right)_{iIjJ} = \mathcal{A}_{iIpP}A_{qQ}\mathcal{E}_{jpq}\mathcal{E}_{JPQ}$ and $\left(\boldsymbol{A} \boldsymbol{\times} \boldsymbol{\mathcal{A}}\right)_{iIjJ} = \mathcal{A}_{qQjJ}A_{pP}\mathcal{E}_{ipq}\mathcal{E}_{IPQ}$ for any fourth and second order tensors $\boldsymbol{\mathcal{A}}$ and $\boldsymbol{A}$, respectively.

### 3.2. Active response of the heart

The (active) coupling of the stress tensor with the transmembrane potential $\phi$ is typically accounted for following either an active stress or an active strain approach. In the *active stress* approach [37, 41, 45], an additive decomposition of $\boldsymbol{P}$ is defined with a coupled (active) $\boldsymbol{P}_{\text{Active}}$ contribution and a purely mechanical (passive) $\boldsymbol{P}_{\text{Passive}}$ contribution as

$$\boldsymbol{P} = \boldsymbol{P}_{\text{Active}} + \boldsymbol{P}_{\text{Passive}}; \quad \boldsymbol{P}_{\text{Active}} = T_a \boldsymbol{F}_{\boldsymbol{x}} \boldsymbol{f}_0 \otimes \boldsymbol{f}_0; \quad \boldsymbol{P}_{\text{Passive}} = \partial_{\boldsymbol{F}_{\boldsymbol{x}}} W + \partial_{\boldsymbol{H}_{\boldsymbol{x}}} W \boldsymbol{\times} \boldsymbol{F}_{\boldsymbol{x}} + \partial_{J_{\boldsymbol{x}}} W \boldsymbol{H}_{\boldsymbol{x}}, \tag{10}$$

where $T_a$ represents the active cardiomyocite contraction stress and the passive term $\boldsymbol{P}_{\text{Passive}}$ adopts an identical representation to that in (8). On the other hand, the *active strain* approach [23, 40, 46] is based on a multiplicative decomposition of $\boldsymbol{F}_{\boldsymbol{x}} = \boldsymbol{F}_{\boldsymbol{x}}^E \boldsymbol{F}^A$ into its elastic (passive) $\boldsymbol{F}_{\boldsymbol{x}}^E$ and coupled (active) $\boldsymbol{F}^A$ contributions, where $\boldsymbol{F}^A$ is formulated in terms of the electrically activated stretches $\left\{\gamma_{\boldsymbol{f}_0}, \gamma_{\boldsymbol{s}_0}, \gamma_{\boldsymbol{n}_0}\right\}$ as

$$\boldsymbol{F}^A = \boldsymbol{I} + \gamma_{\boldsymbol{f}_0} \boldsymbol{f}_0 \otimes \boldsymbol{f}_0 + \gamma_{\boldsymbol{s}_0} \boldsymbol{s}_0 \otimes \boldsymbol{s}_0 + \gamma_{\boldsymbol{n}_0} \boldsymbol{n}_0 \otimes \boldsymbol{n}_0. \tag{11}$$

In this approach, the strain energy $\Psi$ depends on the elastic component $\boldsymbol{F}_{\boldsymbol{x}}^E$ as

$$\Psi\left(\boldsymbol{\nabla}_0 \boldsymbol{x}, \boldsymbol{F}^A\right) = W\left(\boldsymbol{F}_{\boldsymbol{x}}^E, \boldsymbol{H}_{\boldsymbol{x}}^E, J_{\boldsymbol{x}}^E\right) = W^E\left(\boldsymbol{F}_{\boldsymbol{x}}, \boldsymbol{H}_{\boldsymbol{x}}, J_{\boldsymbol{x}}, \boldsymbol{F}^A, \boldsymbol{H}^A, J^A\right). \tag{12}$$

with $\boldsymbol{H}^A$ and $J^A$ the cofactor and Jacobian of $\boldsymbol{F}^A$, respectively, defined accordingly as in $(1)_b$ and $(1)_c$. Consideration of $W^E$ in (12) leads to an expression for $\boldsymbol{P}$ similar to that in (8) as

$$\boldsymbol{P} = \partial_{\boldsymbol{F}_{\boldsymbol{x}}} W^E + \partial_{\boldsymbol{H}_{\boldsymbol{x}}} W^E \boldsymbol{\times} \boldsymbol{F}_{\boldsymbol{x}} + \partial_{J_{\boldsymbol{x}}} W^E \boldsymbol{H}_{\boldsymbol{x}}. \tag{13}$$

### 3.3. Electrophysiology of the heart

In analogy with Fick's Law, it is customary [30, 34] to define $\boldsymbol{Q}$ in (3) as

$$\boldsymbol{Q} = \boldsymbol{D} \boldsymbol{\nabla}_0 \phi, \tag{14}$$

where $\boldsymbol{D}$ represents the second order conductivity tensor [44], expressed in terms of the electrical conductivities $d_{\text{iso}}$ and $d_{\text{ani}}$ [23, 44, 46] as

$$\boldsymbol{D} = d_{\text{iso}} J_{\boldsymbol{x}}^{-2} \boldsymbol{H}_{\boldsymbol{x}}^T \boldsymbol{H}_{\boldsymbol{x}} + d_{\text{ani}} \boldsymbol{f}_0 \otimes \boldsymbol{f}_0. \tag{15}$$

The source term $f_\phi$ in (3) depends on $\phi$ and on $\boldsymbol{q} \in \mathbb{R}^{n_{\boldsymbol{q}}}$, the latter representing the set of internal variables [8, 13, 25, 28], with $n_{\boldsymbol{q}}$ the total number of internal variables. A set of first order differential equations [8, 30, 32–34] describe the evolution of $\boldsymbol{q}$ as

$$\dot{\boldsymbol{q}}(\phi) = \boldsymbol{g}(\phi, \boldsymbol{q}(\phi)), \tag{16}$$

with $\boldsymbol{g} : \mathbb{R}^{n_{\boldsymbol{q}}+1} \to \mathbb{R}^{n_{\boldsymbol{q}}}$. It is customary to assume an additive decomposition of $f_\phi$ as

$$f_\phi(\phi, \boldsymbol{q}(\phi)) = I_{\text{stim}} + I_{\text{sum}}(\phi, \boldsymbol{q}(\phi)), \tag{17}$$

with $I_{\text{sum}} : \mathbb{R}^{n_{\boldsymbol{q}}+1} \to \mathbb{R}$ and where the first term $I_{\text{stim}}$ in $(17)_b$ enables the initial propagation of the electrical wave (3). The expressions for $I_{\text{sum}}$ is dictated by the choice of the ionic model. In this paper we consider the model proposed by Bueno-Orovio [34]. The reader is referred to [34] for the expressions of $I_{\text{sum}}$ for this specific model $\boldsymbol{g}(\phi, \boldsymbol{q}(\phi))$ (16).

### 3.4. Electro-Mechanical activation of the heart

As described in Section 3.2, two coupling approaches, denoted as active stress and active strain can be used for the cardiac electro-mechanical activation. In the *active stress* approach, an ordinary differential equation is defined for the evolution of the active cardiomyocite contraction stress $T_a$ as

$$\dot{T}_a = h_{T_a}\left(T_a, \phi\right), \tag{18}$$

with $h_{T_a} : \mathbb{R}^2 \to \mathbb{R}$. The model proposed by Nash and Panfilov [41] considers the following expression for $h_{T_a}$ (18)

$$h_{T_a} = \varepsilon\left(u\right)\left(k_{T_a} u - T_a\right); \qquad \varepsilon\left(u\right) = \begin{cases} 1 & \text{if } u > 0 \\ 10 & \text{if } u < 0 \end{cases}; \qquad u = \frac{\left(\phi + 84\right)}{85.7}, \tag{19}$$

where $k_{T_a}$ is a constant with dimensions of stress [41]. On the other hand, in the *active strain* approach, the evolution equation for the electrical stretch $\gamma_{\boldsymbol{f}_0}$ (11) can be expressed as

$$\dot{\gamma}_{\boldsymbol{f}_0} = h_{\gamma_{\boldsymbol{f}_0}}\left(\gamma_{\boldsymbol{f}_0}, \phi, \boldsymbol{q}\left(\phi\right)\right), \tag{20}$$

with $= h_{\gamma_{\boldsymbol{f}_0}} : \mathbb{R}^{n_{\boldsymbol{q}}+2} \to \mathbb{R}$. The remaining electric stretches $\{\gamma_{\boldsymbol{s}_0}, \gamma_{\boldsymbol{n}_0}\}$ in (11) are usually related to $\gamma_{\boldsymbol{f}_0}$ [1]. In Reference [23], Rossi *et al.* proposed the following thermodynamically consistent expression for the function $h_{\gamma_{\boldsymbol{f}_0}}$

$$h_{\gamma_{\boldsymbol{f}_0}} = \frac{1}{\hat{\mu}_A c_{\mathrm{Ca}}^2}\left(F_A + \frac{2I_{4,\boldsymbol{f}_0}}{\left(1+\gamma_{\boldsymbol{f}_0}\right)^3} - 2I_{4,\boldsymbol{f}_0}\right), \tag{21}$$

where $\hat{\mu}_A$ represents a viscous-type term, $c_{\mathrm{Ca}}$ denotes the calcium concentration and $F_A$ is the dimensionless active force along the fibre direction $\boldsymbol{f}_0$, defined as

$$F_A = \alpha\left(c_{\mathrm{Ca}} - c_{\mathrm{Ca},0}\right)^2 \chi_{[l_{\min}, l_{\max}]}\left(\mathcal{F}\left(l\right)\right); \qquad \chi_{[l_{\min}, l_{\max}]}\left(\mathcal{F}\left(l\right)\right) = \begin{cases} \mathcal{F}\left(l\right) & \text{if } l \in [l_{\min}, l_{\max}] \\ 0 & \text{if } l \notin [l_{\min}, l_{\max}] \end{cases};$$

$$l = I_{4,\boldsymbol{f}_0} l_0; \qquad \mathcal{F}\left(l\right) = \frac{d_0}{2} + \sum_{n=1}^{3} d_n \cos\left(nl\right) + e_n \sin\left(nl\right), \tag{22}$$

where $\alpha$ is the active force of a sarcomere, $c_{\mathrm{Ca},0}$, the resting calcium concentration, $\{l_{\min}, l_{\max}\}$, the minimum and maximum sarcomere lengths and $\{d_0, d_n, e_n\}$, constants reported in [69]. Finally, following [23], the electrical stretches $\{\gamma_{\boldsymbol{n}_0}, \gamma_{\boldsymbol{s}_0}\}$ are defined satisfying $\det \boldsymbol{F}^A = 1$ as

$$\gamma_{\boldsymbol{n}_0} = 4\gamma_{\boldsymbol{f}_0}; \qquad \gamma_{\boldsymbol{s}_0} = \left(1+\gamma_{\boldsymbol{f}_0}\right)^{-1}\left(1+4\gamma_{\boldsymbol{f}_0}\right)^{-1} - 1. \tag{23}$$

## 4. Variational formulation for cardiac electro-mechanics

In this Section, the weak forms associated with the governing and constitutive equations in Sections 2 and 3 are presented.

### 4.1. Standard two-field $\boldsymbol{x}$-$\phi$ formulation

In this formulation, the unknown fields and their virtual variations are $\boldsymbol{\mathcal{U}} = \{\boldsymbol{x}, \phi\} \in \mathbb{V}^{\boldsymbol{x}} \times \mathbb{V}^{\phi}$ and $\delta\boldsymbol{\mathcal{V}} = \{\delta\boldsymbol{x}, \delta\phi\} \in \mathbb{V}_0^{\boldsymbol{x}} \times \mathbb{V}^{\phi}$, respectively, with

$$\mathbb{V}^{\boldsymbol{x}} = \left\{\boldsymbol{x} : \Omega_0 \to \mathbb{R}^3; \quad (\boldsymbol{x})_i \in H^1\left(\Omega_0\right)\right\}; \quad \mathbb{V}^{\phi} = \left\{\phi : \Omega_0 \to \mathbb{R}; \quad \phi \in H^1\left(\Omega_0\right)\right\}, \tag{24}$$

and

$$\mathbb{V}_0^{\boldsymbol{x}} = \left\{\boldsymbol{x} \in \mathbb{V}^{\boldsymbol{x}}, \quad \boldsymbol{x} = \boldsymbol{0} \text{ on } \partial_{\boldsymbol{x}}\Omega_0\right\}, \tag{25}$$

which result in the following (two) weak forms for this formulation $\mathcal{W}_{\boldsymbol{\mathcal{U}}} = \{\mathcal{W}_{\boldsymbol{x}}, \mathcal{W}_{\phi}\}$

$$\begin{aligned}
\mathcal{W}_{\boldsymbol{x}} &= \int_{\Omega_0} \boldsymbol{P} : \boldsymbol{\nabla}_0 \delta\boldsymbol{x} \, d\Omega_0 - \int_{\Omega_0} \delta\boldsymbol{x} \cdot \boldsymbol{b}_0 \, d\Omega_0 - \int_{\partial_t\Omega_0} \delta\boldsymbol{x} \cdot \boldsymbol{t}_0 \, d\Gamma = 0; \\
\mathcal{W}_{\phi} &= \int_{\Omega_0} \delta\phi \, \dot{\phi} \, d\Omega_0 + \int_{\Omega_0} \boldsymbol{\nabla}_0 \delta\phi \cdot \boldsymbol{Q} \, d\Omega_0 - \int_{\Omega_0} \delta\phi f_{\phi} \, d\Omega_0 = 0,
\end{aligned} \tag{26}$$

where in order to capture the nearly/truly incompressible nature of the myocardium, a high value of $\kappa$ (featuring in the volumetric functional $U(J_{\boldsymbol{x}})$ in (5)) is typically adopted [44].

### *4.2. Stabilised three-field $\boldsymbol{x}$-$\phi$-$p$ formulation*

In this formulation, an additional Lagrange multiplier field (to weakly enforce the incompressibility condition) $p \in \mathbb{V}^p$ and its virtual variation $\delta p \in \mathbb{V}^p$ are added to the set of unknowns $\boldsymbol{\mathcal{U}} = \{\boldsymbol{x}, \phi, p\} \in \mathbb{V}^{\boldsymbol{x}} \times \mathbb{V}^{\phi} \times \mathbb{V}^p$ and virtual fields $\delta\boldsymbol{\mathcal{V}} = \{\delta\boldsymbol{x}, \delta\phi, \delta p\} \in \mathbb{V}_0^{\boldsymbol{x}} \times \mathbb{V}^{\phi} \times \mathbb{V}^p$ , respectively, with

$$\mathbb{V}^p = \{p : \Omega_0 \to \mathbb{R}; \qquad p \in \mathbb{L}_2(\Omega_0)\}, \tag{27}$$

resulting in (three) weak forms for this formulation $\mathcal{W}_{\boldsymbol{\mathcal{U}}} = \{\mathcal{W}_{\boldsymbol{x}}, \mathcal{W}_{\phi}, \mathcal{W}_p\}$

$$\begin{aligned}
\mathcal{W}_{\boldsymbol{x}} &= \int_{\Omega_0} (\boldsymbol{P} + p\boldsymbol{H}_{\boldsymbol{x}}) : \boldsymbol{\nabla}_0 \delta\boldsymbol{x} \, d\Omega_0 - \int_{\Omega_0} \delta\boldsymbol{x} \cdot \boldsymbol{b}_0 \, d\Omega_0 - \int_{\partial_t\Omega_0} \delta\boldsymbol{x} \cdot \boldsymbol{t}_0 \, d\Gamma = 0; \\
\mathcal{W}_{\phi} &= \int_{\Omega_0} \delta\phi \, \dot{\phi} \, d\Omega_0 + \int_{\Omega_0} \boldsymbol{\nabla}_0 \delta\phi \cdot \boldsymbol{Q} \, d\Omega_0 - \int_{\Omega_0} \delta\phi f_{\phi} \, d\Omega_0 = 0; \\
\mathcal{W}_p &= \int_{\Omega_0} \delta p \, (J_{\boldsymbol{x}} - 1) \, d\Omega_0 = 0.
\end{aligned} \tag{28}$$

It is well-known that the functional spaces $\{\mathbb{V}^{\boldsymbol{x}}, \mathbb{V}^p\}$ must be carefully chosen in order to fulfil the *inf-sup* or LBB condition [70, 71]. In this work, we circumvent the *inf-sup* condition by means of a Streamline Upwind Petrov-Galerkin (SUPG) stabilisation [50, 51, 72, 73], by introducing the stabilised virtual field $\delta\boldsymbol{x}^{\mathrm{st}}$ as

$$\delta\boldsymbol{x}^{st} = \delta\boldsymbol{x} - \tau_{\boldsymbol{x}} (\boldsymbol{H}_{\boldsymbol{x}} \boldsymbol{\nabla}_0 \delta p); \qquad \tau_{\boldsymbol{x}} = \frac{\alpha h}{2\mu_0}, \tag{29}$$

where $h$ represents the characteristic length of the element of the mesh, $\mu_0$ is a positive material constant taken as the shear modulus in the origin of deformations and $\alpha$ the dimensionless stabilisation parameter. The use of $\delta\boldsymbol{x}^{st}$ in the specific case of a $\{P_1, P_1\}$ interpolation for the $\{\boldsymbol{x}, p\}$ fields leads to a modified (stabilised) expression for $\mathcal{W}_p$ as

$$\mathcal{W}_p^{st} = \int_{\Omega_0} \delta p \, (J_{\boldsymbol{x}} - 1) \, d\Omega_0 - \int_{\Omega_0} \tau_{\boldsymbol{x}} (\boldsymbol{H}_{\boldsymbol{x}} \boldsymbol{\nabla}_0 \delta p) \cdot (\boldsymbol{H}_{\boldsymbol{x}} \boldsymbol{\nabla}_0 p) \, d\Omega_0 = 0. \tag{30}$$

### *4.3. Super enhanced mixed formulations: **MFA**-$T_a$ for active stress and **MFA**-$\gamma$ for active strain*

We now briefly revisit the two mixed formulations introduced in [1] in the context of cardiac electro-mechanics. These formulations do not exhibit shear and volumetric locking and have been shown to be very convenient in this context. In the **MFA**-$T_a$ formulation, the unknown fields are $\boldsymbol{\mathcal{U}} = \{\boldsymbol{x}, \phi, p\} \in \mathbb{V}^{\boldsymbol{x}} \times \mathbb{V}^{\phi} \times \mathbb{V}^p$, new fields $\boldsymbol{\mathcal{D}} = \{\boldsymbol{F}, \boldsymbol{H}, J, \boldsymbol{A}\} \in \mathbb{V}^{\boldsymbol{\mathcal{D}}}$ and their dual $\boldsymbol{\Sigma}_{\boldsymbol{\mathcal{D}}} = \{\boldsymbol{\Sigma}_{\boldsymbol{F}}, \boldsymbol{\Sigma}_{\boldsymbol{H}}, \Sigma_J, \boldsymbol{\Sigma}_{\boldsymbol{A}}\} \in \mathbb{V}^{\boldsymbol{\mathcal{D}}}$, with $\mathbb{V}^{\boldsymbol{\mathcal{D}}} = \mathbb{V}^{\boldsymbol{F}} \times \mathbb{V}^{\boldsymbol{H}} \times \mathbb{V}^J \times \mathbb{V}^{\boldsymbol{A}}$ as

$$\begin{aligned}
&\mathbb{V}^{\boldsymbol{F}} = \left\{\boldsymbol{F} : \Omega_0 \to \mathbb{R}^{3\times3}; \quad (\boldsymbol{F})_{iI} \in \mathbb{L}_2(\Omega_0)\right\}; && \mathbb{V}^{\boldsymbol{H}} = \left\{\boldsymbol{H} : \Omega_0 \to \mathbb{R}^{3\times3}; \quad (\boldsymbol{H})_{iI} \in \mathbb{L}_2(\Omega_0)\right\}; \\
&\mathbb{V}^J = \{J : \Omega_0 \to \mathbb{R}; \qquad J \in \mathbb{L}_2(\Omega_0)\}; && \mathbb{V}^{\boldsymbol{A}} = \left\{\boldsymbol{A} : \Omega_0 \to \mathbb{R}^3; \quad (\boldsymbol{A})_I \in \mathbb{L}_2(\Omega_0)\right\},
\end{aligned} \tag{31}$$

where both sets of additional fields $\boldsymbol{\mathcal{D}}$ and $\boldsymbol{\Sigma}_{\boldsymbol{\mathcal{D}}}$ are forced to converge weakly to

$$\{\boldsymbol{F}, \boldsymbol{H}, J, \boldsymbol{A}\} \rightharpoonup \{\boldsymbol{F}_{\boldsymbol{x}}, \boldsymbol{H}_{\boldsymbol{x}}, J_{\boldsymbol{x}}, \boldsymbol{\nabla}_0\phi\}; \qquad \{\boldsymbol{\Sigma}_{\boldsymbol{F}}, \boldsymbol{\Sigma}_{\boldsymbol{H}}, \Sigma_J, \boldsymbol{\Sigma}_{\boldsymbol{A}}\} \rightharpoonup \{\partial_{\boldsymbol{F}} W, \partial_{\boldsymbol{H}} W, \partial_J W, \boldsymbol{DA}\}. \quad (32)$$

Notice that $(32)_a$ represent the compatibility conditions whereas $(32)_b$ represent the constitutive equations. In addition to the previously defined virtual fields $\delta\boldsymbol{\mathcal{V}} = \{\delta\boldsymbol{x}, \delta\phi, \delta p\} \in \mathbb{V}_0^{\boldsymbol{x}} \times \mathbb{V}^{\phi} \times \mathbb{V}^{p}$, further required virtual fields are $\delta\boldsymbol{\mathcal{D}} = \{\delta\boldsymbol{F}, \delta\boldsymbol{H}, \delta J, \delta\boldsymbol{A}\} \in \mathbb{V}^{\boldsymbol{\mathcal{D}}}$ and their dual $\delta\boldsymbol{\Sigma}_{\boldsymbol{\mathcal{D}}} = \{\delta\boldsymbol{\Sigma}_{\boldsymbol{F}}, \delta\boldsymbol{\Sigma}_{\boldsymbol{H}}, \delta\Sigma_J, \delta\boldsymbol{\Sigma}_{\boldsymbol{A}}\} \in \mathbb{V}^{\boldsymbol{\mathcal{D}}}$. In this formulation, weak forms $\mathcal{W}_{\boldsymbol{\mathcal{U}}} = \{\mathcal{W}_{\boldsymbol{x}}, \mathcal{W}_{\phi}, \mathcal{W}_{p}\}$ are identical to those in (28), except that the stress tensor $\boldsymbol{P}$ is now defined as in (10) but in terms of the unknown fields $\{\boldsymbol{\Sigma}_{\boldsymbol{F}}, \boldsymbol{\Sigma}_{\boldsymbol{H}}, \Sigma_J, \boldsymbol{F}\}$ as

$$\boldsymbol{P} = \boldsymbol{\Sigma}_{\boldsymbol{F}} + \boldsymbol{\Sigma}_{\boldsymbol{H}} \boldsymbol{\times} \boldsymbol{F}_{\boldsymbol{x}} + \Sigma_J \boldsymbol{H}_{\boldsymbol{x}} + T_a(\phi)\, \boldsymbol{F}\boldsymbol{f}_0 \otimes \boldsymbol{f}_0. \quad (33)$$

In order to enforce (32), two sets of weak forms denoted as $\mathcal{W}_{\boldsymbol{\Sigma}_{\boldsymbol{\mathcal{D}}}} = \{\mathcal{W}_{\boldsymbol{\Sigma}_{\boldsymbol{F}}}, \mathcal{W}_{\boldsymbol{\Sigma}_{\boldsymbol{H}}}, \mathcal{W}_{\Sigma_J}, \mathcal{W}_{\boldsymbol{\Sigma}_{\boldsymbol{A}}}\}$ and $\mathcal{W}_{\boldsymbol{\mathcal{D}}} = \{\mathcal{W}_{\boldsymbol{F}}, \mathcal{W}_{\boldsymbol{H}}, \mathcal{W}_{J}, \mathcal{W}_{\boldsymbol{A}}\}$, are added

$$\begin{aligned}
\mathcal{W}_{\boldsymbol{\Sigma}_{\boldsymbol{F}}} &= \int_{\Omega_0} \delta\boldsymbol{\Sigma}_{\boldsymbol{F}} : (\boldsymbol{F}_x - \boldsymbol{F})\, d\Omega_0; & \mathcal{W}_{\boldsymbol{F}} &= \int_{\Omega_0} \delta\boldsymbol{F} : (\partial_{\boldsymbol{F}} W - \boldsymbol{\Sigma}_{\boldsymbol{F}})\, d\Omega_0; \\
\mathcal{W}_{\boldsymbol{\Sigma}_{\boldsymbol{H}}} &= \int_{\Omega_0} \delta\boldsymbol{\Sigma}_{\boldsymbol{H}} : (\boldsymbol{H}_x - \boldsymbol{H})\, d\Omega_0; & \mathcal{W}_{\boldsymbol{H}} &= \int_{\Omega_0} \delta\boldsymbol{H} : (\partial_{\boldsymbol{H}} W - \boldsymbol{\Sigma}_{\boldsymbol{H}})\, d\Omega_0; \\
\mathcal{W}_{\Sigma_J} &= \int_{\Omega_0} \delta\Sigma_J\, (J_x - J)\, d\Omega_0; & \mathcal{W}_{J} &= \int_{\Omega_0} \delta J\, (\partial_J W - \Sigma_J)\, d\Omega_0; \\
\mathcal{W}_{\boldsymbol{\Sigma}_{\boldsymbol{A}}} &= \int_{\Omega_0} \delta\boldsymbol{\Sigma}_{\boldsymbol{A}} \cdot (\boldsymbol{\nabla}_0\phi - \boldsymbol{A})\, d\Omega_0; & \mathcal{W}_{\boldsymbol{A}} &= \int_{\Omega_0} \delta\boldsymbol{A} \cdot (\boldsymbol{DA} - \boldsymbol{\Sigma}_{\boldsymbol{A}})\, d\Omega_0,
\end{aligned} \quad (34)$$

where $W$ depends on the unknown fields $\{\boldsymbol{F}, \boldsymbol{H}, J\}$. Finally, the second order diffusion tensor $\boldsymbol{D}$ in $(34)_i$ adopts an equivalent expression to that in (15) in terms of $\{\boldsymbol{H}, J\}$ as

$$\boldsymbol{D}(\boldsymbol{H}, J) = d_{\text{iso}} J^{-2} \boldsymbol{H}^T \boldsymbol{H} + d_{\text{ani}} \boldsymbol{f}_0 \otimes \boldsymbol{f}_0. \quad (35)$$

Similarly, in the **MFA-$\gamma$** mixed formulation, $\mathcal{W}_{\boldsymbol{\mathcal{U}}} = \{\mathcal{W}_{\boldsymbol{x}}, \mathcal{W}_{\phi}, \mathcal{W}_{p}\}$ are identical to those in (28) but the first Piola-Kirchhoff stress tensor $\boldsymbol{P}$ is now defined as,

$$\boldsymbol{P} = \boldsymbol{\Sigma}_{\boldsymbol{F}} + \boldsymbol{\Sigma}_{\boldsymbol{H}} \boldsymbol{\times} \boldsymbol{F}_{\boldsymbol{x}} + \Sigma_J \boldsymbol{H}_{\boldsymbol{x}}. \quad (36)$$

The weak forms $\mathcal{W}_{\boldsymbol{\Sigma}_{\boldsymbol{\mathcal{D}}}} = \{\mathcal{W}_{\boldsymbol{\Sigma}_{\boldsymbol{F}}}, \mathcal{W}_{\boldsymbol{\Sigma}_{\boldsymbol{H}}}, \mathcal{W}_{\Sigma_J}, \mathcal{W}_{\boldsymbol{\Sigma}_{\boldsymbol{A}}}\}$ and $\mathcal{W}_{\boldsymbol{A}}$ are equivalent to those in (34). However, the multiplicative nature of the active strain approach leads to alternative expressions for $\{\mathcal{W}_{\boldsymbol{F}}, \mathcal{W}_{\boldsymbol{H}}, \mathcal{W}_{J}\}$ as (refer to (13))

$$\begin{aligned}
\mathcal{W}_{\boldsymbol{F}} &= \int_{\Omega_0} \delta\boldsymbol{F} : \left(\partial_{\boldsymbol{F}} W^E - \boldsymbol{\Sigma}_{\boldsymbol{F}}\right) d\Omega_0; \\
\mathcal{W}_{\boldsymbol{H}} &= \int_{\Omega_0} \delta\boldsymbol{H} : \left(\partial_{\boldsymbol{H}} W^E - \boldsymbol{\Sigma}_{\boldsymbol{H}}\right) d\Omega_0; \\
\mathcal{W}_{J} &= \int_{\Omega_0} \delta J\, \left(\partial_J W^E - \Sigma_J\right) d\Omega_0,
\end{aligned} \quad (37)$$

where $W^E$ depends upon $\{\boldsymbol{F}, \boldsymbol{H}, J, \boldsymbol{F}^A, \boldsymbol{H}^A, J^A\}$ and not on $\{\boldsymbol{F}_{\boldsymbol{x}}, \boldsymbol{H}_{\boldsymbol{x}}, J_{\boldsymbol{x}}, \boldsymbol{F}^A, \boldsymbol{H}^A, J^A\}$ as in (12). Notice in (37) the extra dependence with respect to the field $\phi$ (due to the dependence of $W^E$ with respect to $\{\boldsymbol{F}^A, \boldsymbol{H}^A, J^A\}$, in contrast to those in (34).

## 5. Computational implementation

This Section presents the discretisations in space and time used in this work. The discretisation in space follows the Finite Element method and for the discretisation in time the backward Euler method is used. Due to the coupled (electro-mechanical) nature of the problem, alternative solution strategies can be put forward, such as monolithic and staggered, which will be presented in detail.

### 5.1. Finite Element spatial discretisation

The computational domain $\Omega_0$ is tessellated into a finite number of non-overlapping elements $e \in \mathbb{E}$ such that

$$\Omega_0 \approx \Omega_0^h = \bigcup_{e \in \mathbb{E}} \Omega_0^e. \tag{38}$$

The unknown fields for the two-field $\boldsymbol{x}$-$\phi$ formulation (Section 4.1) are discretised as $\{\boldsymbol{x}, \phi\} \in \mathbb{V}^{\boldsymbol{x}^h} \times \mathbb{V}^{\phi^h}$ with

$$\mathbb{V}^{\boldsymbol{x}^h} = \{\boldsymbol{x} \in \mathbb{V}^{\boldsymbol{x}};\ \ \boldsymbol{x} = \sum\nolimits_{a=1}^{n_{\boldsymbol{x}}} \boldsymbol{x}_a N_a^{\boldsymbol{x}}\}; \qquad \mathbb{V}^{\phi^h} = \{\phi \in \mathbb{V}^{\phi};\ \ \phi = \sum\nolimits_{a=1}^{n_{\phi}} \phi_a N_a^{\phi}\}, \tag{39}$$

where $a$ denotes the nodes used for the interpolation of the above variables and $n_{(\bullet)}$, the number of nodes (per element) associated with the variable $(\bullet)$. In addition, for the stabilised three-field $\boldsymbol{x}$-$\phi$-$p$ formulation (Section 4.2), the pressure field is discretised as $p \in \mathbb{V}^{p^h}$ with

$$\mathbb{V}^{p^h} = \{p \in \mathbb{V}^{p};\ \ p = \sum\nolimits_{a=1}^{n_p} p_a N_a^{p}\}. \tag{40}$$

Finally, the additional set of unknown fields $\boldsymbol{\mathcal{D}}$ and $\boldsymbol{\Sigma_{\mathcal{D}}}$ introduced in the super enhanced mixed **MFA-**$T_a$ and **MFA-**$\gamma$ formulations (Section 4.3) are discretised as $\boldsymbol{\mathcal{D}} \in \mathbb{V}^{\boldsymbol{\mathcal{D}}^h}$ and $\boldsymbol{\Sigma_{\mathcal{D}}} \in \mathbb{V}^{\boldsymbol{\mathcal{D}}^h}$, where $\mathbb{V}^{\boldsymbol{\mathcal{D}}^h} = \mathbb{V}^{\boldsymbol{F}^h} \times \mathbb{V}^{\boldsymbol{H}^h} \times \mathbb{V}^{J^h} \times \mathbb{V}^{\boldsymbol{A}^h}$ with

$$\begin{aligned}
&\mathbb{V}^{\boldsymbol{F}} = \{\boldsymbol{F} \in \mathbb{V}^{\boldsymbol{F}};\quad \boldsymbol{F} = \sum\nolimits_{a=1}^{n_{\boldsymbol{F}}} \boldsymbol{F}_a N_a^{\boldsymbol{F}}\}; \quad \mathbb{V}^{\boldsymbol{H}} = \{\boldsymbol{H} \in \mathbb{V}^{\boldsymbol{H}};\quad \boldsymbol{H} = \sum\nolimits_{a=1}^{n_{\boldsymbol{H}}} \boldsymbol{H}_a N_a^{\boldsymbol{H}}\};\\
&\mathbb{V}^{J} = \{J \in \mathbb{V}^{J};\quad J = \sum\nolimits_{a=1}^{n_{J}} J_a N_a^{J}\}; \quad \mathbb{V}^{\boldsymbol{A}} = \{\boldsymbol{A} \in \mathbb{V}^{\boldsymbol{A}};\quad \boldsymbol{A} = \sum\nolimits_{a=1}^{n_{\boldsymbol{A}}} \boldsymbol{A}_a N_a^{\boldsymbol{A}}\}.
\end{aligned} \tag{41}$$

Similarly, appropriate functional spaces are used for the test functions $\{\delta\boldsymbol{x}, \delta\phi, \delta p\} \in \mathbb{V}_0^{\boldsymbol{x}^h} \times \mathbb{V}^{\phi^h} \times \mathbb{V}^{p^h}$ and $\delta\boldsymbol{\mathcal{D}} \in \mathbb{V}^{\boldsymbol{\mathcal{D}}^h}$ and $\delta\boldsymbol{\Sigma_{\mathcal{D}}} \in \mathbb{V}^{\boldsymbol{\mathcal{D}}^h}$, with

$$\mathbb{V}_0^{\boldsymbol{x}^h} = \{\boldsymbol{x} \in \mathbb{V}^{\boldsymbol{x}^h};\quad \boldsymbol{x} = \boldsymbol{0};\ \text{on}\ \partial_{\boldsymbol{x}}\Omega_0\}. \tag{42}$$

Three Finite Elements discretisations will be tested and compared in the following examples, namely: (i) $\{P_1, P_1\}$ interpolation for the fields $\{\boldsymbol{x}, \phi\}$ when using the two-field $\boldsymbol{x}$-$\phi$ formulation (Section 4.1); (ii) $\{P_1, P_1, P_1\}$ interpolation for the unknown fields $\{\boldsymbol{x}, \phi, p\}$ when using the stabilised three-field $\boldsymbol{x}$-$\phi$-$p$ formulation (Section 4.2); (iii) $\{P_2, P_2, P_0\}$ interpolation for the fields $\{\boldsymbol{x}, \phi, p\}$ and piecewise discontinuous $\{P_1, P_1, P_0, P_1\}$ interpolation for the fields $\{\boldsymbol{F}, \boldsymbol{H}, J, \boldsymbol{A}\}$ and their dual $\{\boldsymbol{\Sigma_F}, \boldsymbol{\Sigma_H}, \Sigma_J, \boldsymbol{\Sigma_A}\}$ when using the super enhanced mixed **MFA-**$T_a$and **MFA-**$\gamma$ formulations. For the **MFA** formulations, a tailor-made static condensation procedure [1] is used in order to condense out the (element-wise) discontinuous fields without unnecessarily increasing the number of unknowns of the solver.

### 5.2. Computational coupling strategies

For the advancement in time of the electro-mechanical fields $\boldsymbol{x}$ and $\phi$, a one-step backward Euler method is used, progressing the solution from time step $t_n$ to $t_{n+1}$ with a time step $\Delta t = t_{n+1} - t_n$. Three coupling strategies will be explored and compared in the search of an optimum methodology which can render accurate results without a prohibitively expensive computational solver, namely: (a) monolithic approach; (b) staggered approach and (c) staggered linearised approach. Algorithms 1 and 2 will be used to illustrate the various coupling strategies.

*5.2.1. Monolithic approach*

In a monolithic implementation, both electrical and mechanical fields are advanced simultaneously from a time step $t_n$ to the next $t_{n+1}$ with $\Delta t = t_{n+1} - t_n$. Both in the two-field $\boldsymbol{x}$-$\phi$ and stabilised three-field $\boldsymbol{x}$-$\phi$-$p$ formulations, the assembly of the residual vector $\mathbf{T}$ and tangent stiffness matrix $\mathbf{K}$ resulting from the discretisation of the electro-mechanical weak forms $\mathcal{W}_{\boldsymbol{\mathcal{U}}}$ (in (26) or $(28)_{a,b}$ and (30)) is carried out simultaneously at each iteration $k$ of the Newton-Raphson algorithm, and the values of the unknown fields $\boldsymbol{\mathcal{U}}$ are updated iteratively[5].

For the super enhanced mixed **MFA**-$T_a$ and **MFA**-$\gamma$ formulations, contributions $\mathbf{T}$ and $\mathbf{K}$ associated with the weak forms $\{\mathcal{W}_{\boldsymbol{\mathcal{U}}}, \mathcal{W}_{\boldsymbol{\mathcal{D}}}, \mathcal{W}_{\boldsymbol{\Sigma_{\mathcal{D}}}}\}$ are assembled at each iteration $k$ of the Newton-Raphson algorithm. A static condensation procedure (condensing out the degrees of freedom for $\boldsymbol{\mathcal{D}}$ and $\boldsymbol{\Sigma_{\mathcal{D}}}$) is carried out and the values of the fields $\boldsymbol{\mathcal{U}}$ are updated. Immediately after this, the remaining fields $\{\boldsymbol{\mathcal{D}}, \boldsymbol{\Sigma_{\mathcal{D}}}\}$ are also updated (in a typical second stage of the static condensation procedure). The reader is referred to the pseudo-code version of the monolithic solver depicted in Algorithm 1 for further details.

*5.2.2. Staggered approach*

In a staggered implementation, electrical and mechanical fields are solved separately in order to advance the solution from a time step $t_n$ to the next $t_{n+1}$ with $\Delta t = t_{n+1} - t_n$. Due to the higher time variability (specially in the vicinity of sharp gradients) of the transmembrane potential in comparison with that expected for the deformations of the myocardium, a time sub-stepping approach is used whereby the transmembrane potential is advanced in time for $N$ time steps $\Delta t$ during which the mechanical fields are not updated (e.g. stay *frozen*). This is equivalent to consider a larger pseudo-mechanical time step $\Delta t_m = N\Delta t$. Thus, for the two-field $\boldsymbol{x}$-$\phi$ and stabilised three-field $\boldsymbol{x}$-$\phi$-$p$ formulations, the electrical problem is advanced first during $N$ time sub-increments before proceeding to the solution of the *Mechanical Problem*. As such, for every electrical time step, the assembly of the residual vector $\mathbf{T}$ and tangent matrix $\mathbf{K}$ resulting from the discretisation of the weak form $\mathcal{W}_\phi$ is first performed. This is carried out at each iteration $k$ of the Newton-Raphson algorithm associated within each (electrical) time step $\Delta t$. Then, we proceed to the update the value of the transmembrane potential $\phi$.

After $N$ electrical time sub-steps (see conditional statement in the pseudo-code in Algorithm 2), we freeze the field $\phi$ and proceed to the solution of the mechanical fields through a Newton-Raphson algorithm. We assemble the residual vector $\mathbf{T}$ and tangent stiffness matrix $\mathbf{K}$ associated with the discretisation of the (mechanical) weak forms $\mathcal{W}_{\boldsymbol{\mathcal{U}}_m} = \{\mathcal{W}_{\boldsymbol{x}}, \mathcal{W}_p\}$ at each iteration $k$. Then, we update the value of $\boldsymbol{\mathcal{U}}_m = \{\boldsymbol{x}, p\}$. An identical procedure is established for the super enhanced mixed **MFA**-$T_a$ and **MFA**-$\gamma$ formulations. The reader is referred to the pseudo-code version of the monolithic solver shown in Algorithm 2 for further details.

*5.2.3. Staggered linearised approach*

Most of the computational time in the staggered approach is spent in the solution of the so-called *Mechanical Problem*, due to the assembly, possible static condensation and solution of the system of equations. Inspired by the work in [63–65], a possible strategy to reduce this time consists of approximating this problem by its consistent linearisation within the mechanical time step increment $\Delta t_m = N\Delta t$. For instance, for the $\boldsymbol{x}$-$\phi$-$p$ formulation, the linearisation of the two

[5]Note that the last (stabilisation) term in (30) can potentially be treated in a explicit manner in order to preserve the symmetry of the solver, namely, the cofactor terms $\boldsymbol{H}_{\boldsymbol{x}}$ are evaluated at time step $t_n$

weak forms associated with the fields $\boldsymbol{x}$ and $p$ in $(28)_a$ and (30) can be formulated as follows,

$$\begin{aligned}\mathcal{W}_{\boldsymbol{x}}^{\text{lin}} &= \int_{\Omega_0} \left(\boldsymbol{P}^{\text{lin}} + (p\boldsymbol{H}_{\boldsymbol{x}})^{\text{lin}}\right) : \boldsymbol{\nabla}_0 \delta\boldsymbol{x}\, d\Omega_0 - \int_{\Omega_0} \delta\boldsymbol{x}\cdot\boldsymbol{b}_0\, d\Omega_0 - \int_{\partial\Omega_0} \delta\boldsymbol{x}\cdot\boldsymbol{t}_0\, d\Gamma = 0;\\ \mathcal{W}_p^{st,\text{lin}} &= \int_{\Omega_0} \delta p \left(J_{\boldsymbol{x}}^{\text{lin}} - 1\right) d\Omega_0 - \int_{\Omega_0} \tau_{\boldsymbol{x}} \left[(\boldsymbol{H}_{\boldsymbol{x}}\boldsymbol{\nabla}_0\delta p)\cdot(\boldsymbol{H}_{\boldsymbol{x}}\boldsymbol{\nabla}_0 p)\right]^{\text{lin}} d\Omega_0 = 0\end{aligned} \tag{43}$$

where we have replaced $\boldsymbol{P}$ and $p\boldsymbol{H}_{\boldsymbol{x}}$ in $(28)_a$ with their suitable linearised counterparts $\boldsymbol{P}^{\text{lin}}$ and $(p\boldsymbol{H}_{\boldsymbol{x}})^{\text{lin}}$, respectively, and $J_{\boldsymbol{x}}$ and $(\boldsymbol{H}_{\boldsymbol{x}}\boldsymbol{\nabla}_0\delta p)\cdot(\boldsymbol{H}_{\boldsymbol{x}}\boldsymbol{\nabla}_0 p)$ in (30) with their linearised terms $J_{\boldsymbol{x}}^{\text{lin}}$ and $[(\boldsymbol{H}_{\boldsymbol{x}}\boldsymbol{\nabla}_0\delta p)\cdot(\boldsymbol{H}_{\boldsymbol{x}}\boldsymbol{\nabla}_0 p)]^{\text{lin}}$, respectively. These linearised fields can be expanded as,

$$\begin{aligned}\boldsymbol{P}^{\text{lin}} &= \boldsymbol{P}^* + \boldsymbol{\mathcal{C}}^* : \boldsymbol{\nabla}_0\Delta\boldsymbol{x} + (\partial_\phi \boldsymbol{P})|^*(\phi^{**} - \phi^*);\\ (p\boldsymbol{H}_x)^{\text{lin}} &= p^*\boldsymbol{H}_{\boldsymbol{x}}^* + p^*\boldsymbol{F}_{\boldsymbol{x}}^* \times \boldsymbol{\nabla}_0\Delta\boldsymbol{x} + \boldsymbol{H}_{\boldsymbol{x}}^*\Delta p;\\ J_{\boldsymbol{x}}^{\text{lin}} &= J_{\boldsymbol{x}}^* + \boldsymbol{H}_{\boldsymbol{x}}^* : \boldsymbol{\nabla}_0\Delta\boldsymbol{x};\\ [(\boldsymbol{H}_{\boldsymbol{x}}\boldsymbol{\nabla}_0\delta p)\cdot(\boldsymbol{H}_{\boldsymbol{x}}\boldsymbol{\nabla}_0 p)]^{\text{lin}} &= (\boldsymbol{H}_{\boldsymbol{x}}^*\boldsymbol{\nabla}_0\delta p)\cdot(\boldsymbol{H}_{\boldsymbol{x}}^*\boldsymbol{\nabla}_0\Delta p) + ((\boldsymbol{F}_{\boldsymbol{x}}^* \times \boldsymbol{\nabla}_0\Delta\boldsymbol{x})\boldsymbol{\nabla}_0\delta p)\cdot(\boldsymbol{H}_{\boldsymbol{x}}^*\boldsymbol{\nabla}_0 p^*)\\ &\quad + (\boldsymbol{H}_{\boldsymbol{x}}^*\boldsymbol{\nabla}_0\delta p)\cdot((\boldsymbol{F}_{\boldsymbol{x}}^* \times \boldsymbol{\nabla}_0\Delta\boldsymbol{x})\boldsymbol{\nabla}_0 p^*),\end{aligned} \tag{44}$$

where upper indices $(*)$ and $(**)$ are used to indicate the time instants upon which the evaluation took place, namely, the beginning and the end of the considered mechanical time step, respectively[6]. In addition, the symbol $\Delta$ is used to denote the variation of a field within the given mechanical time step. Note that the linearisation of the stabilisation term in $(44)_d$ can be simplified to just the first term on its right hand side in order to preserve the symmetry of the solver, with its ensuing time reduction in terms of assembly. Moreover, notice that alternative approximations for the last term on the right hand side of above equation $(44)_a$ are possible. For instance, high order terms can be further included into above Taylor series expansion, namely, $1/p!\ (\partial^p_{\phi\ldots\phi}\boldsymbol{P})|^n(\phi^{**} - \phi^*)^p$ or a non-consistent approximation of the term $\partial_\phi\boldsymbol{P}$ can be adopted whereby whilst the deformation is evaluated at time instant $(*)$, the transmembrane potential is evaluated at time instant $(**)$. Similarly, for the super enhanced **MFA** formulations presented in Section 4.3, the linearised version of the compatibility and constitutive equations in (34) are

$$\begin{aligned}\mathcal{W}_{\boldsymbol{\Sigma}_{\boldsymbol{F}}} &= \int_{\Omega_0} \delta\boldsymbol{\Sigma}_{\boldsymbol{F}} : (\boldsymbol{F}_x - \boldsymbol{F})\, d\Omega_0; & \mathcal{W}_{\boldsymbol{F}} &= \int_{\Omega_0} \delta\boldsymbol{F} : \left(\partial_{\boldsymbol{F}} W^{\text{lin}} - \boldsymbol{\Sigma}_{\boldsymbol{F}}\right) d\Omega_0;\\ \mathcal{W}_{\boldsymbol{\Sigma}_{\boldsymbol{H}}} &= \int_{\Omega_0} \delta\boldsymbol{\Sigma}_{\boldsymbol{H}} : \left(\boldsymbol{H}_{\boldsymbol{x}}^{\text{lin}} - \boldsymbol{H}\right) d\Omega_0; & \mathcal{W}_{\boldsymbol{H}} &= \int_{\Omega_0} \delta\boldsymbol{H} : \left(\partial_{\boldsymbol{H}} W^{\text{lin}} - \boldsymbol{\Sigma}_{\boldsymbol{H}}\right) d\Omega_0;\\ \mathcal{W}_{\Sigma_J} &= \int_{\Omega_0} \delta\Sigma_J \left(J_{\boldsymbol{x}}^{\text{lin}} - J\right) d\Omega_0; & \mathcal{W}_J &= \int_{\Omega_0} \delta J \left(\partial_J W^{\text{lin}} - \Sigma_J\right) d\Omega_0,\end{aligned} \tag{45}$$

with $J_{\boldsymbol{x}}^{\text{lin}}$ defined above in $(44)_c$ and $\boldsymbol{H}_{\boldsymbol{x}}^{\text{lin}} = \boldsymbol{H}_{\boldsymbol{x}}^* + \boldsymbol{F}_{\boldsymbol{x}}^* \times \boldsymbol{\nabla}_0\Delta\boldsymbol{x}$. The remaining linearised terms in (45) are obtained as

$$\begin{bmatrix} \partial_{\boldsymbol{F}} W \\ \partial_{\boldsymbol{H}} W \\ \partial_J W \end{bmatrix}^{\text{lin}} = \begin{bmatrix} \partial_{\boldsymbol{F}} W \\ \partial_{\boldsymbol{H}} W \\ \partial_J W \end{bmatrix}^* + [\mathbb{H}_W]^* \begin{bmatrix} :\Delta\boldsymbol{F} \\ :\Delta\boldsymbol{H} \\ \Delta J \end{bmatrix}, \tag{46}$$

where $[\mathbb{H}_W]^*$ represents the Hessian operator of $W$ (with respect to the triad of kinematic fields $\{\boldsymbol{F}, \boldsymbol{H}, J\}$) [1] evaluated at the time instant $(*)$.

[6] In above formulae (44), we have made use of the directional derivatives of the cofactor and the Jacobian in terms of their simpler cross product $\times$ expressions [59].

**Procedure** *Monolithic Solver*

Initialise $\boldsymbol{\mathcal{U}} = \{\boldsymbol{x}, \phi, p\}$
Initialise $\boldsymbol{\mathcal{D}}$ and $\boldsymbol{\Sigma_{\mathcal{D}}}$ (*if* **MFA**-$T_a$/**MFA**-$\gamma$ *formulation*)
Initialise $\boldsymbol{q}$ according to initial conditions $(3)_c$
Set $t = 0$ and $n = 1$ /*(n:=*time iteration*)*/
/* ———————————— *Start Time loop* ———————————— */
**while** $t < t_{max}$ **do**
    /* ———————— *Start Newton-Raphson algorithm* ————————*/
    $i = 1$ /*(*Newton-Raphson iteration*)*/
    **while** $\|\Delta\boldsymbol{\mathcal{U}}\| >$ *tolerance* **do**
        **forall** *elements* **do**
            Compute $\boldsymbol{q}$ and $f_\phi$ and active terms $T_a$ or $\gamma_{\boldsymbol{f}_0}$
            /*———————— Monolithic Local Assembly————————*/
            -Compute $\mathbf{T}$ and $\mathbf{K}$ from weak forms $\mathcal{W}_{\boldsymbol{\mathcal{U}}}$ in 4.1 (*if* $\boldsymbol{x}$-$p$ *formulation*)
            -Compute $\mathbf{T}$ and $\mathbf{K}$ from weak forms $\mathcal{W}_{\boldsymbol{\mathcal{U}}}$ in 4.2 (*if* $\boldsymbol{x}$-$p$-$\phi$ *formulation*)
            -Compute $\mathbf{T}$ and $\mathbf{K}$ for weak forms $\{\mathcal{W}_{\boldsymbol{\mathcal{U}}}, \mathcal{W}_{\boldsymbol{\mathcal{D}}}, \mathcal{W}_{\boldsymbol{\Sigma_{\mathcal{D}}}}\}$ in 4.3 (*if* **MFA**-$T_a$ *formulation*). Perform static condensation procedure
            -Compute $\mathbf{T}$ and $\mathbf{K}$ for weak forms $\{\mathcal{W}_{\boldsymbol{\mathcal{U}}}, \mathcal{W}_{\boldsymbol{\mathcal{D}}}, \mathcal{W}_{\boldsymbol{\Sigma_{\mathcal{D}}}}\}$ in 4.3 (*if* **MFA**-$T_a$ *formulation*). Perform static condensation procedure
        **end**
        Global assembly of residuals and matrices
        Obtain incremental $\Delta\boldsymbol{\mathcal{U}}_i^n$ (iterative solver)
        Update $\boldsymbol{\mathcal{U}}_{i+1}^n = \boldsymbol{\mathcal{U}}_i^n + \Delta\boldsymbol{\mathcal{U}}_i^n$
        Update $\boldsymbol{\mathcal{D}}_i^n$ and $\boldsymbol{\Sigma}_{\boldsymbol{\mathcal{D}}_i}^n$: static condensation (**MFA**-$T_a$/**MFA**-$\gamma$)
    **end**
    Update $\boldsymbol{\mathcal{U}}$, $\boldsymbol{q}$: $t_{n+1} \to t_n$
    $\boldsymbol{\mathcal{D}}$ and $\boldsymbol{\Sigma_{\mathcal{D}}}$: $t_{n+1} \to t_n$
    $t_{n+1} = t_n + \Delta t$, $n+ = 1$
    Adjust new $\Delta t$ according to changes in $\boldsymbol{q}$
**end**

**Algorithm 1:** Pseudo-code for the Monolithic Solver

**Procedure** *Staggered Solver*

Initialise $\boldsymbol{\mathcal{U}}_e = \phi$ and $\boldsymbol{\mathcal{U}}_m = \{\boldsymbol{x}, p\}$

Initialise $\boldsymbol{\mathcal{D}}_e = \boldsymbol{A}$, $\boldsymbol{\Sigma}_{\boldsymbol{\mathcal{D}}_e} = \boldsymbol{\Sigma}_{\boldsymbol{A}}$, $\boldsymbol{\mathcal{D}}_m = \{\boldsymbol{F}, \boldsymbol{H}, J\}$ and $\boldsymbol{\Sigma}_{\boldsymbol{\mathcal{D}}_m} = \{\boldsymbol{\Sigma}_{\boldsymbol{F}}, \boldsymbol{\Sigma}_{\boldsymbol{H}}, \Sigma_J\}$ (**MFA**-$T_a$/**MFA**-$\gamma$ *formulation*)

Initialise $\boldsymbol{q}$ according to initial conditions $(3)_c$

Set $t = 0$

Set $n_e = 1$ and $n_m = 1$ /*(*time iteration for electrical and mechanical staggered problems*)*/

**while** $t < t_{max}$ /*(*Start Time loop*)*/ **do**

/*————————*Solve Electrical problem*————————*/

Freeze $\boldsymbol{\mathcal{U}}_m^{n_m}$ and $\{\boldsymbol{\mathcal{D}}_m^{n_m}, \boldsymbol{\Sigma}_{\boldsymbol{\mathcal{D}}_m}^{n_m}\}$ (**MFA**-$T_a$/**MFA**-$\gamma$ *formulation*)

$i = 1$ /*(*Newton-Raphson iteration*)*/

**while** $\|\Delta\boldsymbol{\mathcal{U}}_e\| >$ *tolerance* **do**

**forall** *elements* **do**

Compute $\boldsymbol{q}$ and $f_\phi$ and active terms $T_a$ or $\gamma_{\boldsymbol{f}_0}$

-Compute $\mathbf{T}$ and $\mathbf{K}$ from weak form $\mathcal{W}_\phi$ in 4.1 (*$\boldsymbol{x}$-$p$ formulation*)

-Compute $\mathbf{T}$ and $\mathbf{K}$ from weak form $\mathcal{W}_\phi$ in 4.2 (*$\boldsymbol{x}$-$p$-$\phi$ formulation*)

-Compute $\mathbf{T}$ and $\mathbf{K}$ for weak forms $\{\mathcal{W}_\phi, \mathcal{W}_{\boldsymbol{A}}, \mathcal{W}_{\boldsymbol{\Sigma}_{\boldsymbol{A}}}\}$ in 4.3 (**MFA**-$T_a$ *formulation*). Perform static condensation procedure

-Compute $\mathbf{T}$ and $\mathbf{K}$ for weak forms $\{\mathcal{W}_\phi, \mathcal{W}_{\boldsymbol{A}}, \mathcal{W}_{\boldsymbol{\Sigma}_{\boldsymbol{A}}}\}$ in 4.3 (**MFA**-$\gamma$ *formulation*). Perform static condensation procedure

**end**

Global assembly of residuals and matrices

Get incremental $\Delta\boldsymbol{\mathcal{U}}_{e_i}^n$ (iterative solver). Update $\boldsymbol{\mathcal{U}}_{e_{i+1}}^{n_e} = \boldsymbol{\mathcal{U}}_{e_i}^{n_e} + \Delta\boldsymbol{\mathcal{U}}_{e_i}^{n_e}$

Update $\boldsymbol{\mathcal{D}}_{e_i}^{n_e}$ and $\boldsymbol{\Sigma}_{\boldsymbol{\mathcal{D}}_{e_i}}^{n_e}$: static condensation (**MFA**-$T_a$/**MFA**-$\gamma$)

**end**

/*————————*Solve Mechanical problem*————————*/

**if** $mod(n, N) = 0$ **then**

Freeze $\boldsymbol{\mathcal{U}}_e^{n_e}$ and $\{\boldsymbol{\mathcal{D}}_e^{n_e}, \boldsymbol{\Sigma}_{\boldsymbol{\mathcal{D}}_e}^{e_e}\}$ (**MFA**-$T_a$/**MFA**-$\gamma$)

$i = 1$ /*(*Newton-Raphson iteration*)*/

**while** $\|\Delta\boldsymbol{\mathcal{U}}_m\| >$ *tolerance* **do**

**forall** *elements* **do**

-Compute $\mathbf{T}$ and $\mathbf{K}$ from weak forms $(\mathcal{W}_{\boldsymbol{\mathcal{U}}_m})$ in 4.1 (*$\boldsymbol{x}$-$p$ formulation*)

-Compute $\mathbf{T}$ and $\mathbf{K}$ from weak forms $(\mathcal{W}_{\boldsymbol{\mathcal{U}}_m})$ in 4.2 (*$\boldsymbol{x}$-$p$-$\phi$ formulation*)

-Compute $\mathbf{T}$ and $\mathbf{K}$ for weak forms $(\{\mathcal{W}_{\boldsymbol{\mathcal{U}}_m}, \mathcal{W}_{\boldsymbol{\mathcal{D}}_m}, \mathcal{W}_{\boldsymbol{\Sigma}_{\boldsymbol{\mathcal{D}}_m}}\})$ in 4.3 (**MFA**-$T_a$ *formulation*). Perform static condensation procedure

-Compute $\mathbf{T}$ and $\mathbf{K}$ for weak forms $(\{\mathcal{W}_{\boldsymbol{\mathcal{U}}_m}, \mathcal{W}_{\boldsymbol{\mathcal{D}}_m}, \mathcal{W}_{\boldsymbol{\Sigma}_{\boldsymbol{\mathcal{D}}_m}}\})$ in 4.3 (**MFA**-$\gamma$ *formulation*). Perform static condensation procedure

**end**

Global assembly of residuals and matrices

Get incremental $\Delta\boldsymbol{\mathcal{U}}_{m_i}^{n_m}$ (iterative solver). Update $\boldsymbol{\mathcal{U}}_{m_i+1}^{n_m} = \boldsymbol{\mathcal{U}}_{m_i}^{n_m} + \Delta\boldsymbol{\mathcal{U}}_{m_i}^{n_m}$

Update $\boldsymbol{\mathcal{D}}_{m_i}^{n_m}$ and $\boldsymbol{\Sigma}_{\boldsymbol{\mathcal{D}}_{m_i}}^{n_m}$: static condensation (**MFA**-$T_a$/**MFA**-$\gamma$)

**end**

Update $\boldsymbol{\mathcal{U}}_m$: $t_{n+1} \to t_n$. Update $\{\boldsymbol{\mathcal{D}}_m, \boldsymbol{\Sigma}_{\boldsymbol{\mathcal{D}}_m}\}$: $t_{n+1} \to t_n$ (**MFA**-$T_a$/**MFA**-$\gamma$)

**end**

Update $\{\boldsymbol{\mathcal{U}}_e, \boldsymbol{q}\}$: $t_{n+1} \to t_n$. Update $\{\boldsymbol{\mathcal{D}}_e, \boldsymbol{\Sigma}_{\boldsymbol{\mathcal{D}}_e}\}$: $t_{n+1} \to t_n$ (**MFA**-$T_a$/**MFA**-$\gamma$)

$n+ = 1$ and $t_{n+1} = t_n + \Delta t$

**end**

**Algorithm 2:** Pseudo-code for the Staggered Solver

## 6. Numerical examples

In this Section, a comprehensive set of numerical examples is presented in order to assess the capability of the different computational strategies described in the previous Section. On the one hand, the low order $\boldsymbol{x}$-$\phi$ and $\boldsymbol{x}$-$\phi$-$p$ formulations will be compared against the more accurate super enhanced mixed **MFA**-$T_a$ and **MFA**-$\gamma$ formulations. On the other hand, staggered and staggered linearised approaches will be analysed against the more accurate monolithic approach. Through these comparisons, we aim to put forward some suggestions regarding the levels of discretisation and coupling required in the search for an approach which is sufficiently accurate yet with an affordable computational time.

### *6.1. Numerical example 1: a benchmark example for cardiac mechanics*

Through the design of this benchmark example we aim to:

- **O1.I** Compare the stabilised $\boldsymbol{x}$-$\phi$-$p$ formulation against the more accurate super enhanced mixed **MFA** formulation and in the process pave the way towards the most realistic simulation of the human myocardium. Notice that the $\boldsymbol{x}$-$\phi$ formulation has not been considered for this example due to its well-reported poor behaviour in incompressible scenarios.

- **O1.II** Select the appropriate amount of stabilisation needed in the $\boldsymbol{x}$-$\phi$-$p$ formulation in order to prevent the appearance of volumetric locking and spurious oscillations akin.

- **O1.III** Study the influence of the aspect ratio and the anisotropy contribution, in a bending dominated scenario, for the $\boldsymbol{x}$-$\phi$-$p$ formulation against the more accurate **MFA** formulation.

A cantilever beam of span $L = 10$ mm, rectangular cross section (width $b = 1$ mm and height $h$) and Dirichlet boundary conditions as shown in Figure $3_a$ is considered. The beam is subjected to a constant parabolically distributed shear force at $X = L$ (see Figure $3_a$) acting along the direction $\begin{bmatrix} 0 & 0 & -1 \end{bmatrix}$ and of maximum magnitude per unit undeformed area $q_{\max}$. The beam is considered incompressible and without electro-activation effects, and the constitutive model is characterised by the following additively decomposed strain energy functional into its isotropic-deviatoric and anisotropic contributions, defined as

$$\Psi\left(\boldsymbol{F}_{\boldsymbol{x}}, J_{\boldsymbol{x}}\right) = \frac{a}{2b} \exp\left[b\left(J_{\boldsymbol{x}}^{-\frac{2}{3}} \boldsymbol{F}_{\boldsymbol{x}} : \boldsymbol{F}_{\boldsymbol{x}} - 3\right)\right] + a_f \langle I_{4,\boldsymbol{f}_0} - 1\rangle^3, \tag{47}$$

with $\{a, b\} = \{0.496 \text{ kPa}, 7.209\}$. The material parameter $a_f$, associated with the anisotropic contribution, takes values in the range $a_f/a \in [0, 10^5]$. The direction of anisotropy is characterised by the vector $\boldsymbol{f}_0$ (see Figure $3_b$) defined as

$$\boldsymbol{f}_0 = [\cos\beta, 0, \sin\beta]; \qquad \beta\left(X, Z\right) = \frac{\pi}{3Lh} X\left(2Z - h\right). \tag{48}$$

We first select a low aspect ratio $L/h = 3.33$ and study the influence of the stabilisation parameter $\alpha$ in the response of the $\boldsymbol{x}$-$\phi$-$p$ formulation. It is well-known that for relatively low aspect ratios (where bending locking is not predominant), the possible presence of volumetric locking can be circumvented with a correct choice of $\alpha$ [58]. Based on previous experience [50], we select three different values of $\alpha = \{0.025, 0.05, 0.075\}$. We observe in Figure 5 that for a value of $q_{\max} = 14.625$ Pa, the deformed configuration and the contour plots of $p$ for the three different values of $\alpha$ are extremely similar to those provided by the accurate **MFA** formulation. The invariance of the results with respect to the three values of $\alpha$, permits us to select either of them for subsequent examples (thus $\alpha = 0.075$ henceforth).

We now turn our attention to the study of the influence of the aspect ratio and the anisotropy content. With that in mind, (a) four aspect ratios $L/h = \{3.33, 10, 20, 50\}$ are considered; (b)

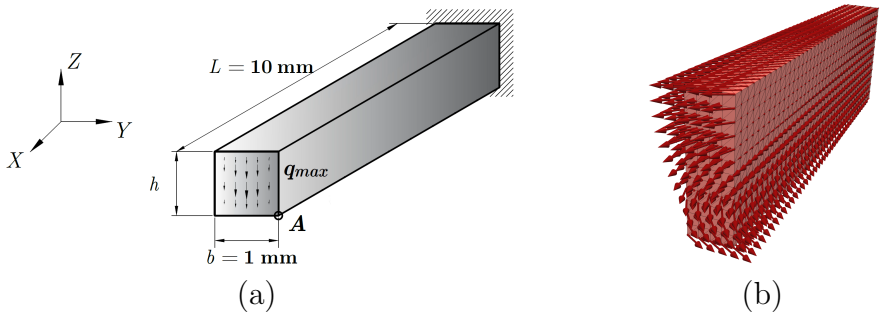


Figure 3: Numerical example 1. (a) Geometry and boundary conditions of the cantilever beam. (b) Representation of the vector $\boldsymbol{f}_0$ (see (48) for its mathematical definition) characterising the anisotropy of the beam.

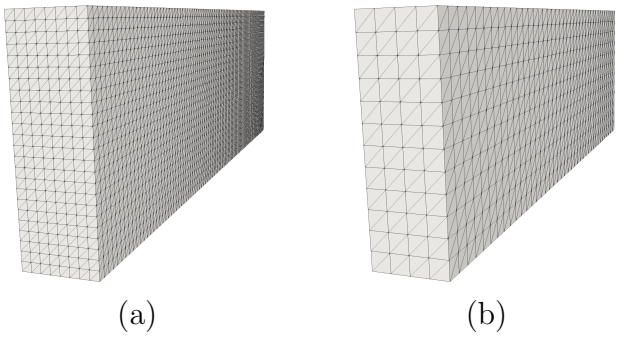


Figure 4: Numerical example 1. Structured meshes used for: (a) stabilised $\boldsymbol{x}$-$\phi$-$p$ formulation and (b) **MFA** formulation for the case $L/h = 3.33$.

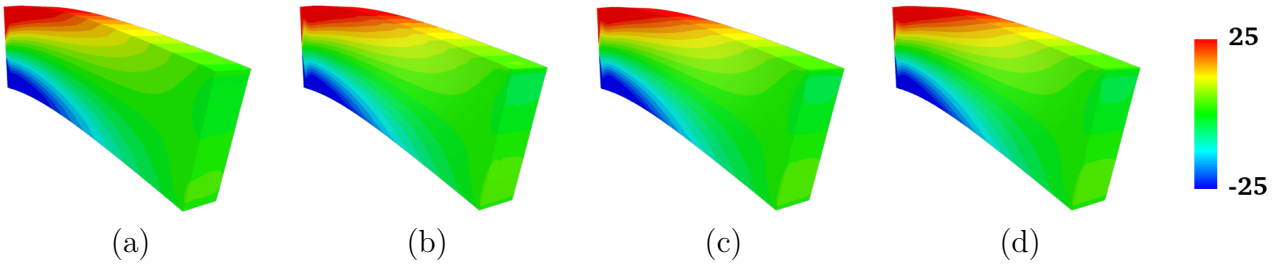


Figure 5: Numerical example 1. Contour plot distribution of the Lagrange multiplier $p$ (Pa) for: (a) **MFA** mixed formulation; (b)-(d) $\boldsymbol{x}$-$\phi$-$p$ formulation with $\alpha = 0.025$, $\alpha = 0.05$ and $\alpha = 0.075$, respectively. Aspect ratio $L/h = 3.33$ and maximum shear stress $q_{\max} = 14.625$ Pa.

different values for the anisotropy ratio $a_f/a = \{0, 10^{-2}, 10^{-1}, 10^{-0}, 10^{1}, 10^{2}, 10^{3}, 10^{4}, 10^{5}\}$ are selected; (c) the values for the maximum parabolic shear stress per unit undeformed area are $q_{\max} = \{33.75, 3.05, 0.76, 0.122\}$ Pa, corresponding to aspect ratios of $L/h = \{3.33, 10, 20, 50\}$, respectively; (d) for the **MFA**[7] formulation, four different meshes are selected depending on the aspect ratio $L/h$ (see Table 1); (e) as for the $\boldsymbol{x}$-$\phi$-$p$ formulation, for the lowest aspect ratio $L/h = 3.33$ we only consider one level of refinement. For higher aspect ratios $L/h = \{10, 20, 50\}$, two levels of refinement are selected. The coarsest refinement is defined by a structured mesh with four elements across the thickness of the beam ($\boldsymbol{x}$-$\phi$-$p$ (4)), which results in the same number of degrees of freedom $\boldsymbol{x}$ as for the equivalent discretisations used for the **MFA** formulation. On the other hand, the finest level of refinement is defined by a structured mesh with ten elements across the thickness of the beam ($\boldsymbol{x}$-$\phi$-$p$ (10)).

| **Number of degrees of freedom and element size for each cantilever beam and mixed formulation** | | | | |
|---|---|---|---|---|
| | $L/h = 3.33$ | $L/h = 10$ | $L/h = 20$ | $L/h = 50$ |
| $\boldsymbol{x}$-$\phi$-$p$ (4) | $\boldsymbol{x}$: 54675<br>$p$: 18225<br>$\Delta h$: 0.125 mm | $\boldsymbol{x}$: 3075<br>$p$: 1025<br>$\Delta h$: 0.25 mm | $\boldsymbol{x}$: 10935<br>$p$: 3645<br>$\Delta h$: 0.125 mm | $\boldsymbol{x}$: 63315<br>$p$: 21105<br>$\Delta h$: 0.05 mm |
| $\boldsymbol{x}$-$\phi$-$p$ (10) | $\boldsymbol{x}$: -<br>$p$: -<br>$\Delta h$: - | $\boldsymbol{x}$: 36663<br>$p$: 12221<br>$\Delta h$: 0.10 mm | $\boldsymbol{x}$: 139293<br>$p$: 46431<br>$\Delta h$: 0.05 mm | $\boldsymbol{x}$: 843183<br>$p$: 281061<br>$\Delta h$: 0.02 mm |
| **MFA** | $\boldsymbol{x}$: 54675<br>$p$: 11250<br>$\boldsymbol{F}$-$\boldsymbol{\Sigma_F}$: 405000<br>$\boldsymbol{H}$-$\boldsymbol{\Sigma_H}$: 405000<br>$J$-$\Sigma_J$: 11250<br>$\Delta h$: 0.25 mm | $\boldsymbol{x}$: 3075<br>$p$: 480<br>$\boldsymbol{F}$-$\boldsymbol{\Sigma_F}$: 17280<br>$\boldsymbol{H}$-$\boldsymbol{\Sigma_H}$: 17280<br>$J$-$\Sigma_J$: 480<br>$\Delta h$: 0.50 mm | $\boldsymbol{x}$: 10935<br>$p$: 1920<br>$\boldsymbol{F}$-$\boldsymbol{\Sigma_F}$: 69120<br>$\boldsymbol{H}$-$\boldsymbol{\Sigma_H}$: 69120<br>$J$-$\Sigma_J$: 1920<br>$\Delta h$: 0.25 mm | $\boldsymbol{x}$: 63315<br>$p$: 12000<br>$\boldsymbol{F}$-$\boldsymbol{\Sigma_F}$: 432000<br>$\boldsymbol{H}$-$\boldsymbol{\Sigma_H}$: 432000<br>$J$-$\Sigma_J$: 12000<br>$\Delta h$: 0.10 mm |

Table 1: Numerical example 1. Number of degrees of freedom for the different formulations employed. $\boldsymbol{x}$-$\phi$-$p$ (4) stands for 4 elements across the thickness and $\boldsymbol{x}$-$\phi$-$p$ (10) stands for 10 elements across the thickness.

From Figure 6 and Table 2, it can be observed that when no anisotropy is present, a very small relative error of 0.36% in the displacement of node $A$ in the $Z$ direction, namely $(\boldsymbol{x})_{Z,A}$, is obtained with the $\boldsymbol{x}$-$\phi$-$p$ formulation for the lowest aspect ratio. This clearly shows that the stabilisation parameter $\alpha$ has been correctly tuned. For higher aspect ratios $L/h = \{10, 20, 50\}$, the formulation exhibits bending locking and the relative error increases up to 14%. When anisotropy is present (i.e. $a_f/a \neq 0$), Figure 6 and Table 2 show that the relative error increases. This additional anisotropy-induced source of locking has been reported in [74] and resolved through a mixed formulation imposing weak convergence to the anisotropic invariant $I_{4,\boldsymbol{f}_0}$ (and $I_{4,\boldsymbol{s}_0}$ and $I_{8,\boldsymbol{f}_0,\boldsymbol{s}_0}$). However, it is important to remark that even if this source of locking is removed, there is still a 14% of bending locking present that can only be alleviated via mesh refinement. It is remarkable to observe that with the finest mesh and aspect ratio $L/h = 50$, more than $10^6$ degrees of freedom (for fields $\boldsymbol{x}$ and $p$) are needed in order to decrease the error to 6.68% for the isotropic case, whilst less than 70000 degrees of freedom (for fields $\boldsymbol{x}$ and $p$) are used in the **MFA** formulation.[8] Therefore, the accuracy of the $\boldsymbol{x}$-$\phi$-$p$ formulation is seriously compromised for aspect ratios of $L/h > 10$. All in all, we can foresee that at least 10 elements across the thickness of the myocardium must be used in order to obtain an acceptable level of accuracy

[7] Since no electro-activation effects are considered, both formulations **MFA**-$T_a$ and **MFA**-$\gamma$ coincide and hence we denote both as **MFA** in the purely mechanical case.

[8] The degrees of freedom of the discontinuous fields $\{\boldsymbol{F}, \boldsymbol{H}, J, \boldsymbol{\Sigma_F}, \boldsymbol{\Sigma_H}, \Sigma_J\}$ are not counted since they are condensed out.

for the $\boldsymbol{x}$-$\phi$-$p$ formulation. Naturally, an even finer discretisation would be needed for the $\boldsymbol{x}$-$\phi$ formulation. On the contrary, only two elements across the thickness of the myocardium would yield excellent accuracy in the case of the **MFA** formulation.

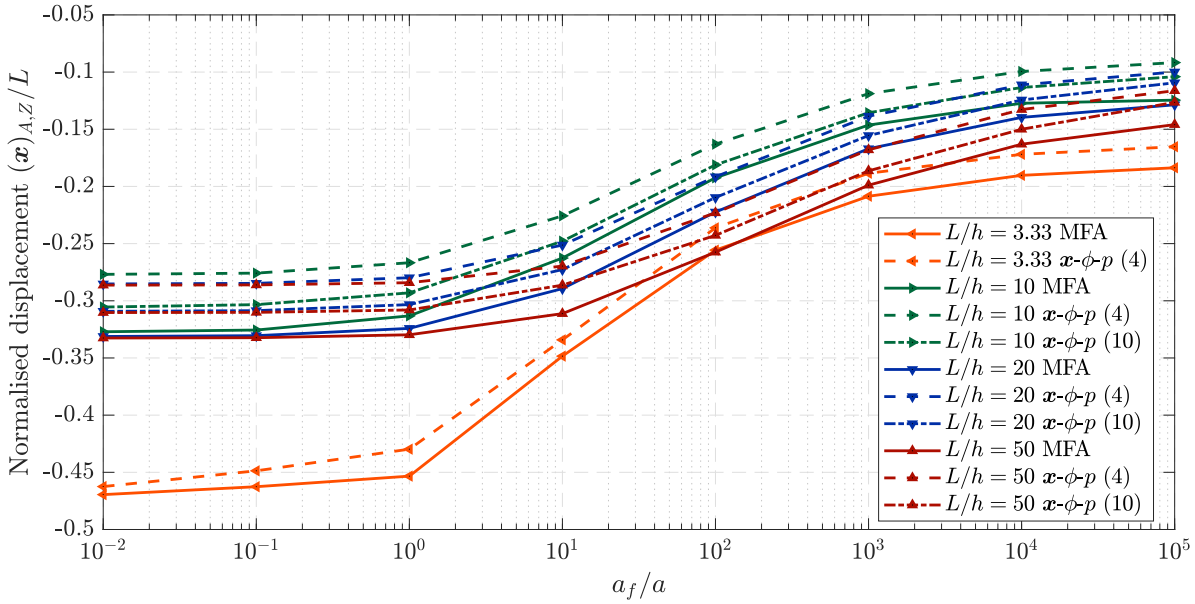


Figure 6: Numerical example 1. Value of displacement in the $Z$ direction at node $A$ (see Figure 4$_a$) for different aspect ratios ($L/h$) and anisotropy ratios ($a_f/a$). Results displayed using the **MFA** mixed formulation and the stabilised ($\alpha = 0.075$) $\boldsymbol{x}$-$\phi$-$p$ mixed formulation. (4) and (10) indicate that 4 and 10 elements in the $Z$ direction of the beam have been used, respectively.

| **Normalised deflection $(\boldsymbol{x})_{A,Z}/L$ of the cantilever beam** | | | | | | |
|---|---|---|---|---|---|---|
| | $L/h = 3.33$ $q_{\max} = 33.75$ Pa | | | $L/h = 10$ $q_{\max} = 3.05$ Pa | | |
| $a_f/a$ | **MFA** | $\boldsymbol{x}$-$\phi$-$p$ (4) | | **MFA** | $\boldsymbol{x}$-$\phi$-$p$ (4) | $\boldsymbol{x}$-$\phi$-$p$ (10) |
| 0 | -0.46955 | -0.47125 (**0.36%**) | | -0.32725 | -0.27700 (**15.36%**) | -0.30471 (**6.89%**) |
| $10^{-2}$ | -0.46950 | -0.46245 (**1.50%**) | | -0.32708 | -0.27688 (**15.35%**) | -0.30457 (**6.88%**) |
| $10^{-1}$ | -0.46258 | -0.44868 (**3.01%**) | | -0.32558 | -0.27582 (**15.28%**) | -0.30337 (**6.82%**) |
| $10^{0}$ | -0.45334 | -0.42975 (**5.20%**) | | -0.31319 | -0.26673 (**14.83%**) | -0.29306 (**6.43%**) |
| $10^{1}$ | -0.34840 | -0.33419 (**7.62%**) | | -0.26262 | -0.22574 (**14.04%**) | -0.24785 (**5.62%**) |
| $10^{2}$ | -0.25570 | -0.23622 (**4.08%**) | | -0.19244 | -0.16304 (**15.28%**) | -0.18116 (**5.86%**) |
| $10^{3}$ | -0.20859 | -0.18848 (**9.64%**) | | -0.14634 | -0.11886 (**18.78%**) | -0.13556 (**7.37%**) |
| $10^{4}$ | -0.19031 | -0.17192 (**9.66%**) | | -0.12726 | -0.09946 (**21.85%**) | -0.11347 (**10.84%**) |
| $10^{5}$ | -0.18367 | -0.16528 (**10.01%**) | | -0.12154 | -0.09169 (**24.56%**) | -0.10403 (**14.41%**) |
| | $L/h = 20$ $q_{\max} = 0.76$ Pa | | | $L/h = 50$ $q_{\max} = 0.122$ Pa | | |
| $a_f/a$ | **MFA** | $\boldsymbol{x}$-$\phi$-$p$ (4) | $\boldsymbol{x}$-$\phi$-$p$ (10) | **MFA** | $\boldsymbol{x}$-$\phi$-$p$ (4) | $\boldsymbol{x}$-$\phi$-$p$ (10) |
| 0 | -0.33129 | -0.28534 (**13.87%**) | -0.30928 (**6.64%**) | -0.33259 | -0.28633 (**13.91%**) | -0.31036 (**6.68%**) |
| $10^{-2}$ | -0.33121 | -0.28528 (**13.86%**) | -0.30921 (**6.64%**) | -0.33256 | -0.28631 (**13.91%**) | -0.31029 (**6.70%**) |
| $10^{-1}$ | -0.33051 | -0.28475 (**13.84%**) | -0.30863 (**6.62%**) | -0.33229 | -0.28611 (**13.90%**) | -0.31012 (**6.67%**) |
| $10^{0}$ | -0.32413 | -0.27985 (**13.66%**) | -0.30333 (**6.41%**) | -0.32972 | -0.28419 (**13.81%**) | -0.30802 (**6.58%**) |
| $10^{1}$ | -0.28936 | -0.25127 (**13.16%**) | -0.27270 (**5.76%**) | -0.31124 | -0.26966 (**13.36%**) | -0.28633 (**8.00%**) |
| $10^{2}$ | -0.22239 | -0.19155 (**13.87%**) | -0.20967 (**5.72%**) | -0.25748 | -0.22308 (**13.36%**) | -0.24279 (**5.70%**) |
| $10^{3}$ | -0.16702 | -0.13861 (**17.01%**) | -0.15549 (**6.90%**) | -0.19890 | -0.16800 (**15.54%**) | -0.18637 (**6.30%**) |
| $10^{4}$ | -0.13963 | -0.11116 (**20.39%**) | -0.12441 (**10.90%**) | -0.16307 | -0.13276 (**18.59%**) | -0.28633 (**14.26%**) |
| $10^{5}$ | -0.12862 | -0.09991 (**22.32%**) | -0.10938 (**14.96%**) | -0.14595 | -0.11628 (**20.33%**) | -0.12647 (**13.34%**) |

Table 2: Numerical example 1. Value of displacement in the $Z$ direction at node $A$ (see Figure 4$_a$) for different aspect ratios ($L/h$) and anisotropy ratios ($a_f/a$). Results displayed using the **MFA** mixed formulation and the stabilised ($\alpha = 0.075$) $\boldsymbol{x}$-$\phi$-$p$ formulation. The specifications (4) and (10) have been used to indicate that 4 and 10 elements in the $Z$ direction of the beam have been used, respectively. Relative error highlighted in bold font.

*6.2. Numerical example 2: simulation of the cardiac cycle with different mixed formulations*

The objective **O2.I** of this example is, taking as starting point the previous example results, to verify the conclusions obtained therein, specially regarding the comparison of the $\boldsymbol{x}$-$\phi$ and stabilised $\boldsymbol{x}$-$\phi$-$p$ formulations against the more accurate **MFA**-$T_a$ formulation for the more challenging scenario represented by the electro-activation of the myocardium within a cardiac cycle. The main features of this example are:

**Geometry:** We consider an idealised geometry of two ventricles defined by four truncated ellipsoids as previously presented in [1] (see Figure 7$_a$). The two outermost ellipsoids are centred at the origin, i.e $\{X, Y, Z\} = \{0, 0, 0\}$ mm and the lengths of their semi-axes are $\{50, 50, 70\}$ mm and $\{45, 45, 65\}$ mm. The two innermost ellipsoids are centred at $\{X, Y, Z\} = \{0, -10, 0\}$ mm and the lengths of their semi-axes are $\{40, 40, 63\}$ mm and $\{35, 35, 60\}$ mm. The four ellipsoids are truncated by the plane $Z = 0$ and only half of them are simulated as shown in Figure 7.

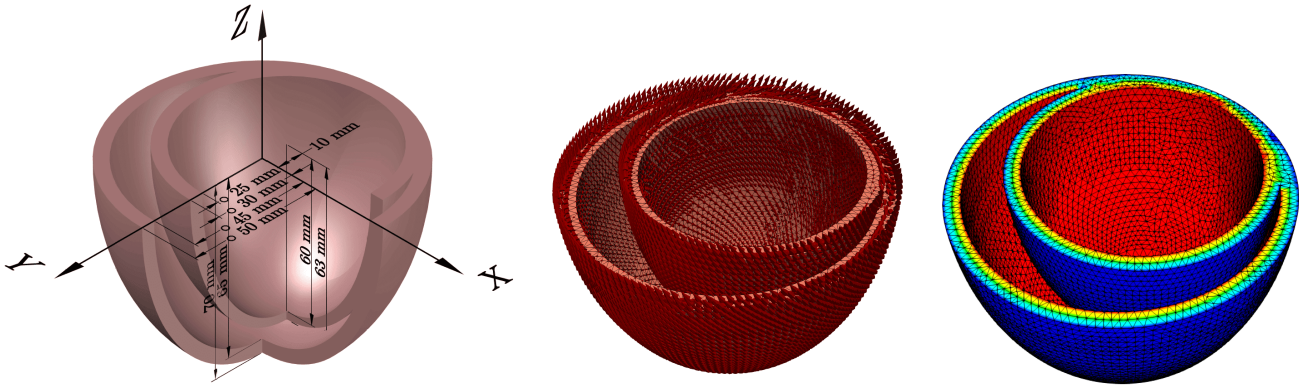


(a) (b) (c)

Figure 7: Numerical example 2. (a) Geometry of the two ventricles. (b) Representation of the fibre $\boldsymbol{f}_0$. (c) Contour plot of $\eta$ for the interpolation of $\boldsymbol{f}_0$. Blue and red regions correspond to $\eta = 1$ and $\eta = 0$, respectively.

**Fibres direction:** For the parametrisation of the fibres orientation, the family of unit fibre vectors $\boldsymbol{f}_0$ is considered first to lie on the local tangent plane of the four ellipsoidal surfaces and, second, the unit fibre vector $\boldsymbol{f}_0$ is assumed to form angle of $+60^o$ or $-60^o$ with respect to its local circumferential axis. Specifically, an orientation of $-60^o$ is considered for the first (outermost) and third ellipsoids and an orientation of $+60^o$ is used for the remaining two ellipsoids (refer to Figure 7$_b$). A regularisation of the fibre family $\boldsymbol{f}_0$ is carried out as described in [12], whereby the Poisson equation $\boldsymbol{\nabla}_0 \cdot (\boldsymbol{\nabla}_0 \eta) = 0$ is solved in the $\Omega_0$ for the intermediate variable $\eta$, with $\eta = 1$ on the ellipsoidal surfaces associated with a $+60^o$ orientation and $\eta = 0$ on the remaining ellipsoidal surfaces (refer to Figure 7$_c$). Finally, from $\eta$, the regularised fibre orientations $\{\boldsymbol{f}_0, \boldsymbol{s}_0, \boldsymbol{n}_0\}$ are obtained following the procedure described in [23].

**Discretisation**: Two different discretisations are used to compare the stabilised $\boldsymbol{x}$-$\phi$-$p$ (and $\boldsymbol{x}$-$\phi$) formulations against the super enhanced **MFA**-$T_a$ formulation. This was carefully carried out in order to maintain a comparable number of solver unknowns across the different formulations. Thus, the **MFA**-$T_a$ mesh (see Figure 8 (left)) resulted in $\{525705, 175235, 112088\}$ degrees of freedom for the $\boldsymbol{x}$, $\phi$ and $p$ fields, respectively[9]. The stabilised $\boldsymbol{x}$-$\phi$-$p$ (and $\boldsymbol{x}$-$\phi$) mesh (see Figure 8 (right)) resulted in $\{578745, 192915, 192915\}$ degrees of freedom for the same fields.

[9]The degrees of freedom for the discontinuous fields $\{\boldsymbol{F}, \boldsymbol{H}, J, \boldsymbol{A}\}$ are $\{4035168, 4035168, 112088, 1345056\}$ (the same for their work conjugates $\{\boldsymbol{\Sigma}_{\boldsymbol{F}}, \boldsymbol{\Sigma}_{\boldsymbol{H}}, \Sigma_J, \boldsymbol{\Sigma}_{\boldsymbol{A}}\}$). Notice that these degrees of freedom are condensed out by means of a standard static condensation procedure [1])

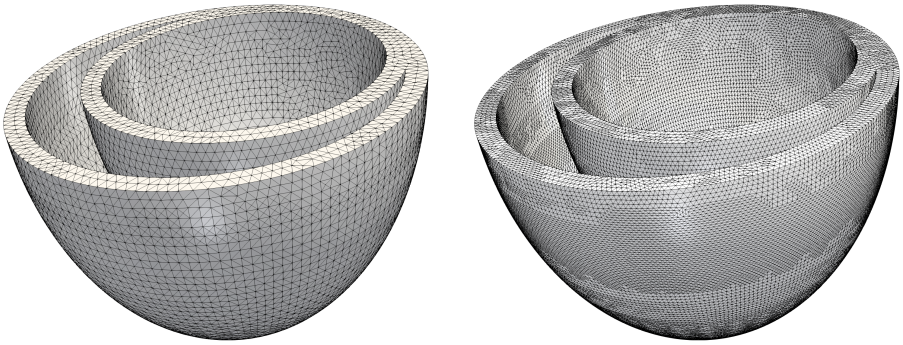

Figure 8: Numerical example 2. Unstructured meshes considered in the heartbeat simulation: discretisation used for the **MFA**-$T_a$ formulation (left) and for the stabilised $\boldsymbol{x}$-$\phi$-$p$ and $\boldsymbol{x}$-$\phi$ formulations (right).

**Boundary conditions:** Dirichlet boundary conditions are applied on the red (displacements constrained in the $OZ$ direction) and white (displacements constrained in all directions) coloured regions in Figure $9_a$. For the remaining boundaries, homogeneous Neumann boundary conditions are considered. For the cardiac action potential field, homogeneous Neumann boundary conditions are considered everywhere (see equation $3_b$). The mesh displayed in Figure $9_a$ corresponds to the discretisation used for the **MFA**-$T_a$ formulation. For the mesh used for the $\boldsymbol{x}$-$\phi$-$p$ (and $\boldsymbol{x}$-$\phi$) formulation, a very similar region to the white area in Figure $9_a$ was carefully selected for the application of the corresponding Dirichlet boundary conditions.

**Initial conditions:** Initial conditions for the cardiac action potential are triggered through an arbitrary stimulation intensity function $I_{\text{stim}}$ applied on the red coloured region in Figure $9_b$. As above, the mesh displayed in Figure $9_b$ corresponds to the discretisation used for the **MFA**-$T_a$ formulation. Similarly, for the mesh used for the $\boldsymbol{x}$-$\phi$-$p$ (and $\boldsymbol{x}$-$\phi$) formulation, a very similar region to the red area in Figure $9_b$ was carefully selected for the application of the initial (electrical) conditions.

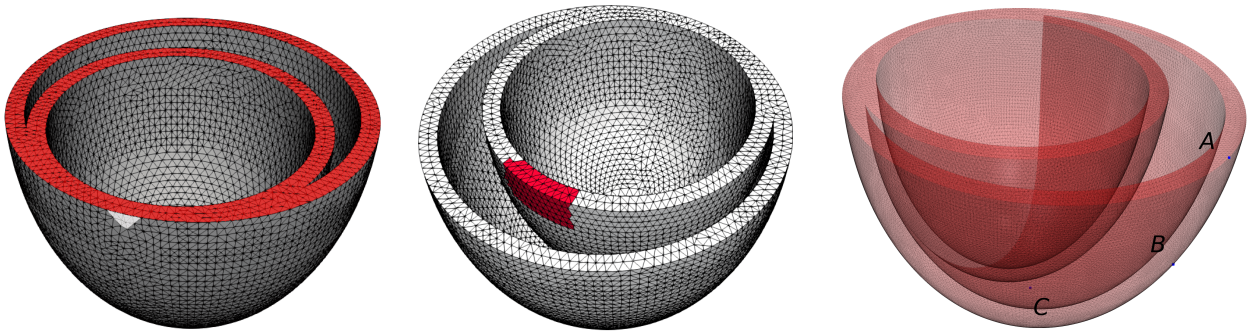


(a) (b) (c)

Figure 9: Numerical example 2. **(a)** Regions for the application of Dirichlet boundary conditions for displacement field. In red: restricted displacements in $OZ$ direction; in white: restricted displacements in all directions. **(b)** Region (in red) where the initial electrical stimulation occurs. **(c)** Nodes where the electrical dispersion is measured.

**Time integration**: An adaptive time-stepping strategy is used for the time integration of the cardiac action potential equation (3). An initial small time step $\Delta t$ is required in order to correctly capture the rapid initial depolarisation taking place which can then be gradually increased without compromising the overall accuracy of the simulation. The time step $\Delta t$ used at a given time $t$ is automatically chosen by measuring the rate of change in absolute value of the internal variables in the ionic model. The minimum and maximum values for $\Delta t$ are 0.3 ms and 50 ms, respectively. The backward Euler scheme is used for the time integration of: (a) the

cardiac action potential equation (3); (b) the evolution equation for the field activation $T_a$ (19); (c) the ordinary differential equations for the vector of internal variables $\boldsymbol{q}$ (see (16)).

**Material parameters**: Table 3 contains the values adopted for the relevant material parameters for: (a) Holzapfel-Ogden model [10] in (5); (b) ionic model proposed by Bueno-Orovio *et al.* [34]; (c) *active stress* approach with activation model as proposed by Nash and Panfilov [41]; (d) parameters controlling diffusion in (35). In addition, a value of $\kappa = 10$ kPa has been used in the $\boldsymbol{x}$-$\phi$ formulation in order to enforce near incompressibility.

**Numerical strategy**: A monolithic approach is used (see Section 5.2.1 and Algorithm 1).

| **Parameters for the Holzapfel-Ogden constitutive law** | | | | | | |
|---|---|---|---|---|---|---|
| $a = 0.496$ kPa | $a_f = 15.196$ kPa | $a_s = 3.283$ kPa | $a_{fs} = 0.662$ kPa | | | |
| $b = 7.209$ | $b_f = 20.417$ | $b_s = 11.176$ | $b_{fs} = 9.466$ | | | |
| **Parameters for the Bueno-Orovio ionic model** | | | | | | |
| $u_o = 0.0$ | $\theta_v = 0.3$ | $\tau_{o1} = 400$ | $\tau_{v1}^- = 60$ | $w_\infty^* = 0.94$ | $\tau_{s1} = 2.7342$ | $k_w^- = 65$ |
| $u_u = 1.55$ | $\theta_w = 0.13$ | $\tau_{o2} = 6$ | $\tau_{v2}^- = 1150$ | $\tau_{w1}^- = 60$ | $\tau_{s2} = 16$ | $k_s = 2.0994$ |
| $u_s = 0.9087$ | $\theta_o = 0.006$ | $\tau_{so1} = 30.0181$ | $\tau_w^+ = 200$ | $\tau_{w2}^- = 15$ | $\tau_{si} = 1.8875$ | $k_{so} = 2.0458$ |
| $u_w^- = 0.03$ | $\theta_v^- = 0.006$ | $\tau_{so2} = 0.9957$ | $\tau_v^+ = 1.4506$ | $\tau_{fi} = 0.11$ | $\tau_w^\infty = 0.07$ | $I_{\text{stim}} = 0.9$ |
| **Parameters for the activation model proposed by Nash and Panfilov** | | | | | | |
| $k_{T_a} = 12.5$ kPa/$\mu$M | | | | | | |
| **Additional parameters** | | | | | | |
| $d_{\text{iso}} = 8 \cdot 10^{-4}$ m$^2$/s | | | $d_{\text{ani}} = 12 \cdot 10^{-4}$ m$^2$/s | | | |

Table 3: List of material parameters used in numerical example 2 for the active stress approach.

Figure 10 shows at points $A$, $B$ and $C$ (see Figure 9$_c$), the time evolution of the $X$, $Y$ and $Z$ components of the displacement, respectively, and of the transmembrane potential $\phi$. The evolution of the transmembrane potential is almost identical for the three formulations. However, as anticipated (refer to the previous example), the mechanical response (displacements) is severely affected by the choice of formulation. Clearly, the displacements predicted by the $\boldsymbol{x}$-$\phi$-$p$ formulation are closer to those predicted by the **MFA** formulation, in comparison with those obtained by the $\boldsymbol{x}$-$\phi$ formulation. These results are illustrated in more detail in Figures 11, 12 and 13. Figure 11 shows how the wave front for the transmembrane potential $\phi$ is practically coincident regardless of the employed methodology. However, Figures 12 and 13 highlight distinct discrepancies in the mechanical response (displacements) between the three formulations. We introduce the quantity of interest $\varepsilon_{\boldsymbol{x}}$, quantifying the error of the $\boldsymbol{x}$-$\phi$-$p$ (and $\boldsymbol{x}$-$\phi$) formulation with respect to the **MFA** formulation, defined as

$$\epsilon_x = \frac{||\boldsymbol{x} - \boldsymbol{x}_{\mathbf{MFA}}||}{\max(||\boldsymbol{x}||)}, \tag{49}$$

where $\boldsymbol{x}_{\mathbf{MFA}}$ denotes the deformed position obtained with the **MFA** formulation at a given Gauss point of the computational domain. In particular, a value of $\varepsilon_{\boldsymbol{x}}$ of 25% is observed in the $\boldsymbol{x}$-$\phi$-$p$ formulation whereas a larger error of up to 50% is observed when using the $\boldsymbol{x}$-$\phi$ formulation. Therefore, the results obtained confirm that extremely fine discretisations are potentially required when employing the $\boldsymbol{x}$-$\phi$-$p$ and $\boldsymbol{x}$-$\phi$ approaches. On the contrary, coarser meshes are acceptable when employing the **MFA** formulation, yielding very accurate results.

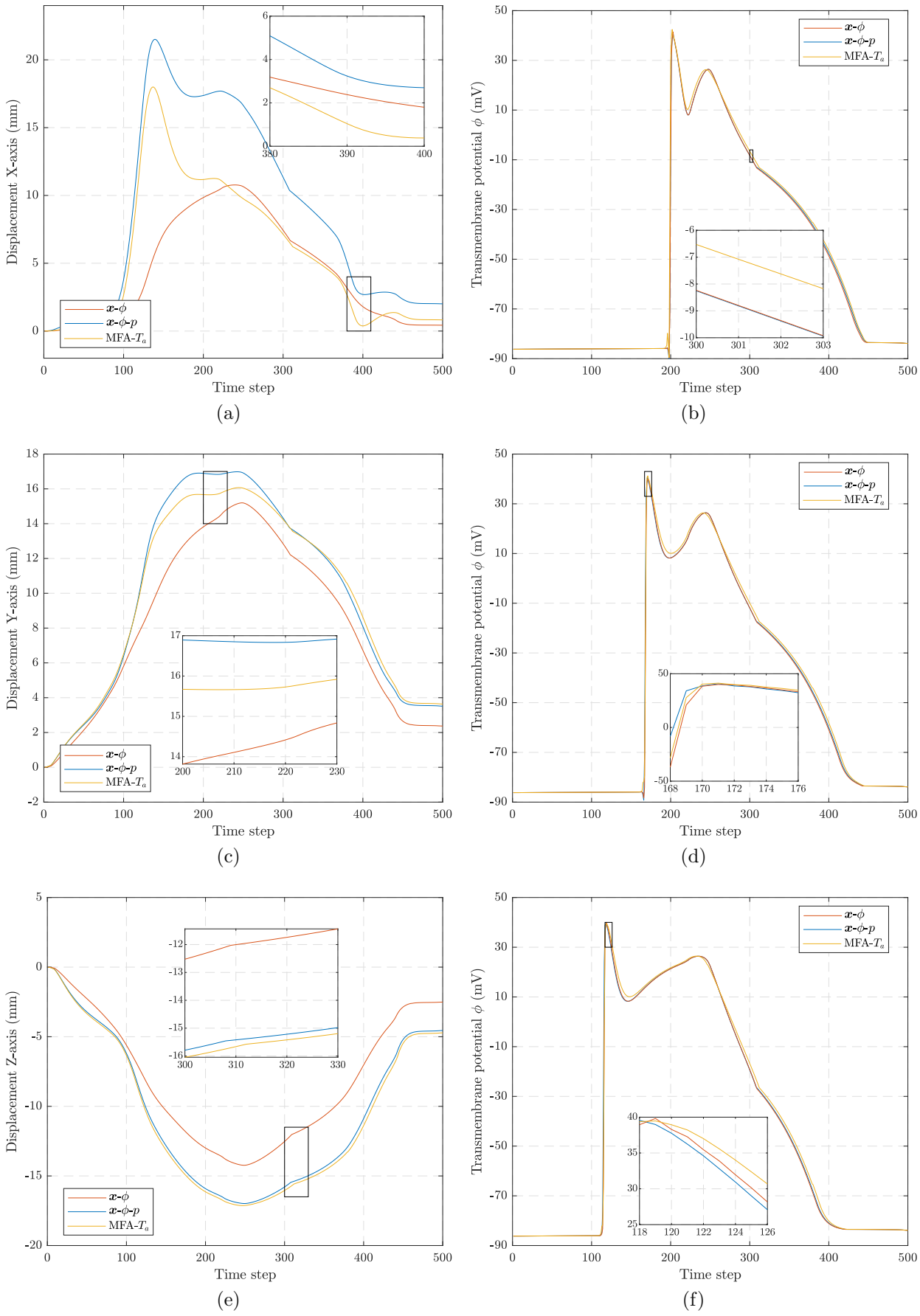


Figure 10: Numerical example 2. (a)-(b) Time evolution of the displacement in $X$ direction and transmembrane potential $\phi$ at node $A$. (c)-(d) Time evolution of the displacement in $Y$ direction and transmembrane potential $\phi$ at node $B$. (e)-(f) Time evolution of the displacement in $Z$ direction and transmembrane potential $\phi$ at node $C$. Results obtained with the **MFA**-$T_a$, $\boldsymbol{x}$-$\phi$-$p$ and $\boldsymbol{x}$-$\phi$ formulations (*activation type*: active stress).

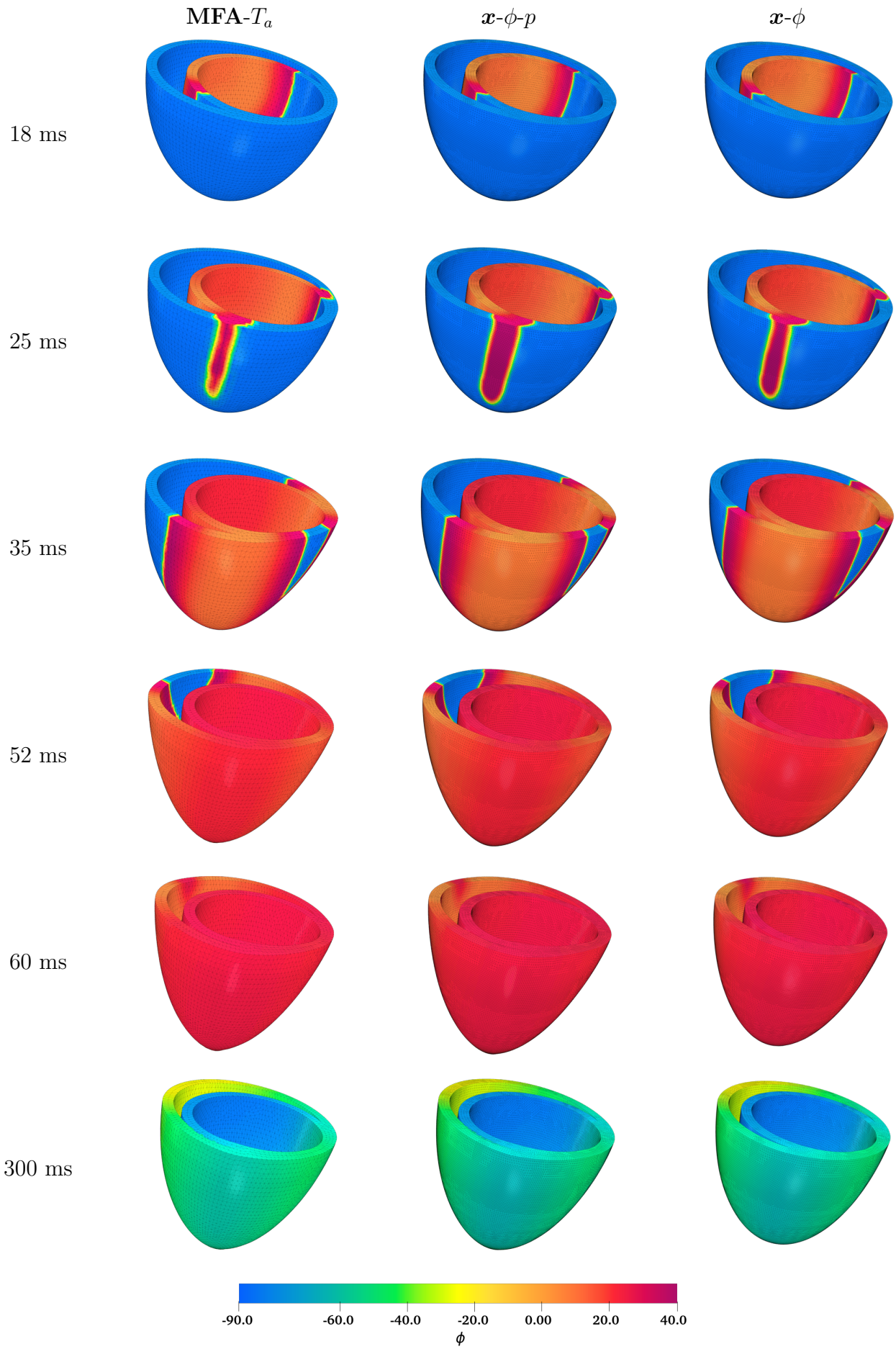


Figure 11: Numerical example 2. Evolution of the cardiac action potential wave front. Results obtained with **MFA**-$T_a$ formulation (left), $\boldsymbol{x}$-$\phi$-$p$ formulation (centre) and $\boldsymbol{x}$-$\phi$ formulation (right). Snapshots for times $t = \{18, 25, 35, 52, 60, 300\}$ (ms) of the cardiac cycle (*activation type*: active stress).

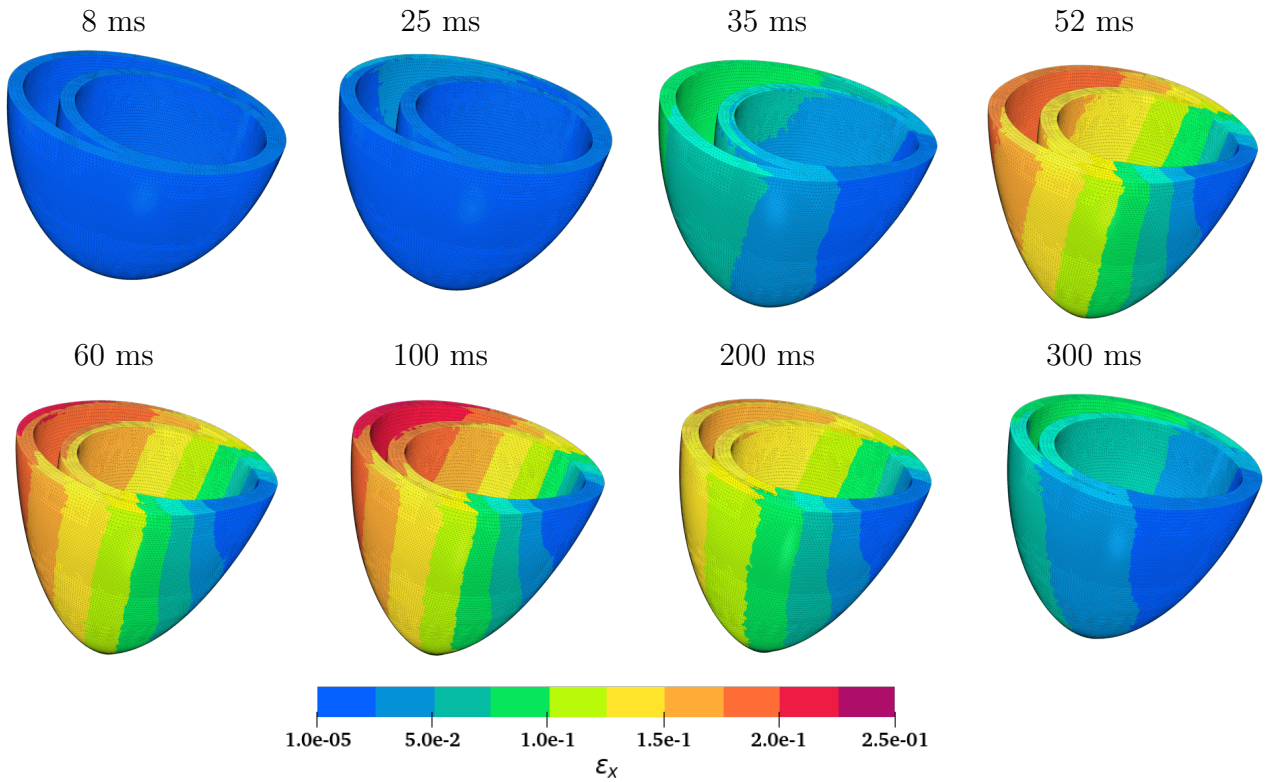


Figure 12: Numerical example 2. Contour plot of $\varepsilon_{\boldsymbol{x}}$ in (49). Error of $\boldsymbol{x}$-$\phi$-$p$ formulation with respect to the **MFA**-$T_a$ formulation. Snapshots for various times $t = \{8, 25, 35, 52, 60, 100, 200, 300\}$ (ms) of the cardiac cycle (*activation type*: active stress).

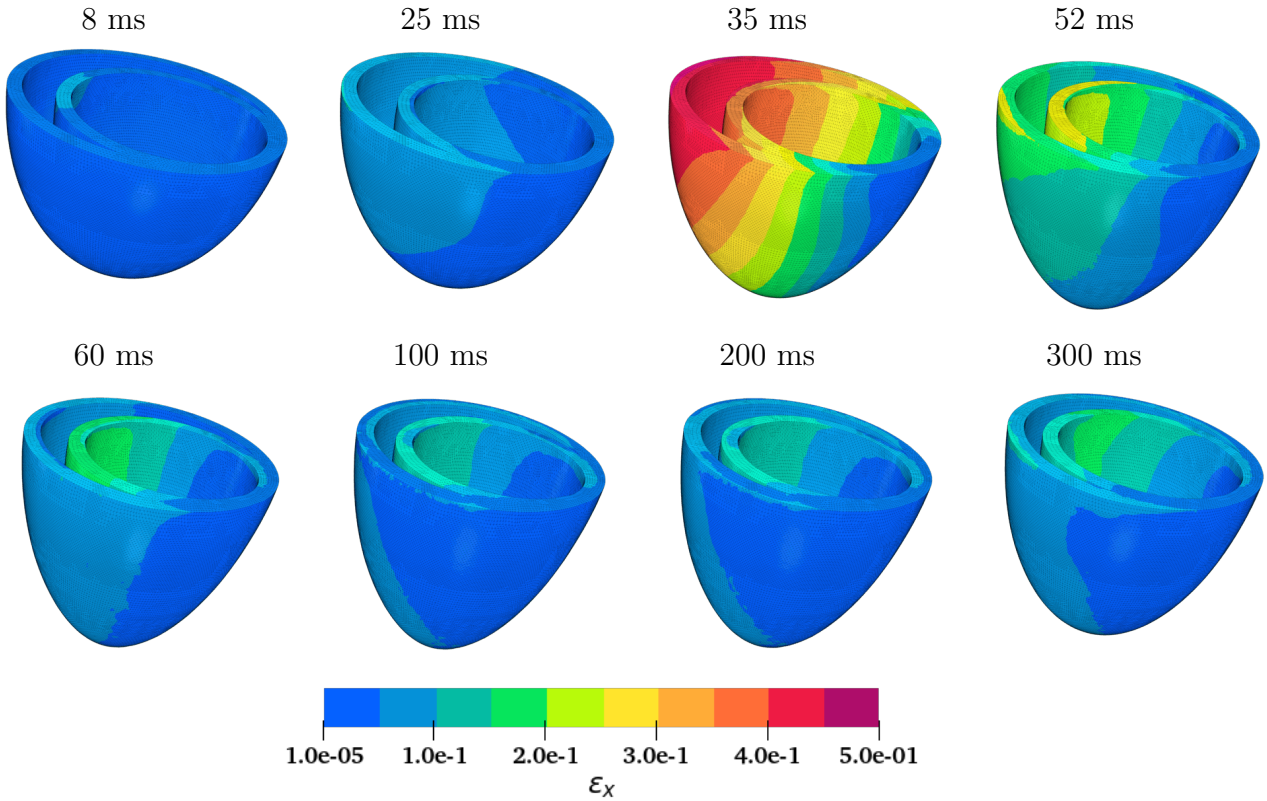


Figure 13: Numerical example 2. Contour plot of $\varepsilon_{\boldsymbol{x}}$ in (49). Error of $\boldsymbol{x}$-$\phi$ formulation with respect to the **MFA**-$T_a$ formulation. Snapshots for various times $t = \{8, 25, 35, 52, 60, 100, 200, 300\}$ (ms) of the cardiac cycle (*activation type*: active stress).

*6.3. Numerical example 3: Monolithic vs. Staggered and Staggered Linearised approaches.*

In this example, we consider the same setting as that described in the previous example in terms of geometry, fibres direction, boundary and initial conditions and time integration scheme. The initial focus is on the super enhanced **MFA** formulation. Both *active strain* and *active stress* approaches will be explored in the context of two different coupling strategies: monolithic and staggered. Specifically, the objectives of this example are:

- **O3.I** To assess numerically the accuracy and feasibility of the staggered solver presented in Section 5.2.2 with respect to the monolithic solver presented in Section 5.2.1 for: (a) **MFA**-$T_a$ active stress and (b) **MFA**-$\gamma$ active strain approaches.
- **O3.II** To determine the accuracy of the staggered scheme when the ratio $N$ between the mechanical time step $\Delta t_m$ and the electrical time step $\Delta t$ increases.

For the **MFA**-$T_a$ active stress approach, Figure 14 shows at points $A$, $B$ and $C$ (see Figure $9_c$), the time evolution of the $X$, $Y$ and $Z$ components of the displacement, respectively, and of the transmembrane potential $\phi$ obtained with the monolithic solver and the staggered solver for different values of the ratio $N = \{1, 2, 4, 6, 8, 10\}$. Remarkably, the time evolution of $\phi$ is almost identical irrespective of the solver. In addition, the evolution of the displacements are also extremely similar. Notice from the zoomed detailed regions in Figure 14 that for the staggered schemes, the displacements remain constant throughout the time span $\Delta t_m = N\Delta t$, during which the *Mechanical Problem* is frozen. These results are further supported in Figures 15 and 16, where it can be seen that the wave front for the transmembrane potential $\phi$ is practically coincident for both monolithic and staggered solvers (the latter with $N = 10$). Similarly as above, we introduce an error indicator for the mechanical response quantified by a parameter $\varepsilon_{\boldsymbol{x}}$ defined as

$$\epsilon_x = \frac{||\boldsymbol{x} - \boldsymbol{x}_{\text{mono}}||}{\max(||\boldsymbol{x}||)}, \tag{50}$$

where $\boldsymbol{x}_{\text{mono}}$ denotes the deformed position obtained with the Monolithic Solver. As can be seen by the values of this indicator, this error is extremely low irrespective of the value of $N$ adopted. These results permit to conclude that for the *active stress* approach, the staggered solver yields extremely similar results to those obtained with the monolithic solver. This conclusion has been confirmed for a range of values of $N$ up to 10, making this approach extremely advantageous from the computational standpoint.

For the **MFA**-$\gamma$ with *active strain* approach, a similar study is conducted, and results are displayed in Figures 17, 18 and 19. It is very interesting to remark that the staggered solver becomes now unstable for a value of $N$ larger than 7, which is the reason why these results are not displayed. For $N \leq 7$, the staggered solver converges and we can see how, similarly to the *active stress* approach, the time evolution of the transmembrane potential is almost identical irrespective of the solver used. However, some differences can be observed when comparing the displacements predicted by the monolithic and the staggered solvers during the plateau phase, which corresponds to the time of maximum contraction, around 270 ms. This can be attributed to: first, the multiplicative decomposition of the deformation gradient tensor which results in a higher level of nonlinearity of the constitutive law, as opposed to the additive decomposition used in the *active stress* approach and, second, the dependence with respect to the anisotropic invariant $I_{4,\boldsymbol{f}_0}$ in the activation law (see equation (21)).

The error in the mechanical response, quantified by the parameter $\varepsilon_{\boldsymbol{x}}$ defined in (50) can reach up to 10%, as opposed to the 1% obtained when considering the *active stress* approach (refer to Figure 16). It is also worth stressing that the higher degree of nonlinearity introduced by the multiplicative decomposition of the deformation gradient tensor leads to an increase in the number of iterations required for the convergence of the Newton-Raphson for the *Mechanical*

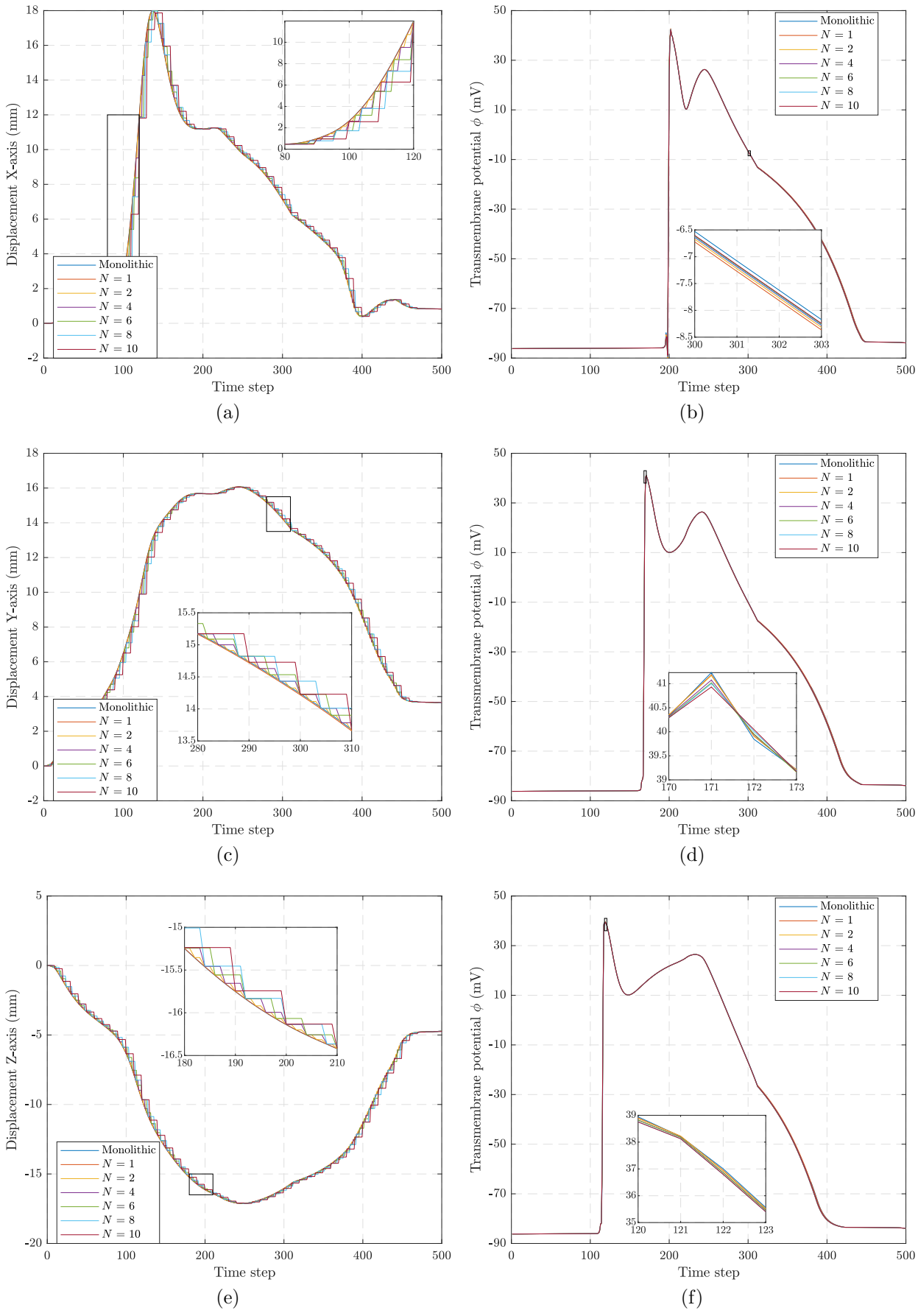


Figure 14: Numerical example 3. Comparison of monolithic and staggered solvers with the **MFA**-$T_a$ formulation: (a)-(b) Time evolution of the displacement in $X$ direction and transmembrane potential $\phi$ at node $A$. (c)-(d) Time evolution of the displacement in $Y$ direction and transmembrane potential $\phi$ at node $B$. (e)-(f) Time evolution of the displacement in $Z$ direction and transmembrane potential $\phi$ at node $C$. Results obtained (*activation type*: active stress).

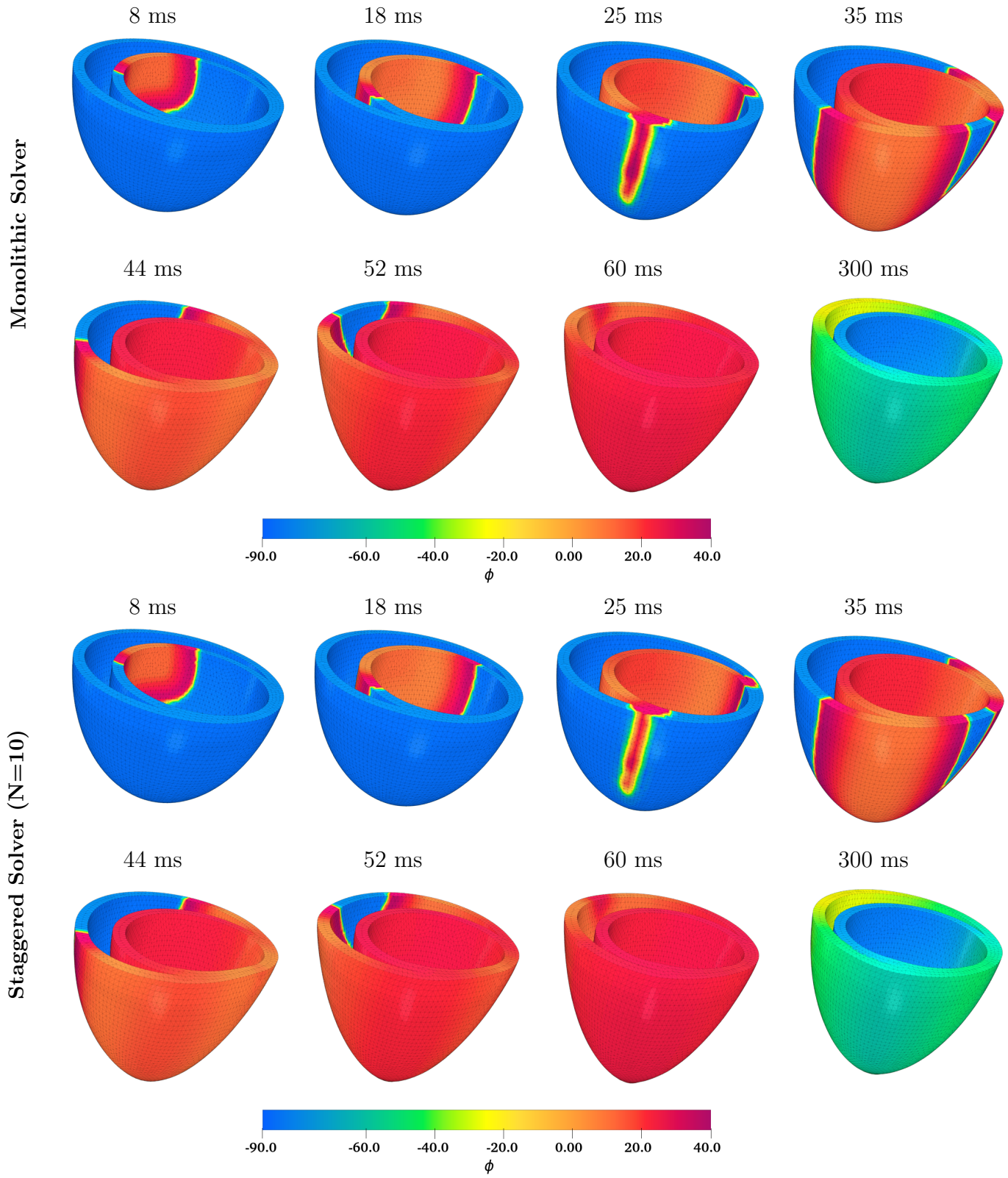


Figure 15: Numerical example 3. Evolution of the cardiac action potential wave-front. Snapshots for various times $t = \{8, 18, 25, 35, 44, 52, 60, 300\}$ (ms) of the cardiac cycle. Results obtained with **MFA**-$T_a$ formulation using the monolithic solver (up) and the staggered solver (down), *activation type*: active stress).

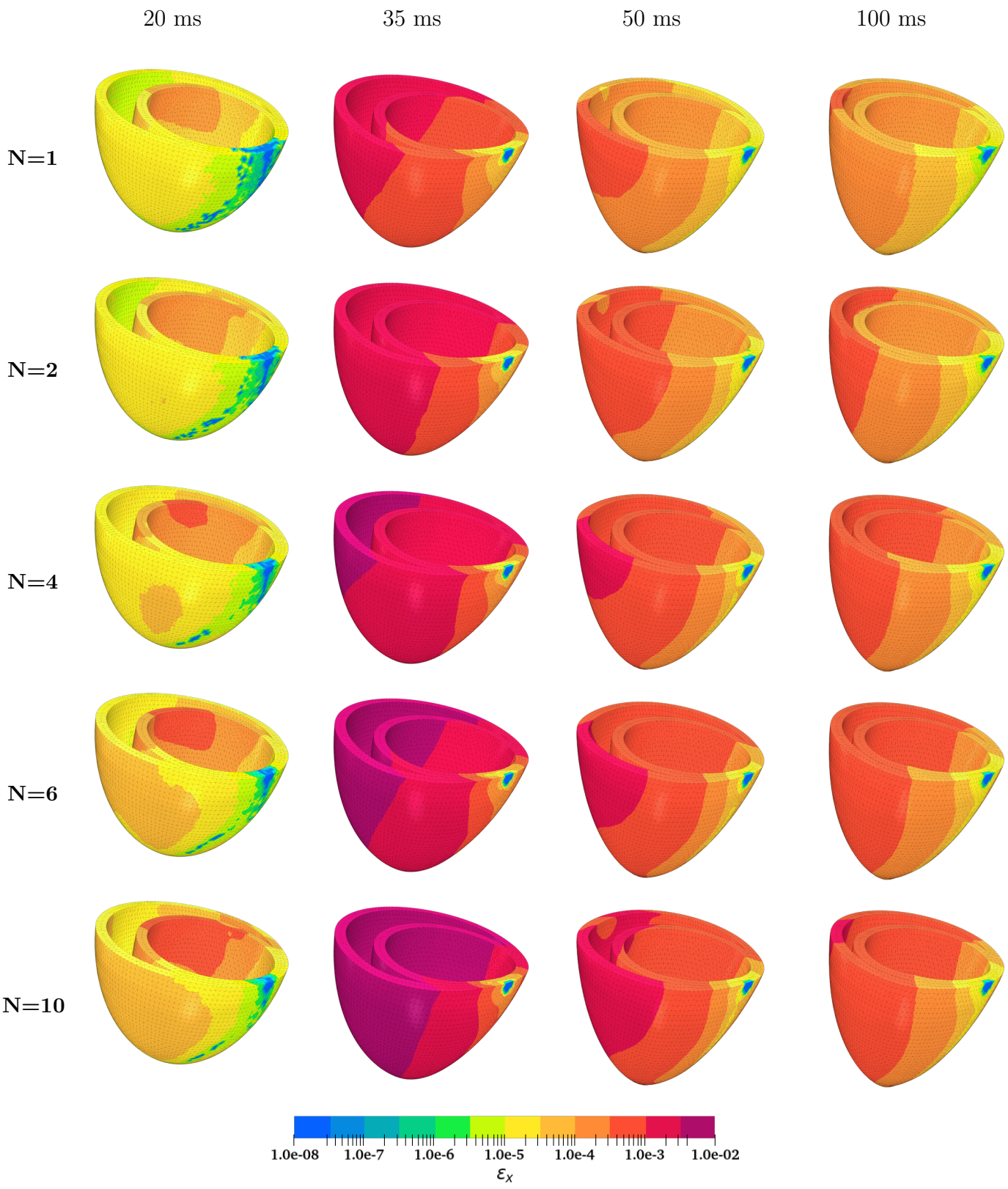


Figure 16: Numerical example 3. Contour plot of $\varepsilon_{\boldsymbol{x}}$ in (49) for snapshots associated with various times $t = \{20, 35, 50, 100\}$ (ms) of the cardiac cycle. Results obtained with **MFA**-$T_a$ formulation and staggered solver for different values of the ratio between the mechanical and electrical time steps $N = \{1, 2, 4, 6, 10\}$, (*activation type*: active stress).

*Problem*. Naturally, this leads to an obvious reduction in the overall computational efficiency of the staggered approach, which was critically observed for values of $N$ beyond $N = 4$. Therefore, we can conclude that: (a) the maximum value of $N$ before stability is compromised in the staggered solver is smaller when considering the *active strain* approach instead of *active stress*; (b) in the *active strain* approach, the staggered solver yields extremely similar results to those obtained with the monolithic solver with regards to the time evolution of $\phi$, in agreement with the results obtained when considering the *active stress* approach; (c) in the *active strain* approach, staggered and monolithic solvers evidence higher discrepancies in the time evolution of the displacements than in the case of *active stress*; (d) the fastest staggered solver for *active strain* corresponds to $N = 4$. Beyond this value, the higher number of iterations required in the Newton-Raphson algorithm for the mechanical problem entails a reduction of the efficiency of the algorithm.

We now turn our attention to the comparison of the monolithic and staggered algorithms but particularised to the case of the stabilised $\boldsymbol{x}$-$\phi$-$p$ formulation (just for *active stress*, to simplify the following exposition). As such, we use the same setting as above and the objectives remain the same, namely, **O3.I** and **O3.II**. The mesh used is identical to that in Figure $9_b$. Relevant results are presented in Figures 20, 21 and 22. Once again, the time evolution of $\phi$ is virtually identical irrespective of the solver. In addition, the time evolution of the displacements is also very similar when comparing the different coupling strategies, although not as much as when we considered the **MFA**-$T_a$ formulation (see Figure 14). These results permit us to conclude that: (a) staggered and monolithic approaches yield very similar results regarding the time evolution of the transmembrane potential; (b) some differences, albeit minor, can be observed in terms of the displacement field; (c) the difference in results between staggered and monolithic solvers is smaller for the case of the **MFA** formulation than for the $\boldsymbol{x}$-$\phi$-$p$ formulation; (d) a value of $N = 10$ would result in an extremely advantageous computational approach.

We finally explore the potential for considering the staggered linearised approach presented in Section 5.2.3, in the search of an extremely optimum computational approach. As such, our objective **O.3.III** is to determine the accuracy of the staggered linearised approach, comparing it against the staggered solver for different ratios $N$ between the mechanical and electrical time steps. The main results are summarised in Figures 23 and 24. Figure 23 displays the results obtained with the staggered solver with $N = 1$ and the staggered linearised solver for different values of the ratio $N = \{1, 4, 10\}$. It is interesting to observe that the time evolution of $\phi$ is almost identical irrespective of the solver. However, we observe a discrepancy for the displacements which is more pronounced as the ratio $N$ in the staggered linearised solver is increased. Notice how the error in the mechanical response, quantified by the parameter $\varepsilon_{\boldsymbol{x}}$ can reach a value of around 5% for $N = 1$, and inadmissible values of up to 60% as $N$ is increased up to $N = 10$. It is clear that the linearised expression adopted for the evaluation of the first Piola-Kirchhoff stress tensor is the key reason for the differences observed. This could potentially be alleviated either by exploring a more accurate linearised expression of the stress tensor or by reducing the size of the time step $\Delta t$. All in all, these results permit us to conclude that: (a) the time evolution of the transmembrane potential $\phi$ remains almost identical for both staggered and staggered linearised solvers, irrespectively of the value of $N$; (b) for $N = 1$, there is good agreement in terms of displacements between the staggered and the staggered linearised approaches; (c) for increasing values of $N$, the staggered linearised approach can yield very inaccurate results in terms of displacements if a non-careful linearised approximation of the stress tensor is employed.

All the large scale examples presented in this paper were coded in FORTRAN and executed in a desktop computer with a ten-core Intel Xeon E5-2630v4 2.20 GHz processor and 64 GB of RAM memory. For the solution stage, the parallel LU decomposition solver provided by the library PARDISO [75] was selected for the monolithic solver and the *Mechanical Problem* in the staggered solvers. Alternatively, the well-conditioned stiffness matrix in the *Electrical Problem* admits iterative solvers, for which the GMRES method from the package MI24 [76] was considered.

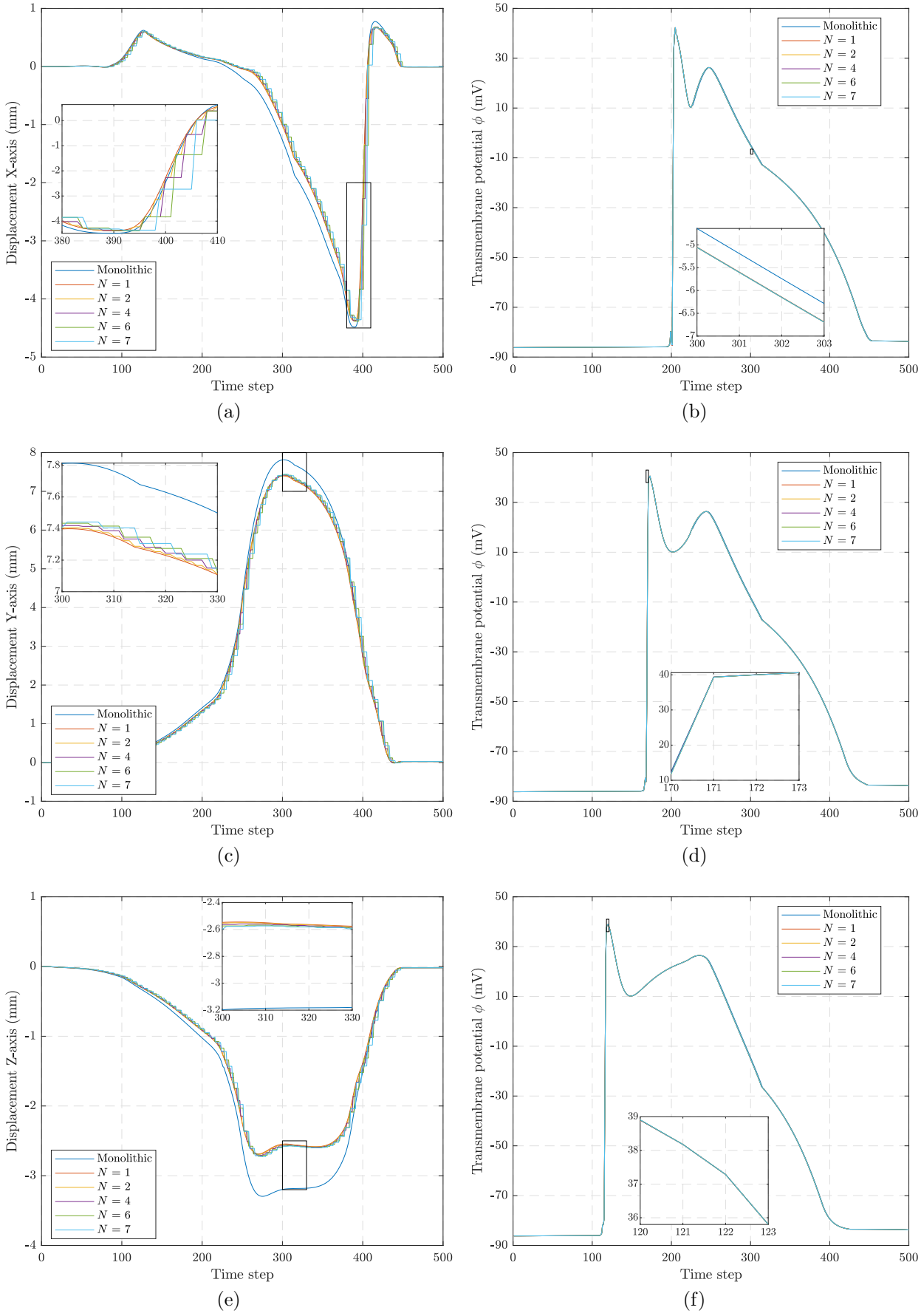


Figure 17: Numerical example 3. Comparison of monolithic and staggered solvers with the **MFA**-$\gamma$ formulation: (a)-(b) Time evolution of the displacement in $X$ direction and transmembrane potential $\phi$ at node $A$. (c)-(d) Time evolution of the displacement in $Y$ direction and transmembrane potential $\phi$ at node $B$. (e)-(f) Time evolution of the displacement in $Z$ direction and transmembrane potential $\phi$ at node $C$. Results obtained (*activation type*: active strain).

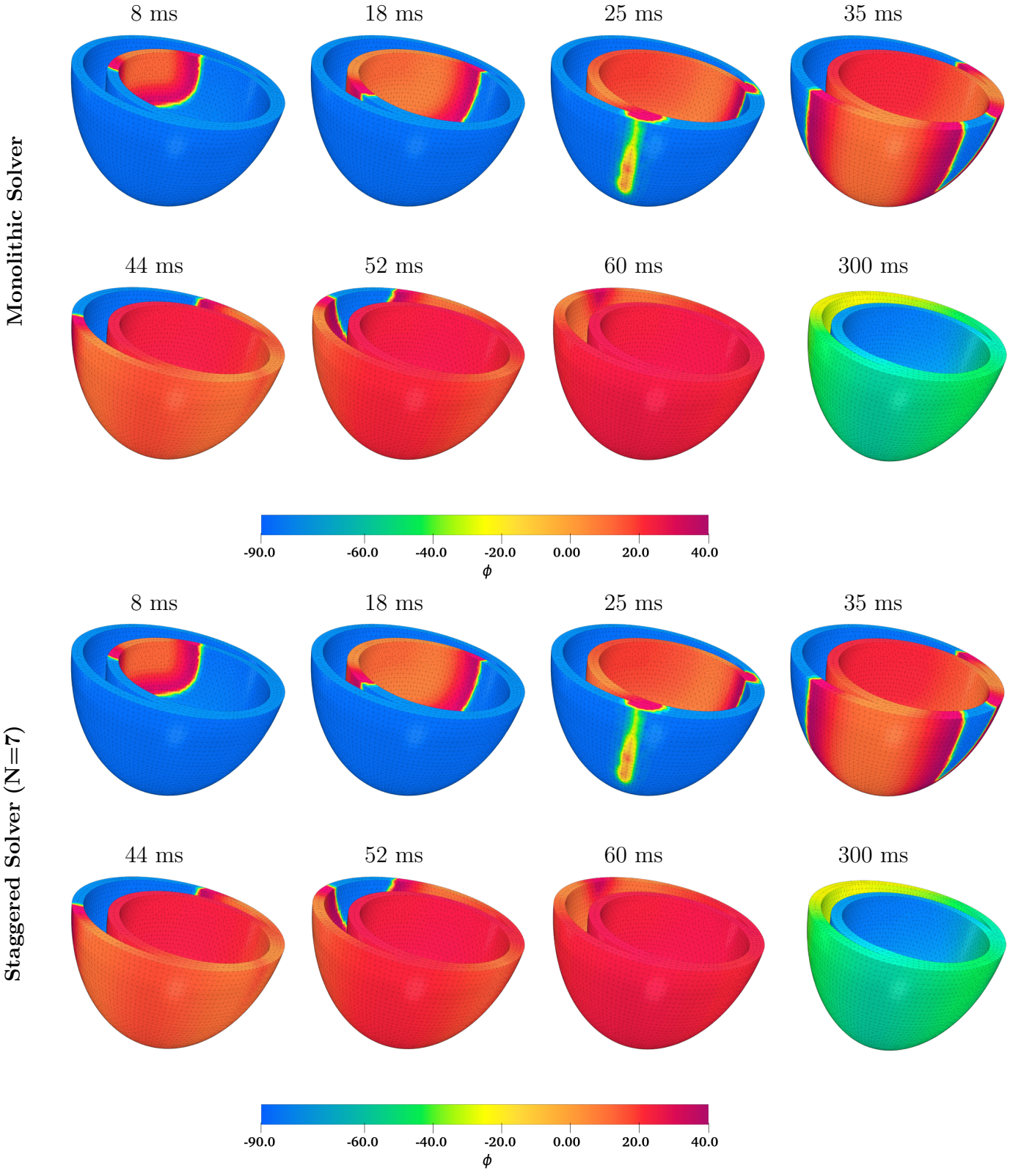


Figure 18: Numerical example 3. Evolution of the cardiac action potential wave-front. Snapshots for various times $t = \{8, 18, 25, 35, 44, 52, 60, 300\}$ (ms) of the cardiac cycle. Results obtained with **MFA**-$\gamma$ formulation using the monolithic solver (up) and the staggered solver with $N = 7$ (down), *activation type*: active strain).

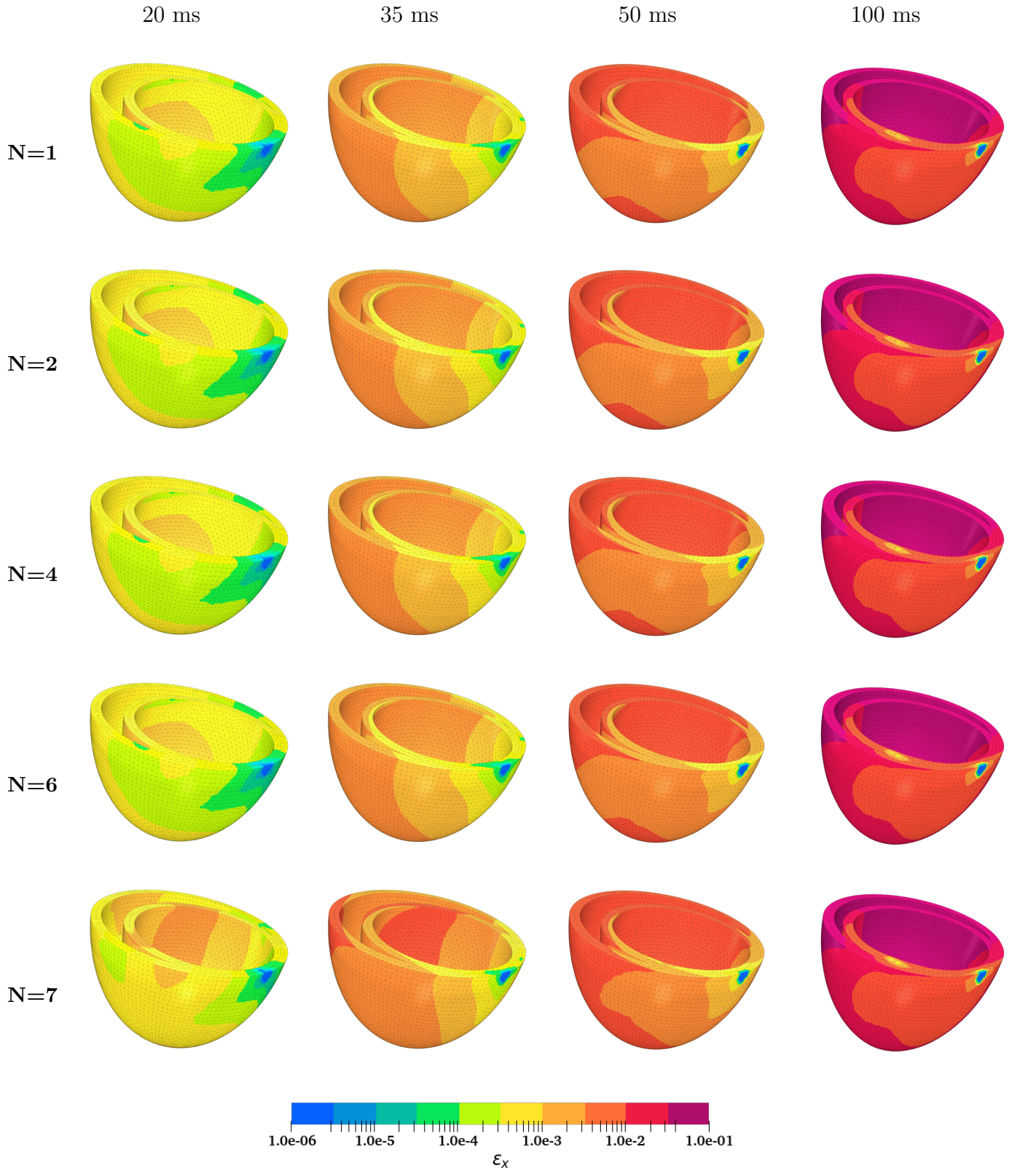


Figure 19: Numerical example 3. Contour plot of $\varepsilon_{\boldsymbol{x}}$ in (49) for snapshots associated with various times $t = \{20, 35, 50, 100\}$ (ms) of the cardiac cycle. Results obtained with **MFA**-$\gamma$ formulation and staggered solver for different values of the ratio between the mechanical and electrical time steps $N = \{1, 2, 4, 6, 7\}$, (*activation type*: active strain).

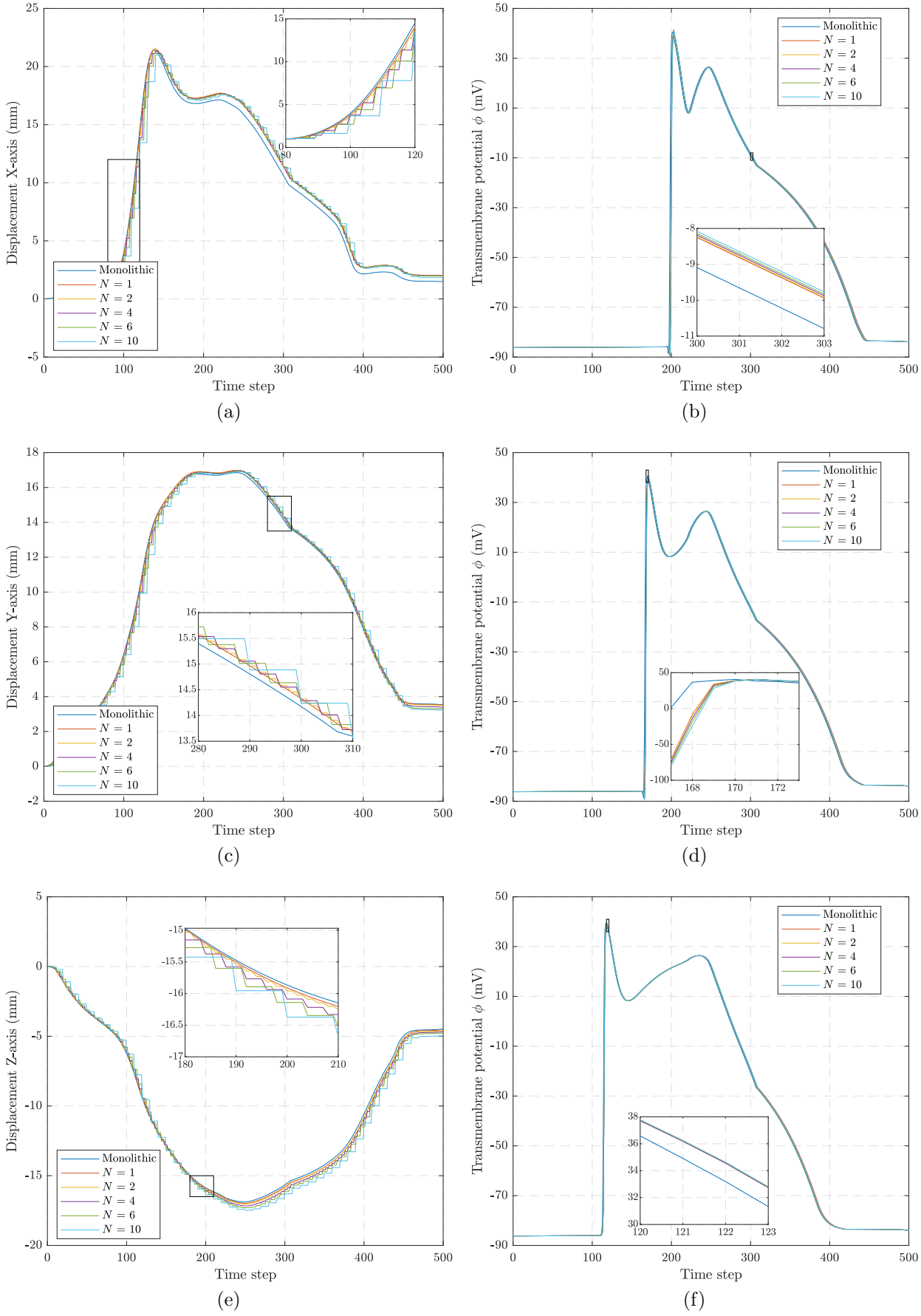


Figure 20: Numerical example 3. Comparison of monolithic and staggered solvers with the $\boldsymbol{x}$-$\phi$-$p$ formulation: (a)-(b) Time evolution of the displacement in $X$ direction and transmembrane potential $\phi$ at node $A$. (c)-(d) Time evolution of the displacement in $Y$ direction and transmembrane potential $\phi$ at node $B$. (e)-(f) Time evolution of the displacement in $Z$ direction and transmembrane potential $\phi$ at node $C$. Results obtained (*activation type*: active stress).

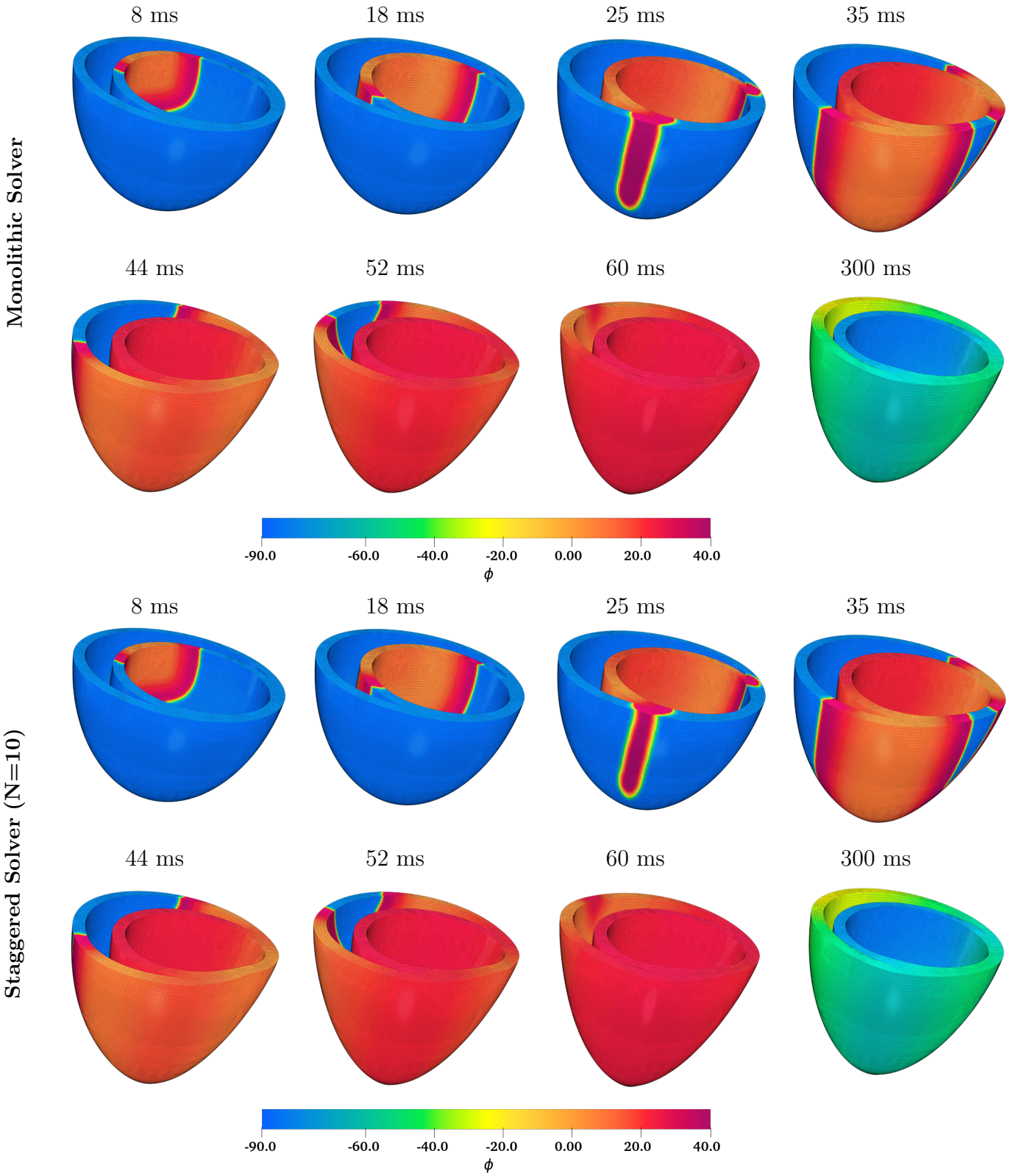


Figure 21: Numerical example 3. Evolution of the cardiac action potential wave-front. Snapshots for various times $t = \{8, 18, 25, 35, 44, 52, 60, 300\}$ (ms) of the cardiac cycle. Results obtained with $\boldsymbol{x}$-$\phi$-$p$ formulation using the monolithic solver (up) and the staggered solver with $N = 10$ (down), *activation type*: active stress).

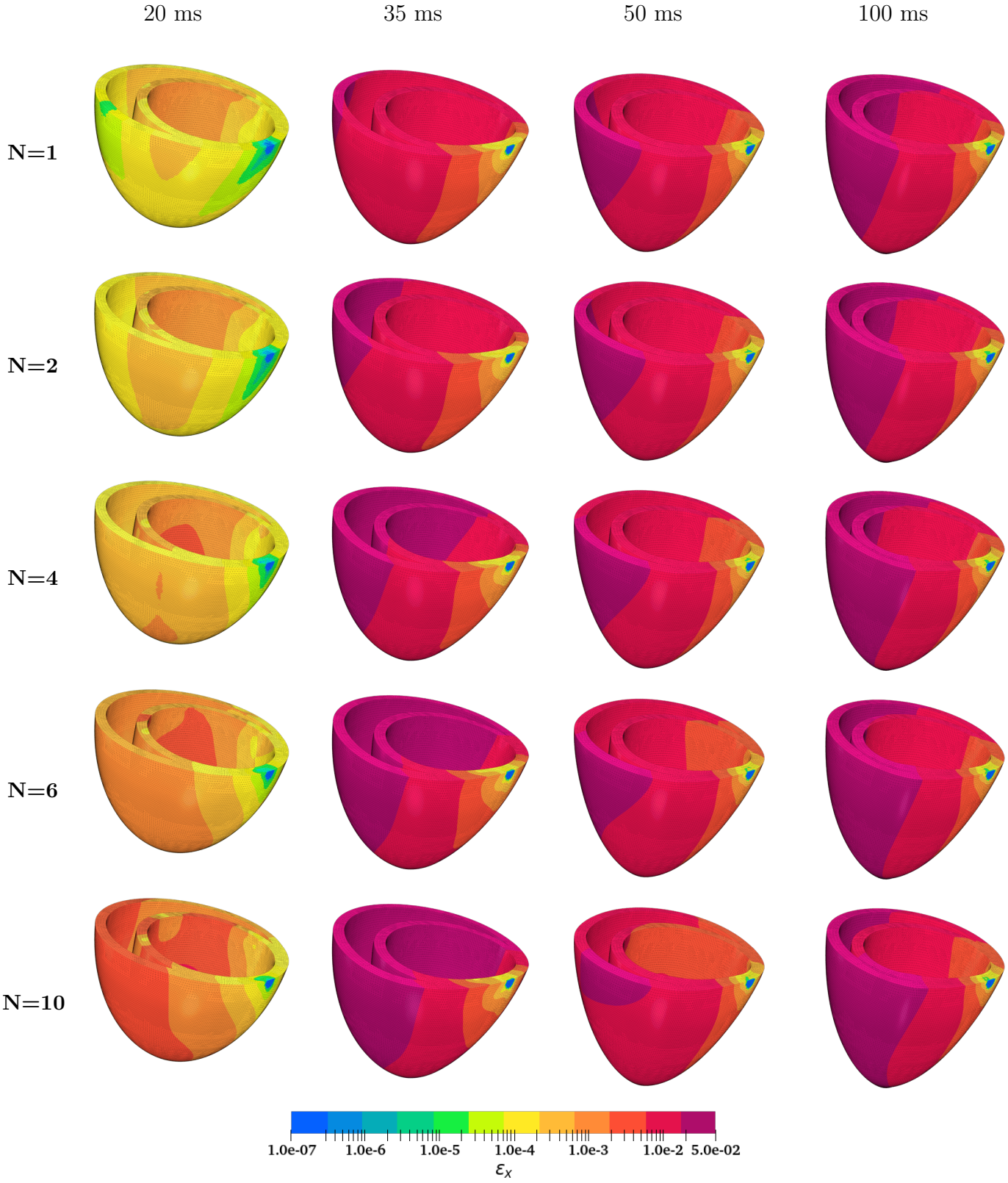


Figure 22: Numerical example 3. Contour plot of $\varepsilon_{\boldsymbol{x}}$ in (49) for snapshots associated with various times $t = \{20, 35, 50, 100\}$ (ms) of the cardiac cycle. Results obtained with $\boldsymbol{x}$-$\phi$-$p$ formulation and staggered solver for different values of the ratio between the mechanical and electrical time steps $N = \{1, 2, 4, 6, 10\}$, (*activation type*: active stress).

The required computational time was slightly greater for the *active strain* approach (due to the higher nonlinearity of the passive response model which leads to a larger number of Newton-Raphson iterations), and both approaches experience appreciable performance improvement with the inclusion of staggered solvers. The computational times for all the large scale simulations are organised in Table 4 according to the selected numerical strategy, proving the considerable time reduction when a $\boldsymbol{x}$-$\phi$-$p$ formulation with a staggered solver is employed instead of **MFA** formulations with a monolithic solver. The computational save stems from the reduction in time in terms of assembly and static condensation, in comparison with the more demanding **MFA** formulations, due to their extended multi-field nature.

| **Computation time for the MFA-$\gamma$ mixed formulation (in hours)** | | | | | |
|---|---|---|---|---|---|
| Monolithic | Stag. $N = 1$ | Stag. $N = 2$ | Stag. $N = 4$ | Stag. $N = 6$ | Stag. $N = 7$ |
| 195.7 | 106.7 | 57.33 | 37.57 | 37.93 | 38.63 |

| **Computation time for the MFA-$T_a$ mixed formulation (in hours)** | | | | | | |
|---|---|---|---|---|---|---|
| Monolithic | Stag. $N = 1$ | Stag. $N = 2$ | Stag. $N = 4$ | Stag. $N = 6$ | Stag. $N = 8$ | Stag. $N = 10$ |
| 181.23 | 83.4 | 55.73 | 47.93 | 36.47 | 34.73 | 30.07 |

| **Computation time for the $\boldsymbol{x}$-$\phi$-$p$ mixed formulation (in hours)** | | | | | | |
|---|---|---|---|---|---|---|
| | Monolithic | Stag. $N = 1$ | Stag. $N = 2$ | Stag. $N = 4$ | Stag. $N = 6$ | Stag. $N = 10$ |
| Nonlinear | 90.33 | 50.78 | 31.58 | 17.4 | 14.27 | 11.32 |
| Linearised | - | 17 | - | 6.83 | - | 4.83 |

Table 4: List of measured computational times for the MFA-$T_a$, MFA-$\gamma$ and $\boldsymbol{x}$-$\phi$-$p$ mixed formulations.

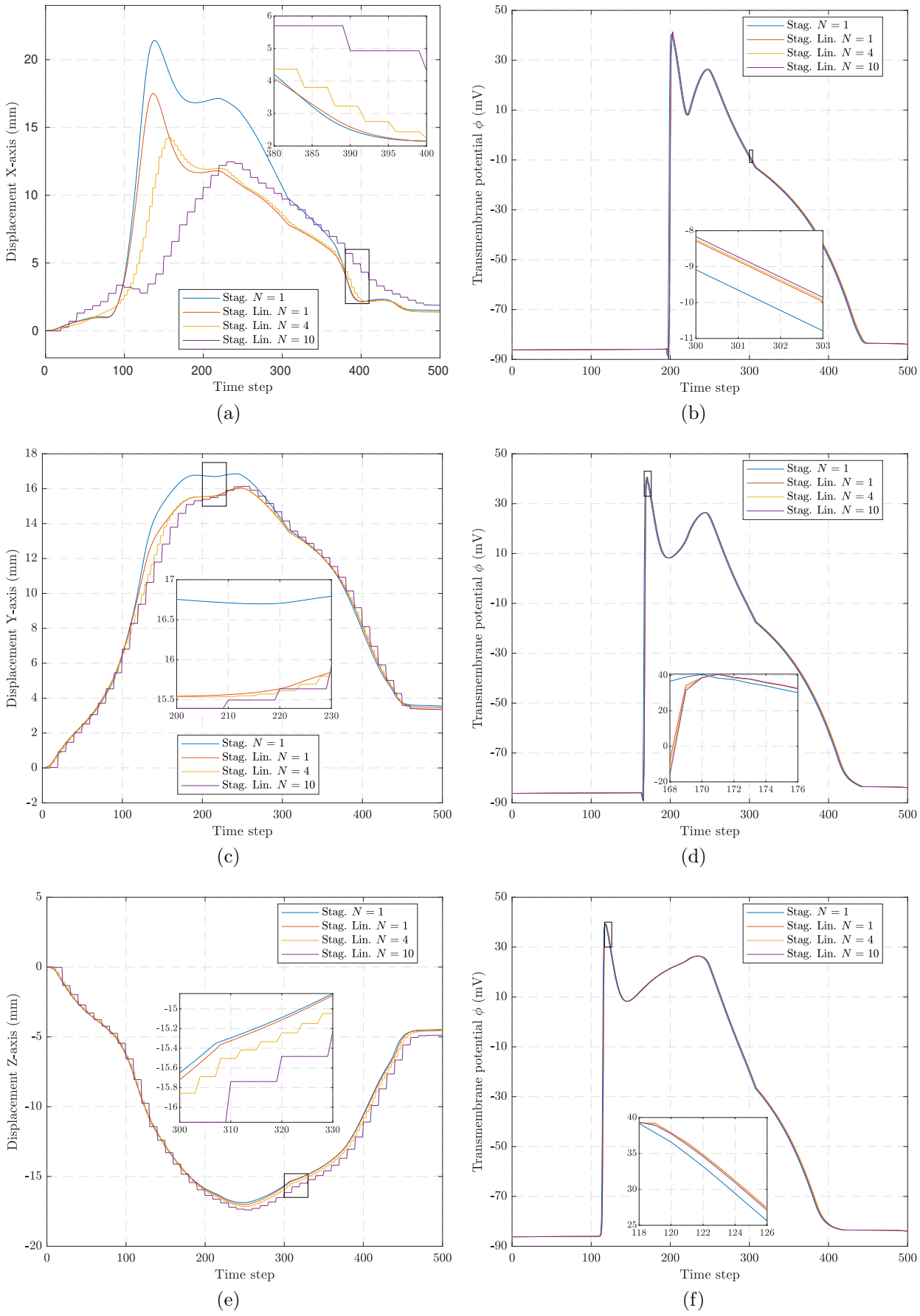


Figure 23: Numerical example 5. Comparison of staggered solver with $N = 1$ and staggered linearised solver (for various $N$) for $\boldsymbol{x}$-$\phi$-$p$ formulation: (a)-(b) Time evolution of the displacement in $X$ direction and potential $\phi$ at node $A$. (c)-(d) Time evolution of the displacement in $Y$ direction and transmembrane potential $\phi$ at node $B$. (e)-(f) Time evolution of the displacement in $Z$ direction and transmembrane potential $\phi$ at node $C$. Results obtained (*activation type*: active stress).

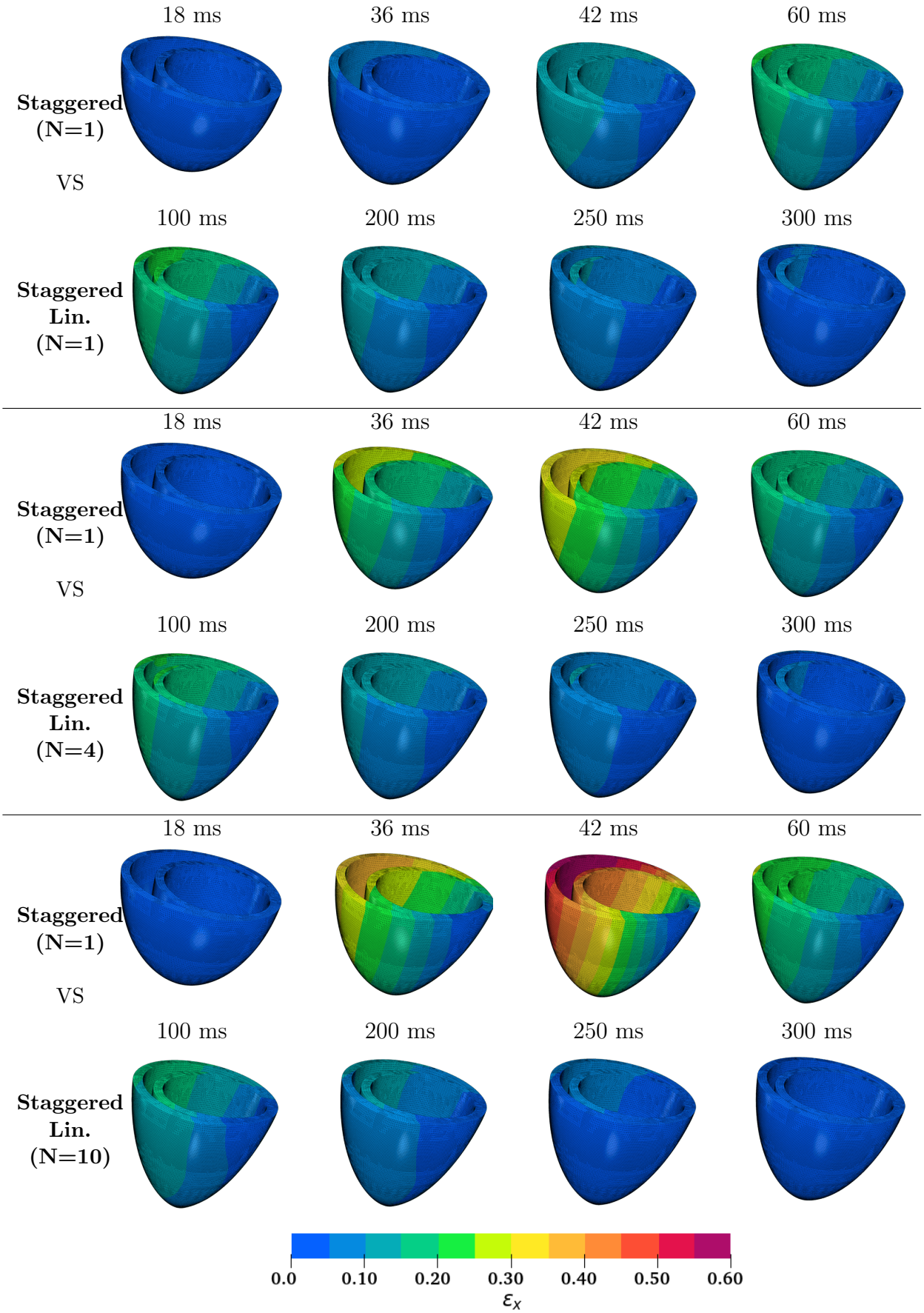


Figure 24: Numerical example 5. Evolution of the cardiac action potential wave-front. Snapshots for various times $t = \{8, 36, 42, 60, 100, 200, 250, 300\}$ (ms) of the cardiac cycle. Results obtained with $\boldsymbol{x}$-$\phi$-p formulation using the staggered solver with $N = 1$ and the linearised staggered solver with $N = \{1, 4, 10\}$, *activation type*: active stress).

*6.4. Numerical example 4: a realistic geometry*

In this final numerical example, we select one of the possible techniques presented in previous sections and study the response of the myocardium through the simulation of a realistic geometry. Specifically, the objective **O4.I** of this example is to use a suitable numerical strategy for a pre-selected Finite Element formulation in order to analyse the electro-activation process in a non-simplified geometry such as the one represented by the pair of idealised ventricles previously analysed (refer to Figure 7). The more realistic geometry is depicted in Figure $25_a$. The fibre directions are represented in Figure $25_b$-$25_c$, where a regularisation (smoothing) of the fibre orientation has been carried out as described in Section 6.2. Figure $25_b$ represents the fibre orientation resulting scalar field $\eta$. Boundary and initial conditions are described in Figure 26. Regarding the material parameters for the passive response, namely the activation model and the ionic model, we use the same as those detailed in Section 6.2.

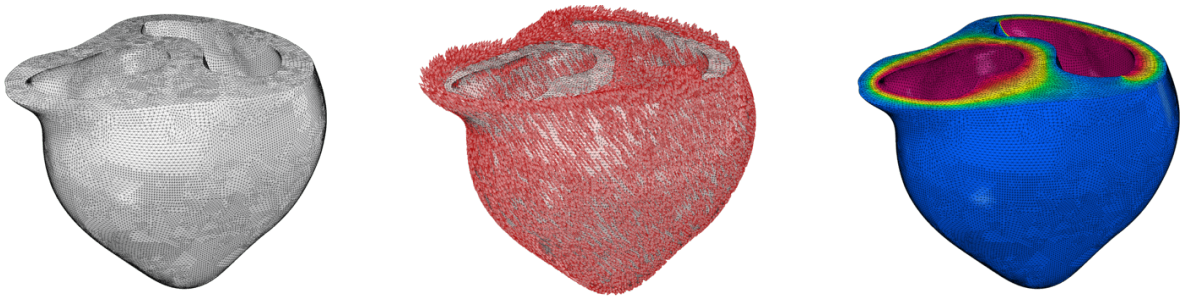

(a) (b) (c)

Figure 25: Numerical example 6. (a) Geometry of the two realistic ventricles. (b) Representation of the fibre $\boldsymbol{f}_0$. (c) Contour plot of $\eta$ for the interpolation of $\boldsymbol{f}_0$. Blue and red regions correspond to $\eta = 1$ and $\eta = 0$, respectively.

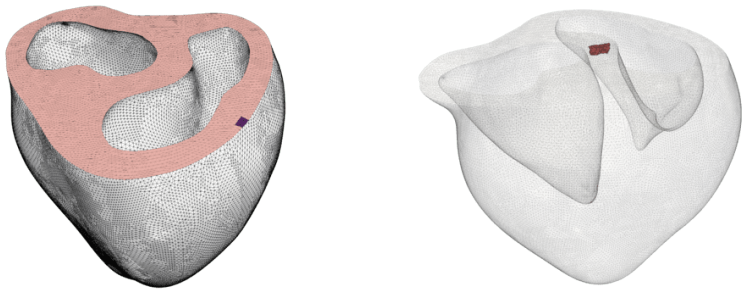

(a) (b)

Figure 26: Numerical example 6. (a) Regions for the application of Dirichlet boundary conditions for displacement field. In red: restricted displacements in $OZ$ direction; in white: restricted displacements in all directions. (b) Region (in red) where the initial electrical stimulation occurs.

The Finite Element formulation employed is that of the $\boldsymbol{x}$-$\phi$-$p$ approach, where a sufficiently fine mesh discretisation has been employed in order to alleviate the presence of possible bending locking. As such, a minimum of 10 finite elements across the thickness have been used following the conclusions extracted from our first numerical example. This level of discretisation is consistent with the mesh considered, as displayed in Figure $26_a$. The corresponding degrees of freedom add up in total to $\{703914, 234638, 234638\}$ for the fields $\boldsymbol{x}$-$\phi$-$p$, respectively. Results displayed in previous examples reported an excellent accuracy of the staggered solver (in comparison with the monolithic solver), especially for the active stress approach. Thus, we advocate for this solver and consider a ratio between the mechanical and electrical time steps of $N = 10$. Notice that, although it might seem more appealing, in principle, the use of the staggered linearised solver, this can yield inaccurate results for this high value of the ratio $N$.

With this combination of Finite Element formulation and numerical strategy, we present in Figures 27 and 28 the results for the contour plot distribution of relevant quantities of interest for different time snapshots. This information is arranged in a similar manner to that in the large scale numerical examples from [1], which allow to shed some light into crucial aspects of cardiac action potential propagation and global motion. In particular, we would like to highlight that (a): even though the same diffusion values from Table 3 were used, the realistic ventricles get fully depolarised in 35 ms whereas the idealised ones required 60 ms, probably due to the different structure of the heart chambers; (b) a smoother field for the right Cauchy tensor component $C_{XX}$ is obtained compared to that in [1] thanks to the employment of a finer mesh; (c) the use of a realistic geometry emphasises the twisting effect as a result of the transmural anisotropy variation; (d) the combination of a $\boldsymbol{x}$-$\phi$-$p$ formulation with a staggered solver reduces the overall computational time up to sixteen times without any loss of certainty, as supported by the findings in the previous examples.

## 7. Concluding remarks

The computational simulation of the heart muscle represents a major challenge due to the complex intertwining of the different electro-chemo-mechanical processes interacting across different space and time scales. In the search towards an efficient yet accurate computational solver in cardiac mechanics, this paper has presented a coupled multi-scale framework where alternative formulations, discretisations and coupling strategies have been presented and analysed in the context of idealised and realistic ventricular geometries. First, a stabilised linear finite element formulation for displacement, pressure and transmembrane potential ($\boldsymbol{x}$-$\phi$-$p$ formulation) has been compared against the super enhanced **MFA** formulation recently proposed in [1] and the widely used penalty-based $\boldsymbol{x}$-$\phi$ approach. Second, a staggered solver and a staggered linearised solver have been assessed in terms of accuracy against the monolithic solver in [1], for both active strain and active stress electro-activation.

Through a set of numerical examples, we have been able to conclude that: (a) at least 10 elements across the thickness of the myocardium must be used in order to attain an acceptable level of accuracy in terms of deformations when using the $\boldsymbol{x}$-$\phi$-$p$ formulation, whilst only 2 elements are needed in the case of the **MFA** formulation; (b) even finer discretisations are needed if the widely used $\boldsymbol{x}$-$\phi$ formulation is to be preferred, as otherwise untrustworthy results will be obtained; (c) the strong anisotropy of the Holzapfel-Ogden model can induce some form of locking which can be totally circumvented with the **MFA** formulation and, partially, with the $\boldsymbol{x}$-$\phi$-$p$ formulation; (d) both $\boldsymbol{x}$-$\phi$-$p$ and **MFA** formulations render extremely similar results in terms of transmembrane potential propagation but slight differences are observed in terms of deformation patterns; (e) these differences are more pronounced in the case of active strain electro-activation due to the strongest nonlinearity of the electro-mechanical coupling; (f) the staggered solver is extremely competitive (specially in case of active stress electro-activation) allowing time step ratios of up to 10 between the electrical and mechanical physics without compromising the accuracy of the results; (g) the proposed staggered linearised solver yields extremely accurate results for the transmembrane potential propagation but struggles to provide accurate results in terms of deformation unless the same time step is used for both individual physics or a more careful linearisation is adopted. This is due to the high variability of the transmembrane potential, specially in the vicinity of sharp gradients, leading to non-negligible deformation updates within a mechanical time step.

**Acknowledgements**
The second and third authors acknowledge the support provided by the Sêr Cymru National Research Network under the Sêr Cymru II Fellowship "Virtual engineering of the new generation of biomimetic artificial muscles", funded by the European Regional Development Fund. The third

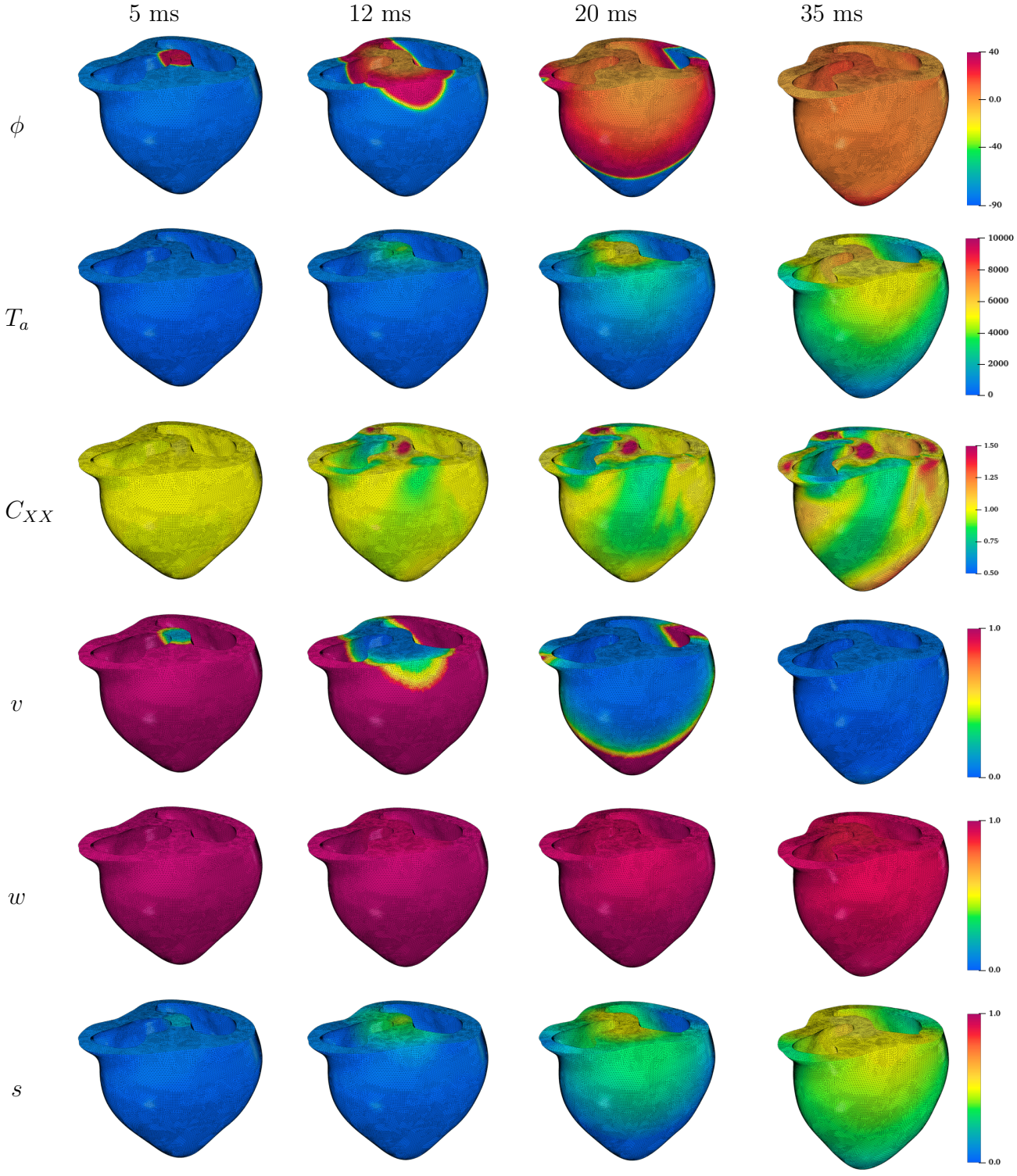


Figure 27: Numerical example 4. (*activation type*: active stress; *ionic model*: Bueno-Ovorio; *activation law*: Nash & Panfilov; *mixed formulation*: $\boldsymbol{x}$-$\phi$-$p$ formulation; *Numerical Strategy*: staggered solver with $N = 10$). Snapshots for time $t = \{5, 20, 40, 100\}$ (ms) of the cardiac cycle. Contour plot of $\phi$ (mV), cardiomyocite stress $T_a$ (Pa), right Cauchy-Green tensor component $C_{XX}$ and three internal variables, namely $\{v, w, s\}$.

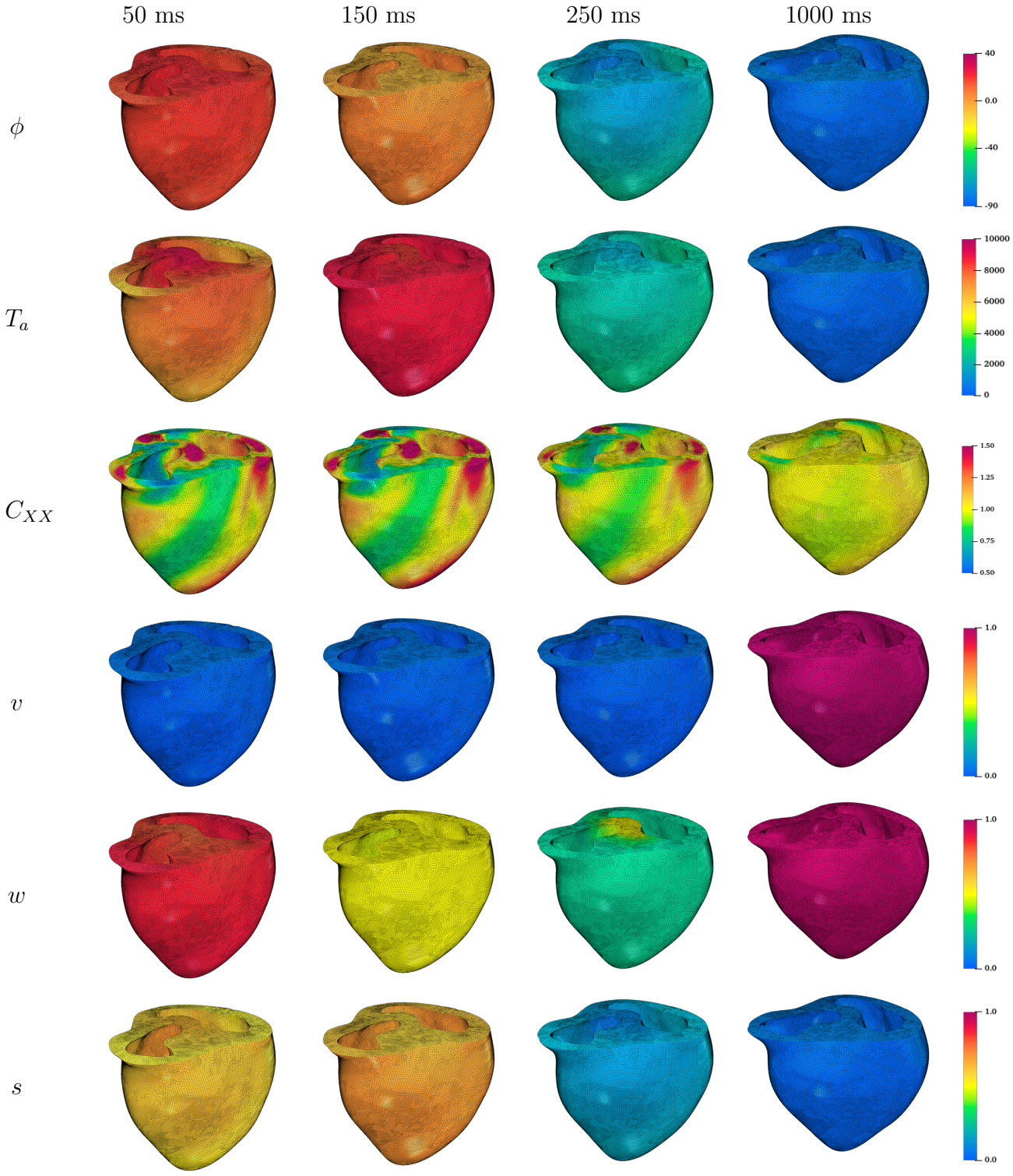


Figure 28: Numerical example 4. (*activation type*: active stress; *ionic model*: Bueno-Ovorio; *activation law*: Nash & Panfilov; *mixed formulation*: $\boldsymbol{x}$-$\phi$-$p$ formulation; *Numerical Strategy*: staggered solver with $N = 10$). Snapshots for time $t = \{150, 200, 320, 1000\}$ (ms) of the cardiac cycle. Contour plot of $\phi$ (mV), cardiomyocite stress $T_a$ (Pa), right Cauchy-Green tensor component $C_{XX}$ and three internal variables, namely $\{v, w, s\}$.

author acknowledges the financial support received through the European Training Network AdMoRe (Project ID: 675919).

[1] E. Garcia-Blanco, R. Ortigosa, A. J. Gil, C. H. Lee, J. Bonet, A new computational framework for electro-activation in cardiac mechanics, Computer Methods in Applied Mechanics and Engineering 348 (2019) 796 – 845.

[2] World Health Organization, Hearts: Technical package for cardiovascular disease management in primary health care (2016).

[3] E. Wilkins, L. Wilson, K. Wickramasinghe, P. Bhatnagar, J. Leal, R. Luengo-Fernandez, R. Burns, M. Rayner, N. Townsend, European cardiovascular disease statistics (2017).

[4] D. Mozaffarian, E. J. Benjamin, A. S. Go, D. K. Arnett, M. J. Blaha, M. Cushman, S. R. Das, S. de Ferranti, J. P. Després, H. J. Fullerton, et al., Heart disease and stroke statistics, Circulation 133 (2016) e38–e360.

[5] J. Hanson, H. E. Huxley, Structural basis of the cross-striations in muscle, Nature 172 (1953) 530.

[6] G. J. Tortora, B. H. Derrickson, Principles of anatomy and physiology, John Wiley & Sons, 2008.

[7] M. Potse, B. Dubé, J. Richer, A. Vinet, R. M. Gulrajani, A comparison of monodomain and bidomain reaction-diffusion models for action potential propagation in the human heart, IEEE Transactions on Biomedical Engineering 53 (2006) 2425–2435.

[8] A. L. Hodgkin, A. F. Huxley, Propagation of electrical signals along giant nerve fibres, Proceedings of the Royal Society of London. Series B, Biological Sciences (1952) 177–183.

[9] J. Vossoughi, R. N. Vaishnav, D. J. Patel, Compressibility of the myocardial tissue, Advances in Bioengineering (1980) 45–48.

[10] G. A. Holzapfel, R. W. Ogden, Constitutive modelling of passive myocardium: a structurally based framework for material characterization, Philosophical Transactions of the Royal Society of London A: Mathematical, Physical and Engineering Sciences 367 (2009) 3445–3475.

[11] Y. C. Fung, Biomechanics: Mechanical properties of living tissues, Springer Science & Business Media, 2013.

[12] J. Wong, E. Kuhl, Generating fibre orientation maps in human heart models using Poisson interpolation, Computer Methods in Biomechanics and Biomedical Engineering 17 (2014) 1217–1226.

[13] F. Fenton, A. Karma, Vortex dynamics in three-dimensional continuous myocardium with fiber rotation: filament instability and fibrillation, Chaos: An Interdisciplinary Journal of Nonlinear Science 8 (1998) 20–47.

[14] S. Soloveva, S. Tuikina, Numerical solution of the inverse problem for the mathematical model of cardiac excitation, Computational Mathematics and Modeling 27 (2016) 162–171.

[15] H. Watanabe, S. Sugiura, H. Kafuku, T. Hisada, Multiphysics simulation of left ventricular filling dynamics using fluid-structure interaction finite element method, Biophysical journal 87 (2004) 2074–2085.

[16] A. Quarteroni, T. Lassila, S. Rossi, R. Ruiz-Baier, Integrated heartcoupling multiscale and multiphysics models for the simulation of the cardiac function, Computer Methods in Applied Mechanics and Engineering 314 (2017) 345–407.

[17] P. C. Franzone, L. Pavarino, B. Taccardi, Simulating patterns of excitation, repolarization and action potential duration with cardiac bidomain and monodomain models, Mathematical biosciences 197 (2005) 35–66.

[18] L. Tung, A bidomain model for describing ischemic myocardial DC potentials., Ph.D. thesis, Massachusetts Institute of Technology, 1978.

[19] B. J. Roth, J. P. Wikswo, A bidomain model for the extracellular potential and magnetic field of cardiac tissue, IEEE Transactions on Biomedical Engineering (1986) 467–469.

[20] R. M. Bordas, K. Gillow, D. Gavaghan, B. Rodríguez, D. Kay, A bidomain model of the ventricular specialized conduction system of the heart, SIAM Journal on Applied Mathematics 72 (2012) 1618–1643.

[21] L. J. Leon, B. M. Horáček, Computer model of excitation and recovery in the anisotropic myocardium: I. rectangular and cubic arrays of excitable elements, Journal of Electrocardiology 24 (1991) 1–15.

[22] S. Göktepe, S. Acharya, J. Wong, E. Kuhl, Computational modeling of passive myocardium, International Journal for Numerical Methods in Biomedical Engineering 27 (2011) 1–12.

[23] S. Rossi, T. Lassila, R. Ruiz-Baier, A. Sequeira, A. Quarteroni, Thermodynamically consistent orthotropic activation model capturing ventricular systolic wall thickening in cardiac electromechanics, European Journal of Mechanics-A/Solids 48 (2014) 129–142.

[24] B. Baillargeon, N. Rebelo, D. D. Fox, R. L. Taylor, E. Kuhl, The living heart project: a robust and integrative simulator for human heart function, European Journal of Mechanics-A/Solids 48 (2014) 38–47.

[25] R. FitzHugh, Mathematical models of threshold phenomena in the nerve membrane, The Bulletin of Mathematical Biophysics 17 (1955) 257–278.

[26] J. Nagumo, S. Arimoto, S. Yoshizawa, An active pulse transmission line simulating nerve axon, Proceedings of the IRE 50 (1962) 2061–2070.

[27] C. H. Luo, Y. Rudy, A dynamic model of the cardiac ventricular action potential. ii. afterdepolarizations, triggered activity, and potentiation., Circulation Research 74 (1994) 1097–1113.

[28] R. R. Aliev, A. V. Panfilov, A simple two-variable model of cardiac excitation, Chaos, Solitons & Fractals 7 (1996) 293–301.

[29] M. Courtemanche, R. J. Ramirez, S. Nattel, Ionic mechanisms underlying human atrial action potential properties: insights from a mathematical model, American Journal of Physiology-Heart and Circulatory Physiology 275 (1998) H301–H321.

[30] L. Priebe, D. J. Beuckelmann, Simulation study of cellular electric properties in heart failure, Circulation Research 82 (1998) 1206–1223.

[31] V. Iyer, R. Mazhari, R. L. Winslow, A computational model of the human left-ventricular epicardial myocyte, Biophysical Journal 87 (2004) 1507–1525.

[32] K. ten Tusscher, D. Noble, P. Noble, A. Panfilov, A model for human ventricular tissue, American Journal of Physiology-Heart and Circulatory Physiology 286 (2004) H1573–H1589.

[33] K. H. ten Tusscher, A. V. Panfilov, Alternans and spiral breakup in a human ventricular tissue model, American Journal of Physiology-Heart and Circulatory Physiology 291 (2006) H1088–H1100.

[34] A. Bueno-Orovio, E. M. Cherry, F. H. Fenton, Minimal model for human ventricular action potentials in tissue, Journal of Theoretical Biology 253 (2008) 544–560.

[35] H. Demiray, On the constitutive equations of biological materials, Journal of Applied Mechanics 42 (1975) 242–243.

[36] J. Humphrey, R. Strumpf, F. Yin, Determination of a constitutive relation for passive myocardium: I. A new functional form, Journal of Biomechanical Engineering 112 (1990) 333–339.

[37] B. Smaill, P. Hunter, Structure and function of the diastolic heart: material properties of passive myocardium, in: Theory of Heart, Springer, 1991, pp. 1–29.

[38] J. M. Guccione, A. D. McCulloch, Finite element modeling of ventricular mechanics, in: Theory of Heart, Springer, 1991, pp. 121–144.

[39] K. D. Costa, J. W. Holmes, A. D. McCulloch, Modelling cardiac mechanical properties in three dimensions, Philosophical Transactions of the Royal Society of London A: Mathematical, Physical and Engineering Sciences 359 (2001) 1233–1250.

[40] L. A. Taber, R. Perucchio, Modeling heart development, Journal of Elasticity 61 (2000) 165–198.

[41] M. P. Nash, A. V. Panfilov, Electromechanical model of excitable tissue to study reentrant cardiac arrhythmias, Progress in Biophysics and Molecular Biology 85 (2004) 501–522.

[42] E. J. Vigmond, C. Clements, D. M. McQueen, C. S. Peskin, Effect of bundle branch block on cardiac output: a whole heart simulation study, Progress in Biophysics and Molecular Biology 97 (2008) 520–542.

[43] S. Göktepe, E. Kuhl, Electromechanics of the heart: a unified approach to the strongly coupled excitation–contraction problem, Computational Mechanics 45 (2010) 227–243.

[44] J. Wong, S. Göktepe, E. Kuhl, Computational modeling of electrochemical coupling: a novel finite element approach towards ionic models for cardiac electrophysiology, Computer Methods in Applied Mechanics and Engineering 200 (2011) 3139–3158.

[45] J. Wong, S. Göktepe, E. Kuhl, Computational modeling of chemo-electro-mechanical coupling: A novel implicit monolithic finite element approach, International Journal for Numerical Methods in Biomedical Engineering 29 (2013) 1104–1133.

[46] S. Rossi, R. Ruiz-Baier, L. F. Pavarino, A. Quarteroni, Orthotropic active strain models for the numerical simulation of cardiac biomechanics, International journal for numerical methods in biomedical engineering 28 (2012) 761–788.

[47] A. Gizzi, R. Ruiz-Baier, S. Rossi, A. Laadhari, C. Cherubini, S. Filippi, A three-dimensional continuum model of active contraction in single cardiomyocytes, in: Modeling the Heart and the Circulatory System, Springer, 2015, pp. 157–176.

[48] L. Pavarino, S. Scacchi, S. Zampini, Newton–krylov-bddc solvers for nonlinear cardiac mechanics, Computer Methods in Applied Mechanics and Engineering 295 (2015) 562–580.

[49] S. Deparis, D. Forti, G. Grandperrin, A. Quarteroni, Facsi: A block parallel preconditioner for fluid–structure interaction in hemodynamics, Journal of Computational Physics 327 (2016) 700–718.

[50] J. Bonet, A. J. Gil, R. Ortigosa, A computational framework for polyconvex large strain elasticity, Computer Methods in Applied Mechanics and Engineering 283 (2015) 1061–1094.

[51] G. Scovazzi, B. Carnes, X. Zeng, A simple, stable and accurate tetrahedral finite element for transient, nearly incompressible, linear and nonlinear elasticity: A dynamic variational multiscale approach, International Journal for Numerical Methods in Engineering (2015).

[52] A. J. Gil, R. Ortigosa, A new framework for large strain electromechanics based on convex multi-variable strain energies: variational formulation and material characterisation, Computer Methods in Applied Mechanics and Engineering 302 (2016) 293–328.

[53] R. Ortigosa, A. J. Gil, A new framework for large strain electromechanics based on convex multi-variable strain energies: Conservation laws, hyperbolicity and extension to electro-magneto-mechanics, Computer Methods in Applied Mechanics and Engineering 309 (2016) 202–242.

[54] R. Ortigosa, A. J. Gil, A new framework for large strain electromechanics based on convex multi-variable strain energies: Finite Element discretisation and computational implementation, Computer Methods in Applied Mechanics and Engineering 302 (2016) 329–360.

[55] R. Ortigosa, A. J. Gil, J. Bonet, C. Hesch, A computational framework for polyconvex large strain elasticity for geometrically exact beam theory, Computational mechanics 57 (2016) 277–303.

[56] J. Schröder, P. Neff, Invariant formulation of hyperelastic transverse isotropy based on polyconvex free energy functions, International Journal of Solids and Structures 40 (2003) 401–445.

[57] J. Schröder, P. Neff, D. Balzani, A variational approach for materially stable anisotropic hyperelasticity, International Journal of Solids and Structures 42 (2005) 4352–4371.

[58] J. Bonet, A. J. Gil, C. H. Lee, M. Aguirre, R. Ortigosa, A first order hyperbolic framework for large strain computational solid dynamics - Part I: Total Lagrangian isothermal elasticity, Computer Methods in Applied Mechanics and Engineering 283 (2015) 689–732.

[59] J. Bonet, A. J. Gil, R. Ortigosa, On a tensor cross product based formulation of large strain solid mechanics, International Journal of Solids and Structures 84 (2016) 49–63.

[60] J. M. Ball, Convexity conditions and existence theorems in nonlinear elasticity, Archive for Rational Mechanics and Analysis 63 (1976) 337–403.

[61] J. M. Ball, Energy-minimising configurations in nonlinear elasticity, Archive for Rational Mechanics and Analysis 63 (1976) 337–403.

[62] J. M. Ball, Geometry, Mechanics and Dynamics, Springer, pp. 3–59.

[63] R. Poya, R. Sevilla, A. J. Gil, A unified approach for a posteriori high-order curved mesh generation using solid mechanics, Computational Mechanics 58 (2016) 457–490.

[64] P. D. Ledger, A. J. Gil, R. Poya, M. Kruip, I. Wilkinson, S. Bagwell, Solution of an industrially relevant coupled magneto–mechanical problem set on an axisymmetric domain, Applied Mathematical Modelling 40 (2016) 1959–1971.

[65] R. Poya, A. J. Gil, R. Ortigosa, R. Sevilla, J. Bonet, W. A. Wall, A curvilinear high order finite element framework for electromechanics: From linearised electro-elasticity to massively deformable dielectric elastomers, Computer Methods in Applied Mechanics and Engineering 329 (2018) 75–117.

[66] R. de Boer, Vektor- und Tensorrechnung für Ingenieure, Springer-Verlag, 1982.

[67] M. P. Nash, P. J. Hunter, Computational mechanics of the heart, Journal of Elasticity and the Physical Science of Solids 61 (2000) 113–141.

[68] J. M. Ball, F. Murat, $W^{1,p}$-quasiconvexity and variational problems for multiple integrals, Journal of Functional Analysis 58 (1984) 225–253.

[69] J. Strobeck, E. Sonnenblick, Myocardial contractile properties and ventricular performance, The Heart and Cardiovascular System (1986) 31–49.

[70] F. Brezzi, M. Fortin, Mixed and Hybrid Finite Element Methods, Springer-Verlag New York, Inc., New York, NY, USA, 1991.

[71] I. Babuška, The finite element method with Lagrangian multipliers, Numerische Mathematik 20 (1973) 179–192.

[72] T. J. R. Hughes, L. P. Franca, M. Balestra, A new finite element formulation for computational fluid dynamics: V. Circumventing the Babuška-Brezzi condition: a stable Petrov-Galerkin formulation of the Stokes problem accommodating equal-order interpolations, Computer Methods in Applied Mechanics and Engineering 59 (1986) 85–99.

[73] A. J. Gil, C. H. Lee, J. Bonet, R. Ortigosa, A first order hyperbolic framework for large strain computational solid dynamics - Part II: Total Lagrangian compressible, nearly incompressible and truly incompressible elasticity, Computer Methods in Applied Mechanics and Engineering 300 (2016) 146–181.

[74] P. Wriggers, J. Schröder, F. Auricchio, Finite element formulations for large strain anisotropic material with inextensible fibers, Advanced Modeling and Simulation in Engineering Sciences 3 (2016) 25.

[75] C. G. Petra, O. Schenk, M. Lubin, K. Gärtner, An augmented incomplete factorization approach for computing the schur complement in stochastic optimization, SIAM Journal on Scientific Computing 36 (2014) C139–C162.

[76] HSL, A collection of fortran codes for large-scale scientific computation, http://www.hsl.rl.ac.uk, 2007. Accessed: 2018-1-30.